

WL-TR-93-3059

AD-A268 596

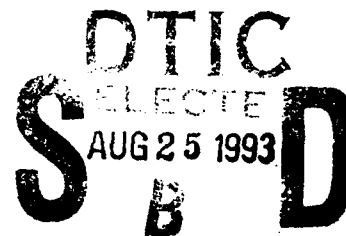


**LASER VELOCIMETRY MEASUREMENTS
OF VORTEX FLOWS ON A DELTA WING
AT MACH 1.9**

Linda G. Smith
Dr. Mark S. Maurice
Charles Tyler
Dr. George L. Seibert
C. Dean Miller

January 1993

Final Report for Period August 1990 - September 1992



Approved for public release; distribution is unlimited

FLIGHT DYNAMICS DIRECTORATE
WRIGHT LABORATORY
AIR FORCE MATERIEL COMMAND
WRIGHT-PATTERSON AIR FORCE BASE, OHIO 45433-7562

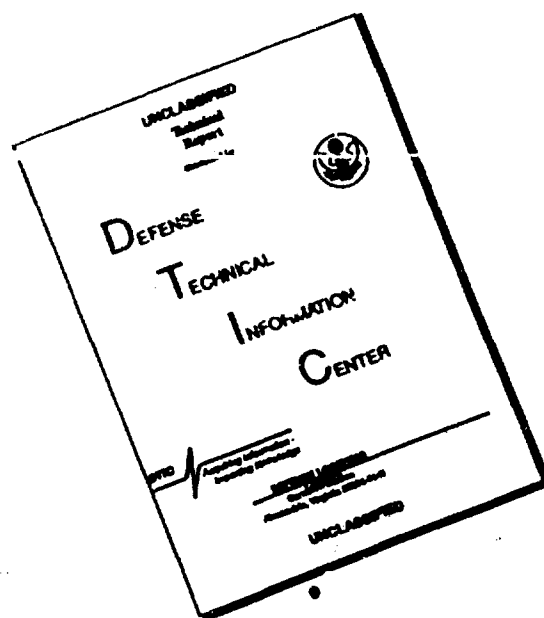


93-19709



11505

DISCLAIMER NOTICE



THIS DOCUMENT IS BEST
QUALITY AVAILABLE. THE COPY
FURNISHED TO DTIC CONTAINED
A SIGNIFICANT NUMBER OF
PAGES WHICH DO NOT
REPRODUCE LEGIBLY.


NOTICE


When Government drawings, specifications, or other data are used for any purpose other than in connection with a definitely Government-related procurement, the United States Government incurs no responsibility or any obligation whatsoever. The fact that the government may have formulated or in any way supplied the said drawings, specifications, or other data, is not to be regarded by implication, or otherwise in any manner construed, as licensing the holder, or any other person or corporation; or as conveying any rights or permission to manufacture, use, or sell any patented invention that may in any way be related thereto.

This report is releasable to the National Technical Information Service (NTIS). At NTIS, it will be available to the general public, including foreign nationals.

This technical report has been reviewed and is approved for publication.


LINDA G. SMITH
Aerospace Engineer
Experimental Facilities Research Branch


GEORGE L. SEIBERT, Chief
Experimental Facilities Research Branch
Aeromechanics Division


DENNIS SEDLOCK, Chief
Aeromechanics Division
Flight Dynamics Directorate

If your address has changed, if you wish to be removed from our mailing list, or if the addressee is not longer employed by your organization please notify WL/FIME, WPAFB, OH 45433-7562 to help us maintain a current mailing list.

Copies of this report should not be returned unless return is required by security considerations, contractual obligations, or notice on a specific document.

REPORT DOCUMENTATION PAGE			Form Approved OMB No. 0704-0188	
<small>Public reporting burden for this collection of information is estimated to average 1 hour per response, including the time for reviewing instructions, searching existing data sources, gathering and maintaining the data needed, and completing and reviewing the collection of information. Send comments regarding this burden estimate or any other aspect of this collection of information, including suggestions for reducing this burden, to Washington Headquarters Services, Directorate for Information Operations and Reports, 1215 Jefferson Davis Highway, Suite 1204, Arlington, VA 22202-4302, and to the Office of Management and Budget, Paperwork Reduction Project (0704-0188), Washington, DC 20503.</small>				
1. AGENCY USE ONLY (Leave blank)		2. REPORT DATE Jan 93	3. REPORT TYPE AND DATES COVERED Final: Aug 90 to Sep 92	
4. TITLE AND SUBTITLE Laser Velocimetry Measurements of Vortex Flows on a Delta Wing at Mach 1.9			5. FUNDING NUMBERS PE-62201F PR-2404 TA-13 WU-21	
6. AUTHOR(S) Linda G. Smith, Dr. Mark S. Maurice, Charles Tyler, Dr. George L. Seibert, C. Dean Miller				
7. PERFORMING ORGANIZATION NAME(S) AND ADDRESS(ES) Flight Dynamics Directorate, Wright Laboratory Air Force Materiel Command WPAFB OH 45433-7562			8. PERFORMING ORGANIZATION REPORT NUMBER WL-TR-93-3059	
9. SPONSORING / MONITORING AGENCY NAME(S) AND ADDRESS(ES)			10. SPONSORING / MONITORING AGENCY REPORT NUMBER	
11. SUPPLEMENTARY NOTES				
12a. DISTRIBUTION / AVAILABILITY STATEMENT Approved for Public Release; Distribution is Unlimited.			12b. DISTRIBUTION CODE	
13. ABSTRACT (Maximum 200 words) Off-body flow visualizations and fluid velocity measurements are conducted in a supersonic vortex flow. Three-dimensional laser velocimetry measurements are made in the leeward flowfield over a simple sharp-edged delta wing with 75 degree sweep angle. Tests are conducted at Mach 1.9 and Reynolds number of 2.4×10^6 based on model root chord. Measurements are made at 40% and 80% chord positions for 20 and 30 degree angles of attack and at 40% chord for 35 degrees. Mean velocities and turbulence intensities are measured on the five planes. Measurement accuracy is discussed in detail. The measurements define the location of the vortex core and provide the flowfield velocities surrounding the vortex. The difficulties inherent with seeding high velocity vortex flows are discussed.				
14. SUBJECT TERMS Laser Velocimetry Measurement of Vortical Flowfields			15. NUMBER OF PAGES 115	
			16. PRICE CODE	
17. SECURITY CLASSIFICATION OF REPORT Unclassified	18. SECURITY CLASSIFICATION OF THIS PAGE Unclassified	19. SECURITY CLASSIFICATION OF ABSTRACT Unclassified	20. LIMITATION OF ABSTRACT Unlimited	

TABLE OF CONTENTS

LIST OF FIGURES	iii
LIST OF TABLES	v
PREFACE AND ACKNOWLEDGEMENTS	vi
NOMENCLATURE	viii
1.0 INTRODUCTION	1
2.0 TEST DESCRIPTION	6
3.0 MEASUREMENT ACCURACY	16
4.0 RESULTS	22
5.0 CONCLUSIONS	36
6.0 RECOMMENDATIONS	37
7.0 REFERENCES	38
APPENDIX A: QUANTITATIVE RESULTS	41
APPENDIX B: PARTICLE DYNAMICS IN VORTICAL FLOWS	89
APPENDIX C: COMPUTATIONAL FLUID DYNAMICS RESULTS	98

DTIC QUALITY INSPECTED 3

Accession For	
NTIS OMA&I	<input checked="" type="checkbox"/>
DTIC TAB	<input type="checkbox"/>
Unannounced	<input type="checkbox"/>
Justification	
By	
Distribution/	
Availability Codes	
Dist	Avail and/or Special
A-1	

LIST OF FIGURES

Fig. 1. Laser Light Sheet Visualization of Delta Wing at Mach 1.9 and $\alpha = 28^\circ$	2
Fig. 2. Classification Chart for Vortices from Miller and Wood (1985).	4
Fig. 3. Three-view Sketch of Sharp-Edged Delta Wing.	7
Fig. 4. Delta Wing Model in Trisonic Gasdynamics Facility Test Section.	8
Fig. 5. Three-Component Laser Velocimetry System for Delta Wing Test.	9
Fig. 6. Transmitting Optics for Laser Velocimetry System	10
Fig. 7. Receiving Optics for Laser Velocimetry System	11
Fig. 8. Photodiode Position Detection System	13
Fig. 9. Data Collection System	14
Fig. 10. Schematic Diagram of Flow about a Sharp-Edged Delta Wing.	15
Fig. 11. Turbulence Intensity Field at $x/L = 40\%$ for $\alpha = 30^\circ$	17
Fig. 12. Axial Velocity Histograms around the Vortex Core Region at $x/L = 40\%$ for $\alpha = 30^\circ$	19
Fig. 13. Two-Dimensional Velocity Field at $x/L = 40\%$ for $\alpha = 20^\circ$	23
Fig. 14. Two-Dimensional Velocity Field at $x/L = 80\%$ for $\alpha = 20^\circ$	24
Fig. 15. Two-Dimensional Velocity Field at $x/L = 40\%$ for $\alpha = 30^\circ$	25
Fig. 16. Two-Dimensional Velocity Field at $x/L = 80\%$ for $\alpha = 30^\circ$	26
Fig. 17. Two-Dimensional Velocity Field at $x/L = 40\%$ for $\alpha = 35^\circ$	27
Fig. 18. Typical Velocity Histogram of Axial Component of Velocity.	29
Fig. 19. Transformed Two-Dimensional Velocity Field Estimating Location of Vortex Origin at $x/L = 80\%$ for $\alpha = 20^\circ$	30

Fig. 20. Three-Dimensional Representation of Axial Velocity Component on the $x/L = 40\%$ plane for $\alpha = 20^\circ$	32
Fig. 21. Normalized Axial Velocity Component vs. Span-wise Distance on Model for $z = 0.25$ cm to $z = 2.54$ cm.	33
Fig. 22. Normalized Axial Velocity Component vs. Span-wise Distance on Model for $z = 2.79$ cm to $z = 4.83$ cm.	34
Fig. A-1. Model Coordinate System	42

LIST OF TABLES

Table A-1. Experimental Data for 20° Angle of Attack, 40% Chord	43
Table A-2. Experimental Data for 20° Angle of Attack, 80% Chord	55
Table A-3. Experimental Data for 30° Angle of Attack, 40% Chord	63
Table A-4. Experimental Data for 30° Angle of Attack, 80% Chord	70
Table A-5. Experimental Data for 35° Angle of Attack, 40% Chord	76

PREFACE AND ACKNOWLEDGEMENTS

The laser velocimetry measurements of a supersonic vortex was part of a larger program to study supersonic vortex flows on a delta wing. However, significant scientific contributions were made in the extension of supersonic laser velocimetry to vortical flows to merit publication of the laser velocimetry (LV) data in this independent report. To the best of the authors' knowledge these are the first laser velocimetry measurements of a supersonic vortex. Many experimenters have made successful LV measurements of subsonic vortex flows, but none had reported successful measurements in a supersonic vortex.

Computational Fluid Dynamics analysis of this flowfield was conducted by Dr. Phillip Webster of the Computational Fluid Dynamics Research Section, Aeromechanics Division, Flight Dynamics Directorate, Wright Laboratory. It was the intention of all researchers to conduct a CFD validation for this flowfield; however, the facility Reynolds number range was changed to provide a high quality flowfield. Thus, a direct quantitative comparison was not possible; but where possible, a qualitative comparison was made. Dr. Mark Maurice used the CFD data as part of a particle dynamics analysis and thus performed a mutual CFD-experimental validation. This CFD-experimental validation is included as Appendix B of this report.

Mr. Robert Guyton is acknowledged for his design of the overall comprehensive test of the supersonic delta wing. The following technicians and tunnel operators provided invaluable

support for these tests: Larry Rieker, Earl Sine, Karl Schoffstall, Charlie McNeely, SSgt Brian Lewis, Mike Green, and Dwight Fox. Glenn Williams and Hank Baust provided invaluable knowledge and advice in the design and writing of the computer programs that made this test possible.

The authors wish to thank Drs. Phillip Webster and Joseph Shang for allowing us to include their AIAA Journal article on the computational fluid dynamics solution of this problem as an appendix. Including the journal articles as appendices makes this technical report a conclusive report on the efforts of the Aeromechanics Division of the Flight Dynamics Directorate on this program of research.

NOMENCLATURE

AOA	Angle of Attack
CL	Centerline
L	Chordwise length of model
L.E.	Leading edge
M_N	Mach number normal to leading edge
U	Velocity component in X direction
UINF	Freestream velocity
X	Axial distance from nose
Y	Spanwise distance from centerline
Z	Distance normal to surface
α	Angle of attack
α_N	Angle of attack normal to leading edge
Λ_{LE}	Wing leading-edge sweep angle

1.0 INTRODUCTION

The flow about modern high speed delta wing aircraft is characterized by the presence of large vortices on the leeward side of the wing. In many cases, these vortices are the primary aerodynamic structure affecting the performance of the aircraft. The vortices form at low angles of attack, with secondary and tertiary vortices forming at higher angles of attack due to boundary layer separation. Previous tests were conducted at the Wright Laboratory to obtain surface pressure profiles, surface oil flow visualizations, and off-body laser light sheet visualizations (Fig. 1). These tests reveal a major change in the supersonic vortex structure above 28° angle of attack (AOA) at Mach 1.9. The disappearance of feeding sheets, secondary vortices, and vortex shocks is observed in the light sheet visualizations.

Laser velocimetry (LV) was successfully applied to vortex flows for the subsonic case by Weissman (Ref 1), Yanta and Wardlaw (Ref 2), Owen and Johnson (Ref 3), and Schwind and Mullen (Ref 4), among others. However, LV measurements have not previously been reported in the case of a supersonic vortex flowfield. Due to the statistical nature of LV measurements, aperiodic, unsteady flows are biased by excessive turbulence levels and distorted mean velocities. In this test series, it is critical to define regions where the vortices burst so as to preclude representing the flow as highly turbulent, but steady state.

Miller and Wood (Ref 5) present a classification graph for flows over delta wings that



Fig. 1. Laser Light Sheet Visualization of Delta Wing at Mach 1.9 and $\alpha = 28^\circ$.

classify a flowfield into seven categories (Fig. 2): classical vortex, vortex with shock, separation bubble with no shock, separation bubble with shock, shock with no separation, shock-induced separation, and no shock/no separation. McMillan, et al. (Ref 6) verified the classification chart using computational results rather than the vapor screen flow visualization techniques used by Miller and Wood. The regions are classified on a graph of M_N versus α_N where M_N is the component of Mach number normal to the leading edge and α_N is the angle of attack normal to the leading edge as given in equations (1) and (2):

$$M_N = M \cos \Lambda_{LE} (1 + \sin^2 \alpha \tan^2 \Lambda_{LE})^{1/2} \quad (1)$$

$$\alpha_N = \tan^{-1}(\tan \alpha / \cos \Lambda_{LE}) \quad (2)$$

Laser light sheet flow visualization of the current 75° delta wing shows that the flow over this model is a classical vortex with a shock. The current test extends the region on the classification graph representing "vortex with shock" to higher values of α_N .

For this experiment, a three-dimensional LV system is used to measure the velocity components of a supersonic vortex flowfield over a simple sharp-edged delta wing at Mach 1.9. Mean velocity vectors are presented for two planes normal to the model at three angles of attack. Only a few planes of data are taken, since this study is accompanied by a companion computational fluid dynamic analysis of this problem (Ref 7). The LV measurements are needed for validation of the CFD solution, and once the CFD solution is

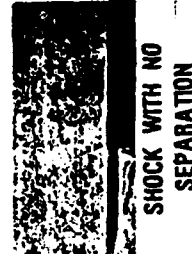
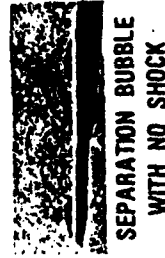
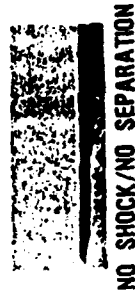
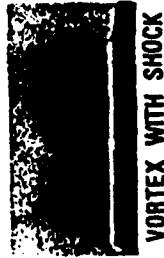
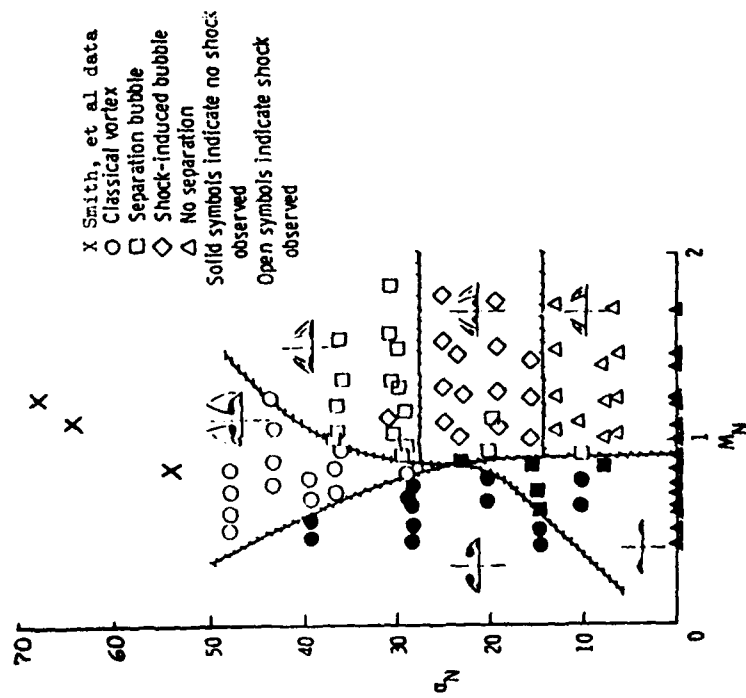


Fig. 2. Classification Chart for Vortices from Miller and Wood (1985).

validated, the CFD solution will be used as a definition of the complete flowfield. Angle of attack effects are discussed, along with an analysis of measurement bias.

2.0 TEST DESCRIPTION

The vortical flow on a sharp-edged delta wing is measured at 3 angles of attack (20° , 30° , and 35°). The leading edge sweep of the delta wing model is 75° and the leading edge vertex angle is 35° . A three-view sketch of the delta wing model and a photograph of this model are shown in Figs. 3 and 4. The model length is 33.91 cm with a thickness of 1.91 cm. The sharp edges have a maximum tip radius of 0.025 cm.

This vortex flow experiment is conducted in the Wright Laboratory's Trisonic Gasdynamics Facility (TGF). The TGF is a closed loop, continuous flow trisonic wind tunnel with a 0.61 m x 0.61 m (2 ft x 2 ft) test section for subsonic and supersonic operations. For this experiment, the TGF is operated at Mach 1.9 with a nominal stagnation pressure of 57.5 kPa and stagnation temperature of 310 K. The Reynolds number for this test is 2.4×10^6 based on the root chord of the model. The dynamic pressure is approximately 22.0 kPa.

A three-component laser velocimeter (Figs. 5 and 6), Bragg shifted in the velocity component normal to the free stream and model surface, is used to make the measurements. The collection optics (Fig. 7) are positioned approximately 10 degrees off-axis, limiting the effective length of the probe volume to 1.54 mm. The flow is seeded with 10-centistoke silicon oil which is introduced into the stagnation chamber using a specially designed seeder. Out-of-tunnel particle size measurements conducted with this seeder (Ref 8) show that 98% of the seed are smaller than $1.0 \mu\text{m}$ in diameter, although polydisperse.

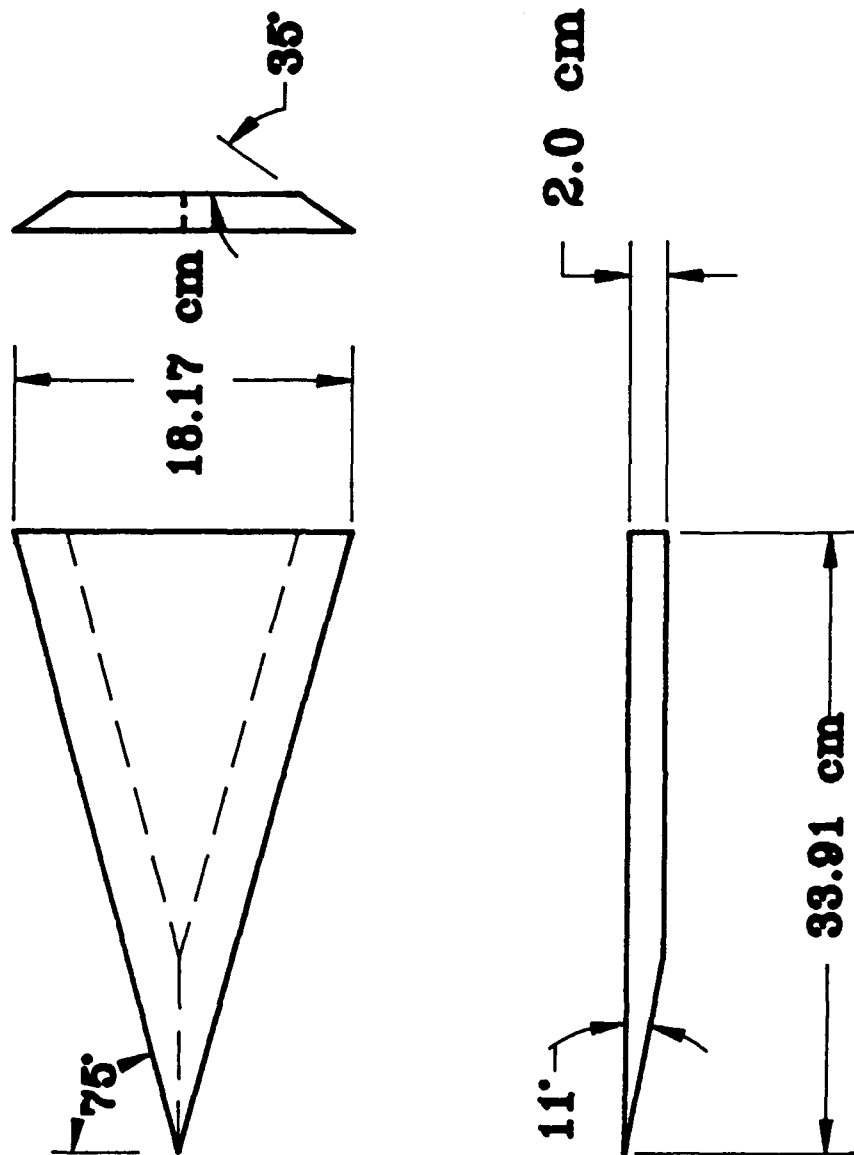


Fig. 3. Three-View Sketch of Sharp-Edged Delta Wing.



Fig. 4. Delta Wing Model in Trisonic Gasdynamics Facility Test Section.

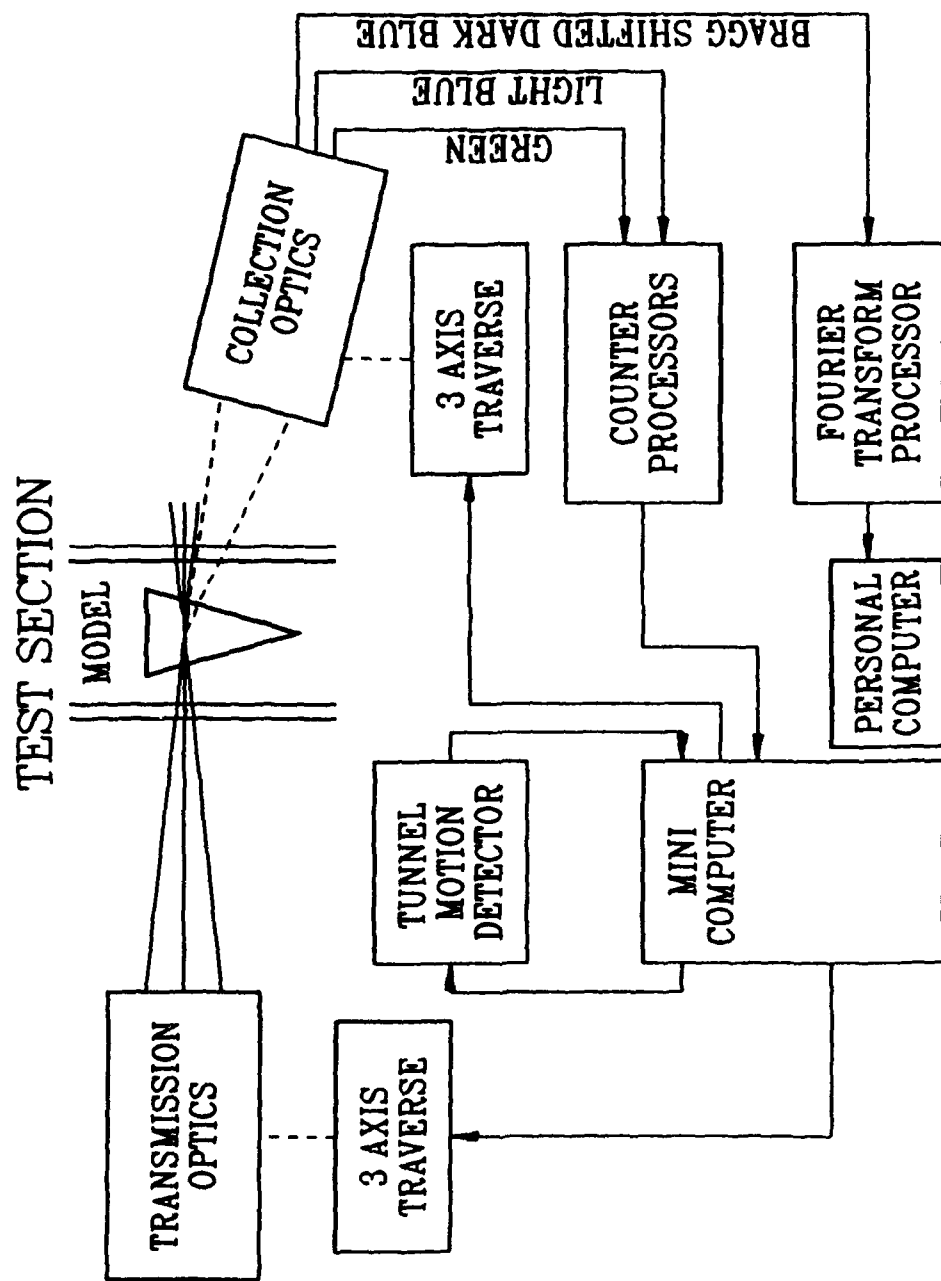


Fig. 5. Three-Component Laser Velocimetry System for Delta Wing Test.



Fig. 6. Transmitting Optics for Laser Velocimetry System.



Fig. 7. Receiving Optics for Laser Velocimetry System.

The system is configured in forward scatter mode. The transmitting optics (Fig. 6) and collection optics (Fig. 7) are driven separately on two machinist-style traverse tables with accuracy of 0.0025 mm. Tunnel movement (which can be up to 1.9 cm for a 3-hour run) is measured using a 1-mW Helium-Neon laser and a photodiode position detecting system (Fig. 8), with the results sent to the main computer and corrected coordinates sent to the traverse tables. The signals from the 514-nm-wavelength green and 476-nm-wavelength light blue beams are processed by a counter processor with a 1-nanosecond clock. The signals from the Bragg shifted 488 nm wavelength blue beams are weaker and require a Fast Fourier Transform (FFT) analysis to distinguish the signals from the noise; hence, the blue signals are processed with a hard wired processor based on the FFT algorithm. The counter processor and FFT analyzer are not connected; therefore, the multi-component velocity data are not restrained by a predetermined coincidence window. This allows for data rates sufficient to measure velocities closer to the vortex core. The counterprocessors, FFT analyzer, personal computer, and mini-computer are shown in Fig. 9.

A schematic of the generic flowfield over the delta wing model is shown in Fig. 10. Because this is a symmetrical model, the flow on only one-half of the span is measured. The test matrices consist of uniform grids on half planes normal to the model at 40% and 80% chord. Typical grid spacing is 0.51 cm by 0.51 cm. Based on previous laser light sheet and schlieren flow visualizations, the 40% chord location is representative of unburst vortex flow and the 80% chord location to represents burst vortex flow at the higher angles of attack.



Fig. 8. Photodiode Position Detection System.

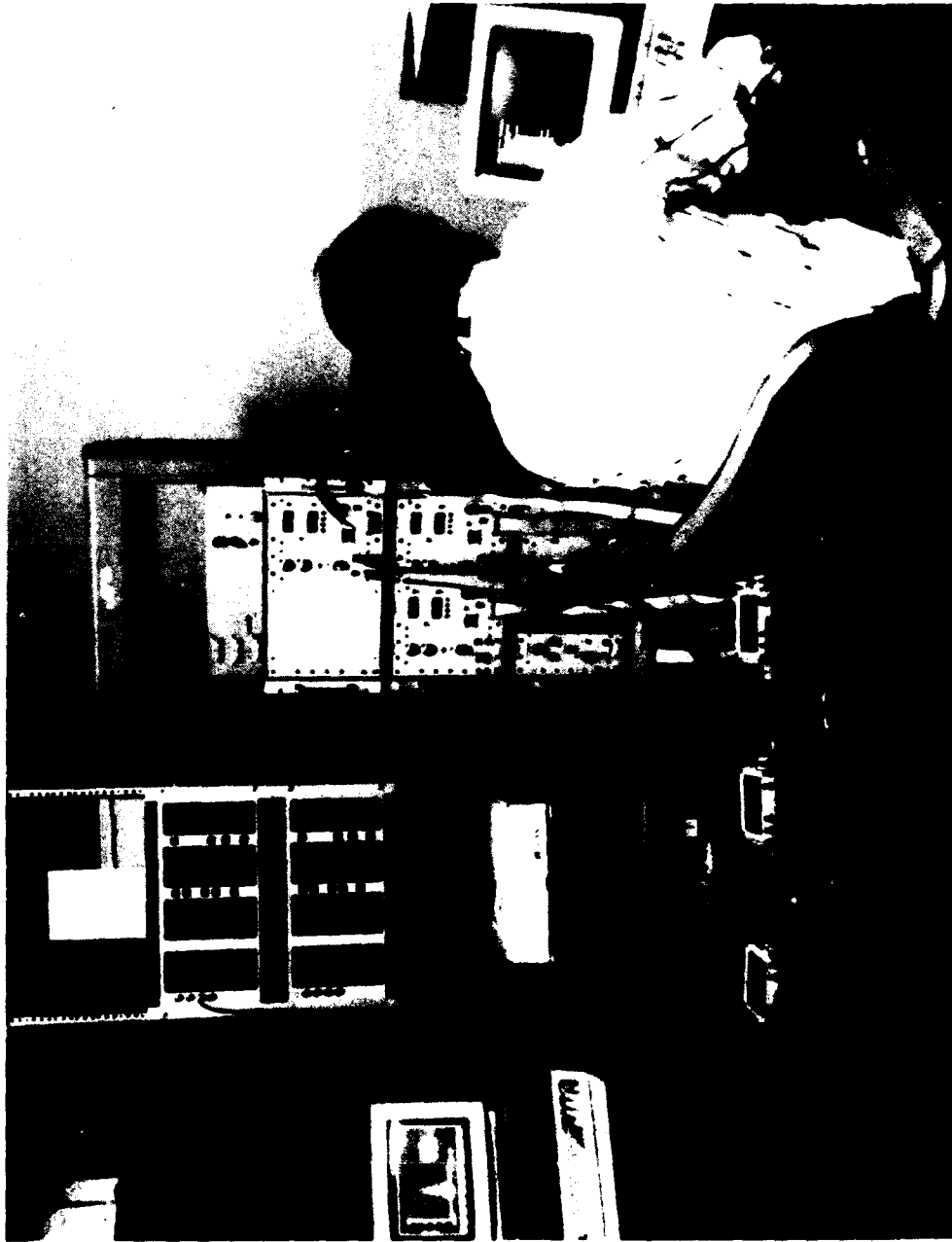
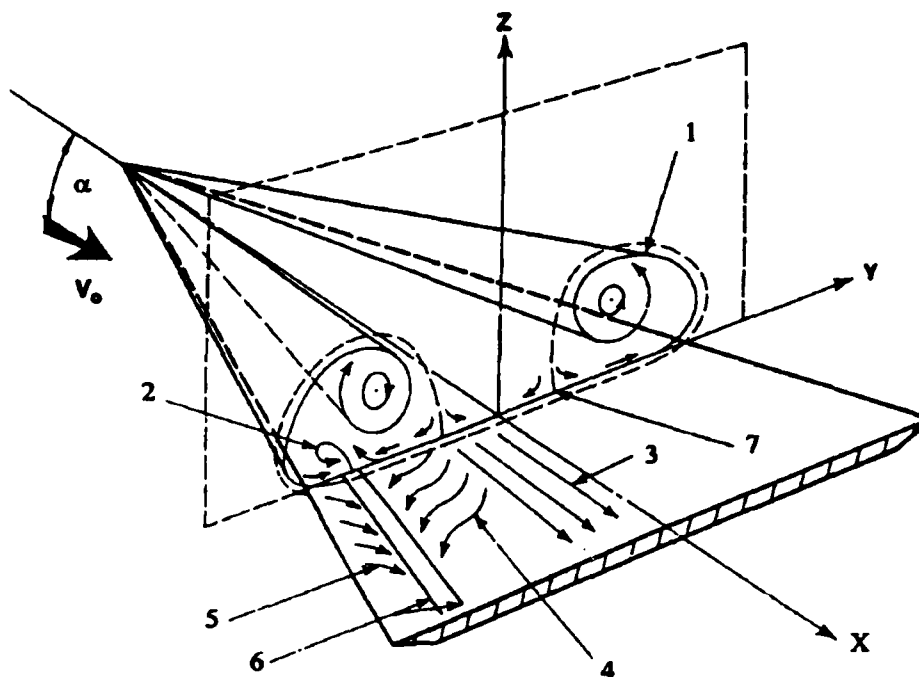


Fig. 9. Data Collection System.



SCHEMATIC FLOW DIAGRAM:

- (1) SCROLL VORTEX SHEET FORMING THE MAIN VORTEX**
- (2) SECONDARY VORTEX**
- (3) CENTRAL ZONE WITHOUT VORTEX FLOW**
- (4) ZONE INDUCED BY THE MAIN VORTEX**
- (5) ZONE INDUCED BY THE SECONDARY VORTEX**
- (6) ACCUMULATION ZONE (AIR BUBBLE OR COATING)**
- (7) REATTACHMENT LINE**

Fig. 10. Schematic Diagram of Flow about a Sharp-Edged Delta Wing.

3.0 MEASUREMENT ACCURACY

In general, LV measurements are biased by many sources within the optical, electronic, data processing, and seeding subsystems. While some of these sources, such as certain types of statistical bias, may be quite subtle, other sources of bias may dominate the measurements. A categorical breakdown of many of the known sources of measurement error is given by Jones, et al. (Ref 9) and Edwards (Ref 10), which include extensive references of LV bias investigations. For this test, particular sources of measurement error appear to be dominant, and help explain perturbations and voids within the presented vortex fields. By understanding the sources and effects of possible bias, experimental error can be distinguished from flowfield structures, and the data can be used to its full potential to supplement future experimental studies or CFD validation efforts.

One source of bias is that the LV measurements are time averaged to represent steady-state velocities, while the actual flowfield is not truly steady state. By visualizing cross sections of the flow with a laser light sheet, the vortex structure appears to be steady to the naked eye or to a video camera with a 60-frame-per-second resolution. However, by using a high-speed video with a 1-microsecond exposure time, the vortex contains structures which are both periodic and random. This inherent unsteadiness causes the measured turbulence intensity to be much higher than for a steady state flow. For example, Fig. 11 shows a representative turbulence intensity field with vertical and horizontal lines representing the magnitudes of the vertical and axial components of turbulence intensity with respect to the freestream velocity. Overall, the

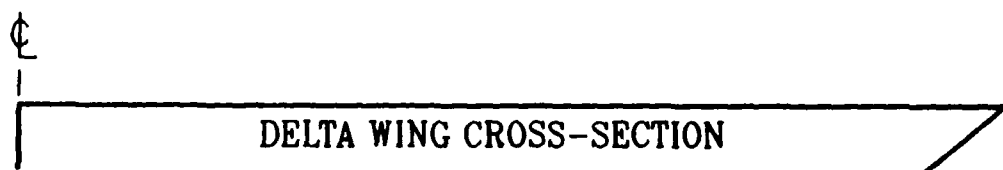
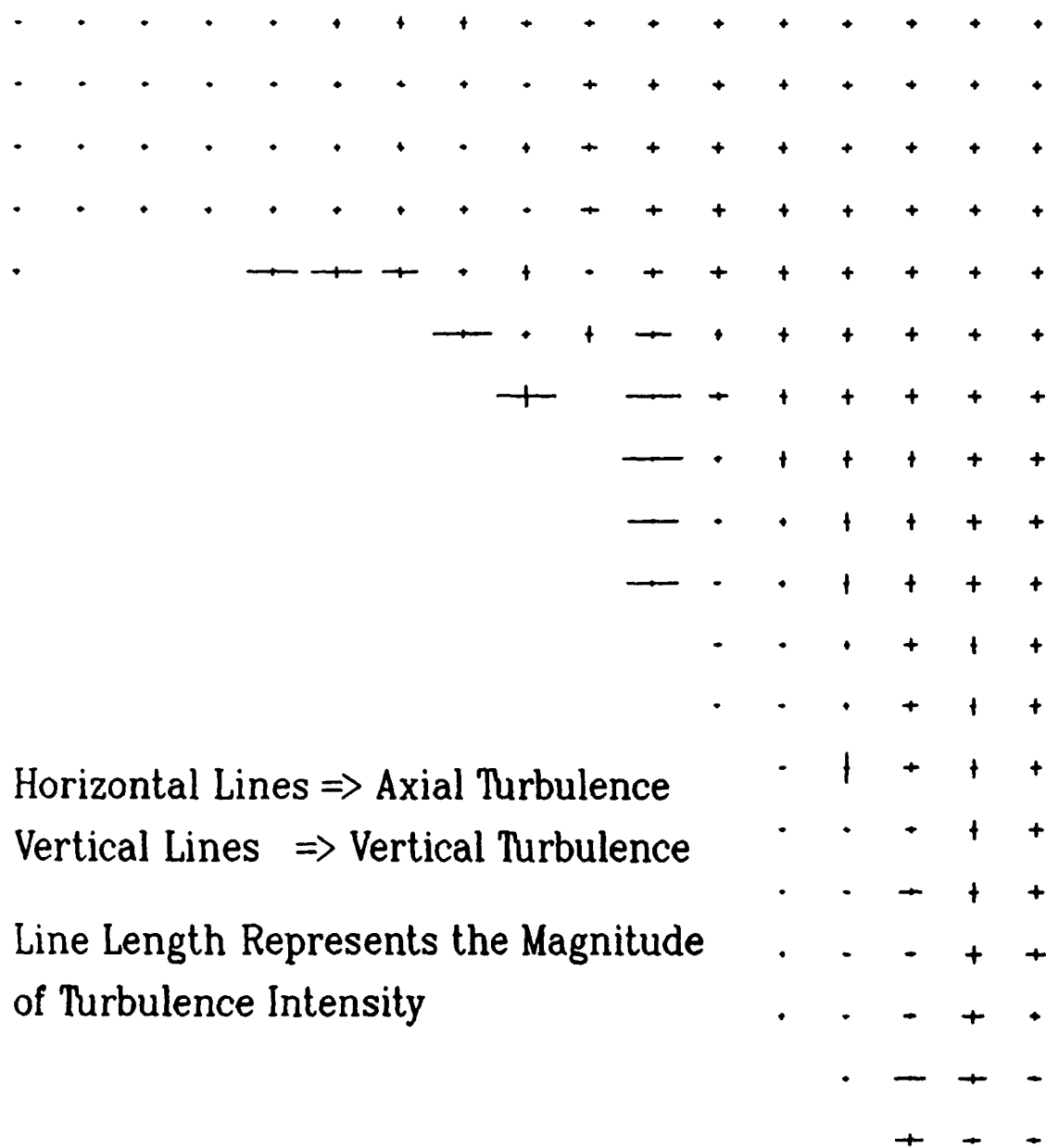


Fig. 11. Turbulence Intensity Field at $x/L = 40\%$ for $\alpha = 30^\circ$.

turbulence intensity in either direction is a relatively uniform 2 to 3 percent across the field, except for a few points along the core boundary where the axial values exceed 20%. Looking at the corresponding histograms at these locations, shown in Fig. 12, the flow at these points is bi-modal, which indicates two distinct flow conditions which alternate with time. The resulting turbulence intensity of the combined flow is much larger than the turbulence intensities of the two individual modes.

The second important source of bias within these surveys is due to the low signal-to-noise ratio of the burst signal. Many factors contribute to the size and clarity of the Doppler burst, including the precision of the optical alignment, the transmission of light through wind tunnel windows, and the quality and limitations of the optics and electronics in general. During these surveys, the data rate decreased substantially as the measurement location approached the vortex core, as the transparency of the windows is degraded by streaks of silicon oil, and as the optical alignment drifted over a period of several hours. Areas within the presented data where changes between neighboring velocity vectors appear erratic are most likely effected by this type of bias.

Another type of bias is due to the sensitivity of the flowfield to slight changes in tunnel conditions during a run and between runs. Most surveys required two to three separate runs of approximately 5 hours each. Despite efforts to precisely maintain steady flow conditions, slight changes in the flowfield are apparent within the presented velocity fields. Rows or columns of vectors with slightly different trends than neighboring rows and columns are indicative of data

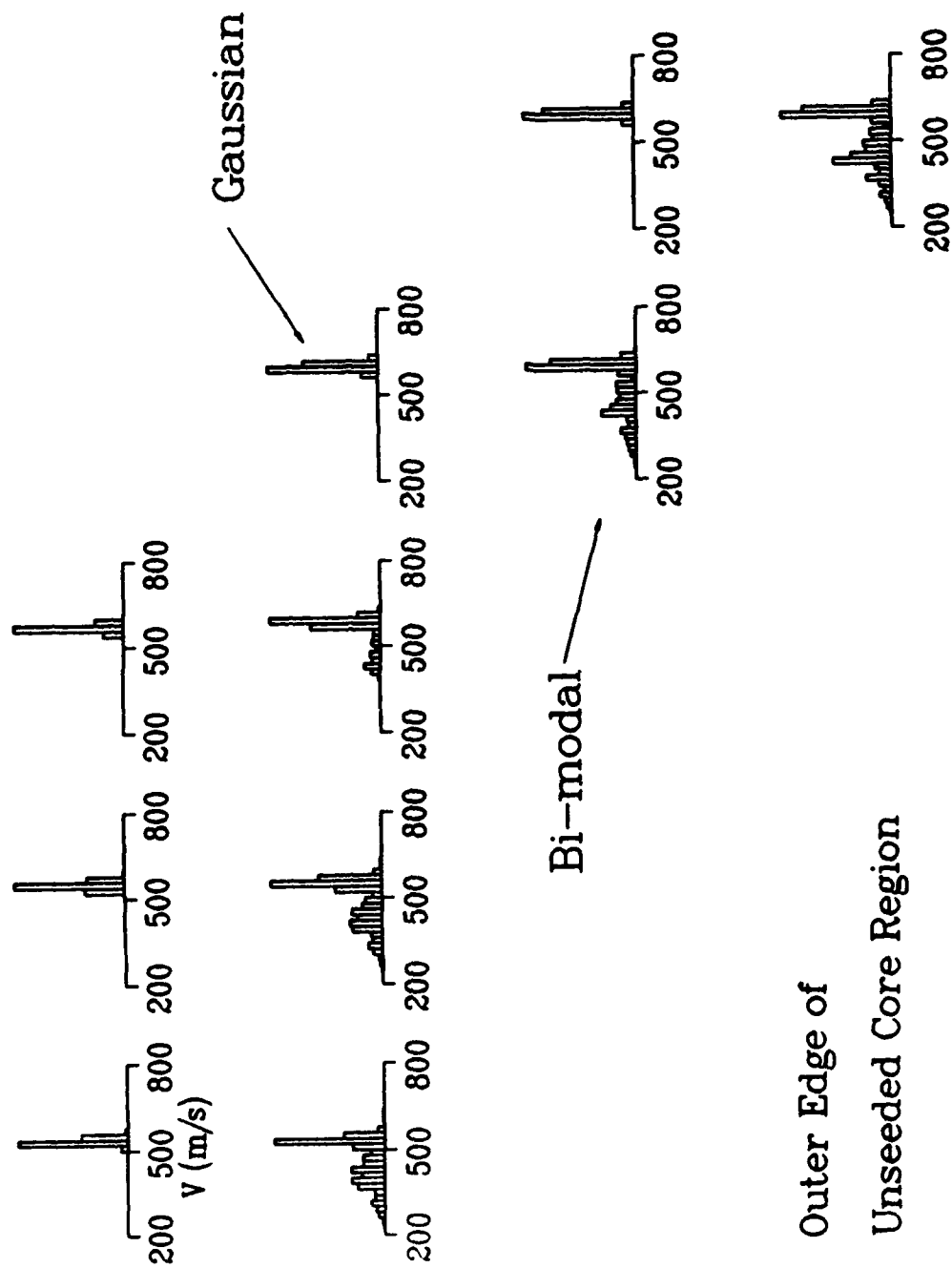


Fig. 12. Axial Velocity Histograms around the Vortex Core Region at $x/L = 40\%$ for $\alpha = 30^\circ$.

which are not taken in sequence during a run, such as certain rows of vectors within the 20°, 80% chord survey. Areas where blocks of vectors within a field exhibit slightly different trends, such as the upper five rows of the 20°, 40% chord survey, represent data collected during separate runs.

As LV measurements are applied to increasingly complex, high speed flows, particle dynamic bias becomes a primary concern. Within the vortex, seed particles tend to be centrifuged away from the core. This causes the measured velocity of the seed to differ from the fluid streamlines it is modeling. Also, since the larger particles are centrifuged more easily than smaller ones, the population density and size distribution of the seed vary radially through a vortex. A noted decrease in data rate toward the vortex core indicates the presence of fewer, smaller particles.

A quantitative analysis of the particle dynamic bias for the 20° AOA flowfield is given by Maurice (Ref 11). By two methods of analysis, one which models the flowfield by an equivalent potential vortex, and one which uses a CFD flowfield solution, the measurement error is shown to increase nearly linearly with particle diameter. The actual particle size distribution of the silicon oil is unknown, although out-of-tunnel measurements have shown 98% of the seed to be less than 1.0 μm in diameter. The analytical analysis estimates that the seed must be less than 0.1 to 0.8 μm to assure dynamic bias of less than 3%. The analysis also shows that the inner core region did not maintain enough seed to make measurements, due to the inability of particles to remain in the core region as the vortex is formed, and due to particles outside of the viscous inner core being centrifuged as they travel downstream. Consequently, a specific estimation of

the particle dynamic bias requires precise knowledge of the particle diameter, and maintaining seed within the inner core cannot be accomplished by injecting the particles into the freestream flow.

Attempts to seed through the model into the vortex at its creation result in significant changes in the vortex structure. As a result, this is no longer a nonintrusive measurement and could not be correlated with computational analyses; hence, no data are presented from this seeding technique. Future tests will be conducted with tailored flow seeding through the model.

4.0 RESULTS

In general, 1500 samples are taken at each test location. However, at some locations, especially near the virtually unseeded vortex core, data rates are too slow to acquire the 1500 samples and the data collection is terminated after 3 minutes. Model interference with the laser beams limits access to some test locations near the surface of the model. These difficulties complicate the problem of defining the secondary vortices.

Two-dimensional velocity fields at 20° , 30° , and 35° AOA for 40% and 80% chord stations are shown in Figs. 13-17. The small isolated holes in the flow field represent instrumentation/computer errors. The large empty areas near the model surface are areas in, or around the vortex core where the LV seed material is centrifuged away from the vortex core. Also, there is a region along the surface where the laser beams intersect the model prior to the formation of the probe volume, restricting LV measurements in the primary vortex. Because of these two limitations, the secondary and tertiary vortices cannot be measured without set-up modifications that are being considered for further studies.

At 20° AOA, previous experiments and laser light sheet flow visualizations indicate that there is not any bursting of the vortices (Ref 12). Hence, the LV measurements provide more accurate statistical mean velocity fields at 20° AOA than at 30° or 35° AOA. At 40% chord the downward flow along the centerline indicates flow reattachment as illustrated in the schematic flow diagram (Fig. 10). The vertical vectors along the centerline in Figs. 13 and 14 clearly

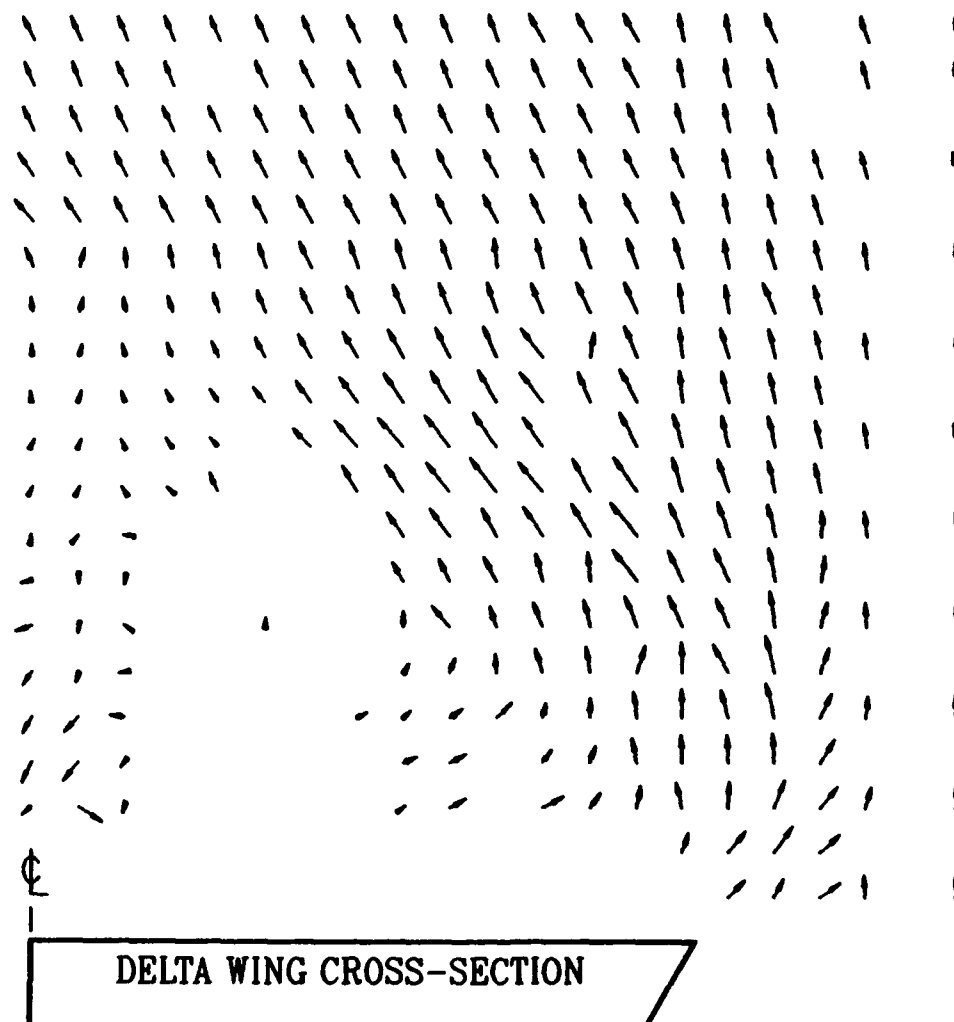


Fig. 13. Two-Dimensional Velocity Field at $x/L = 40\%$ for $\alpha = 20^\circ$.

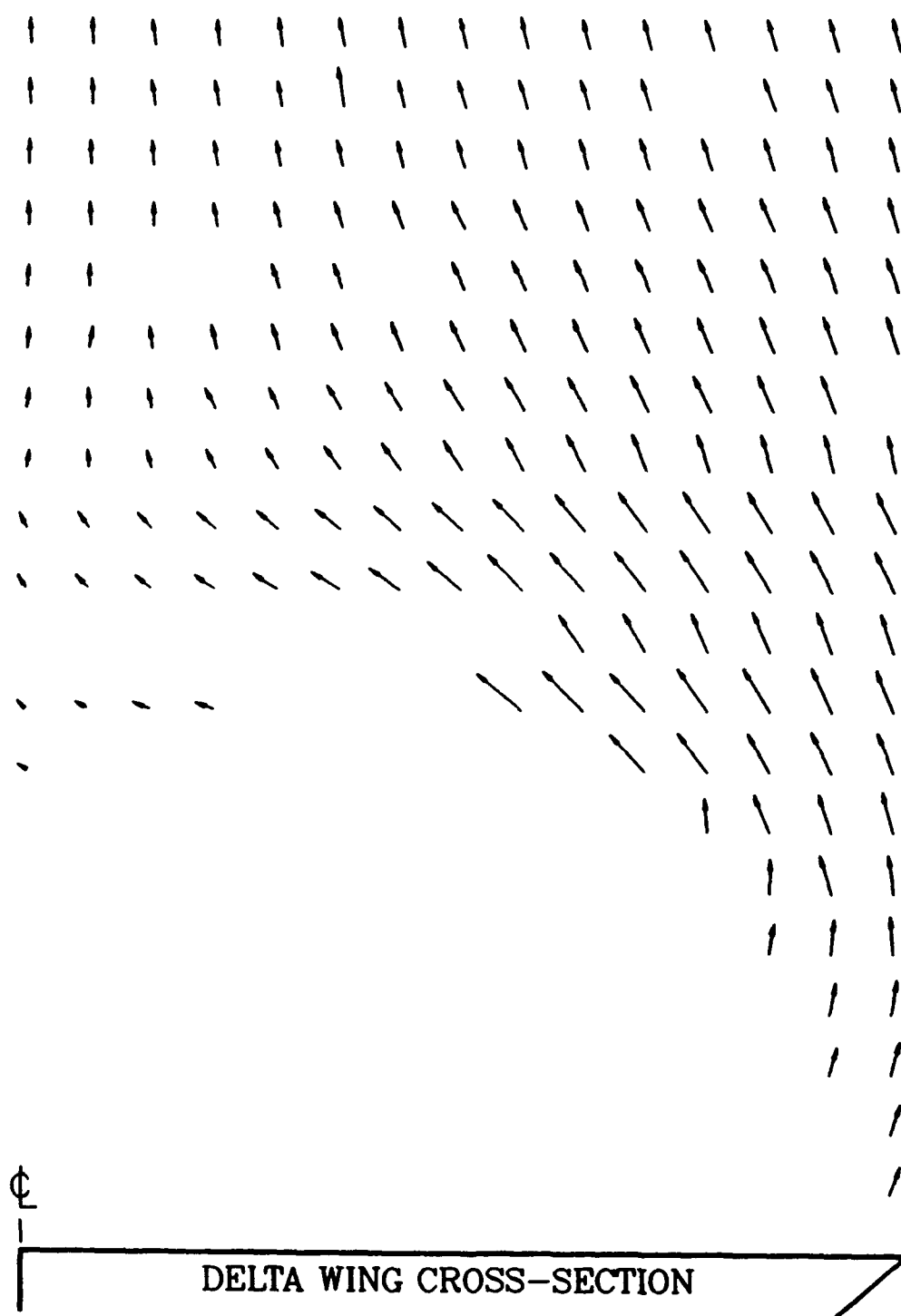


Fig. 14. Two-Dimensional Velocity Field at $x/L = 80\%$ for $\alpha = 20^\circ$.

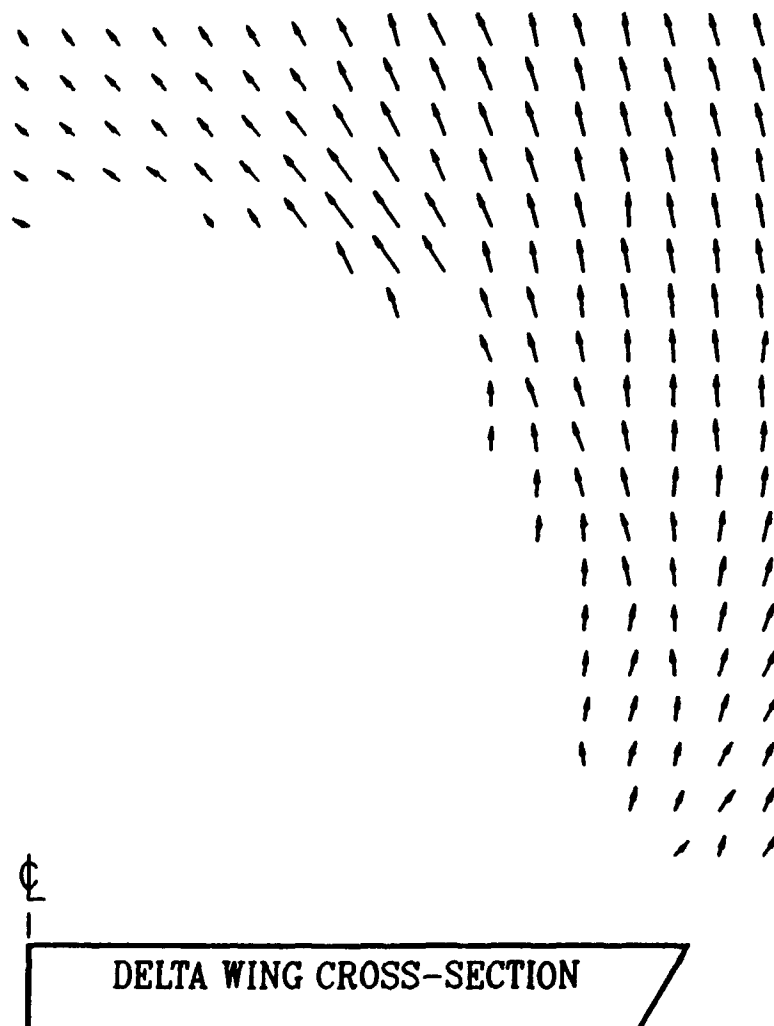


Fig. 15. Two-Dimensional Velocity Field at $x/L = 40\%$ for $\alpha = 30^\circ$.

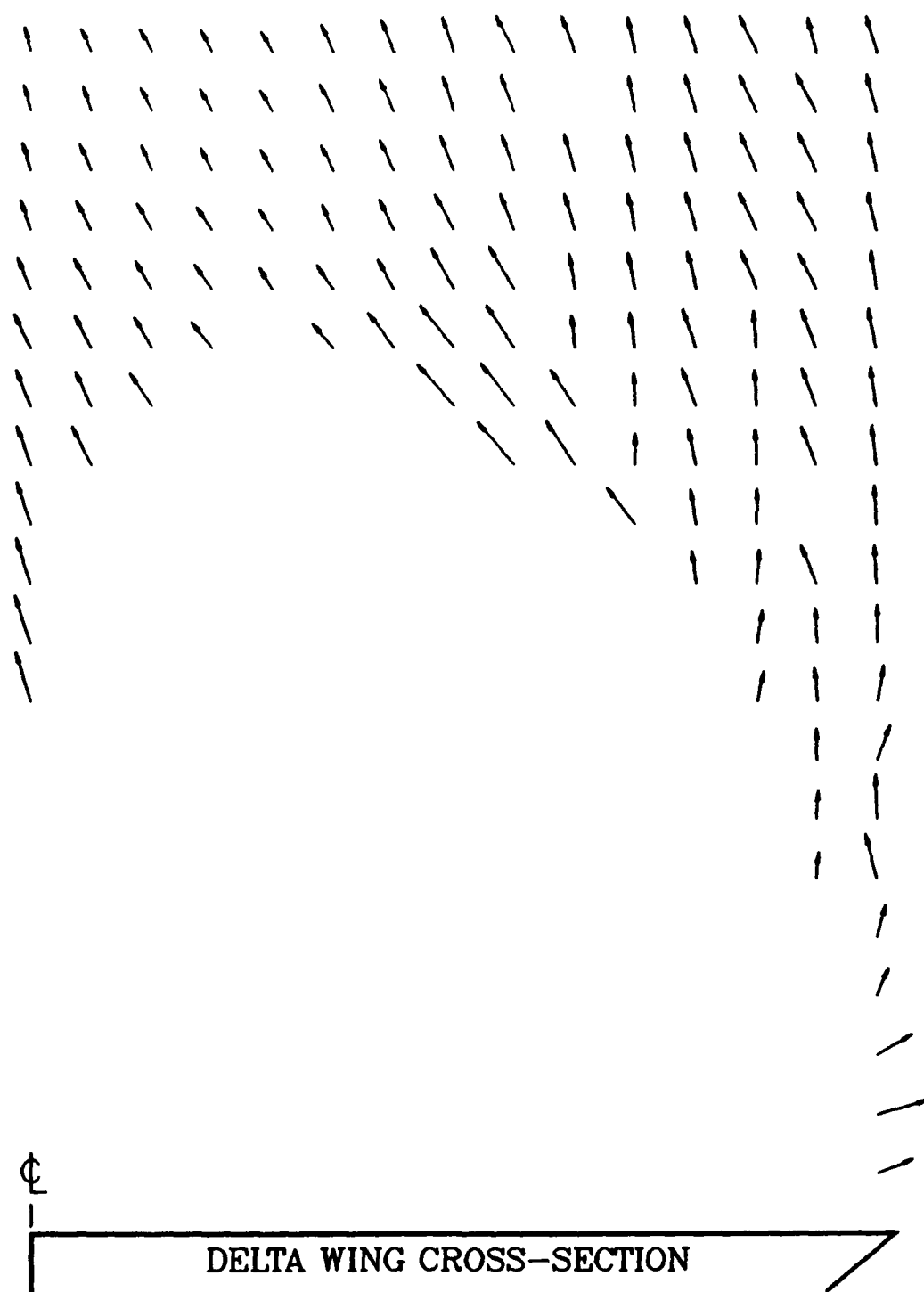


Fig. 16. Two-Dimensional Velocity Field at $x/L = 80\%$ for $\alpha = 30^\circ$.

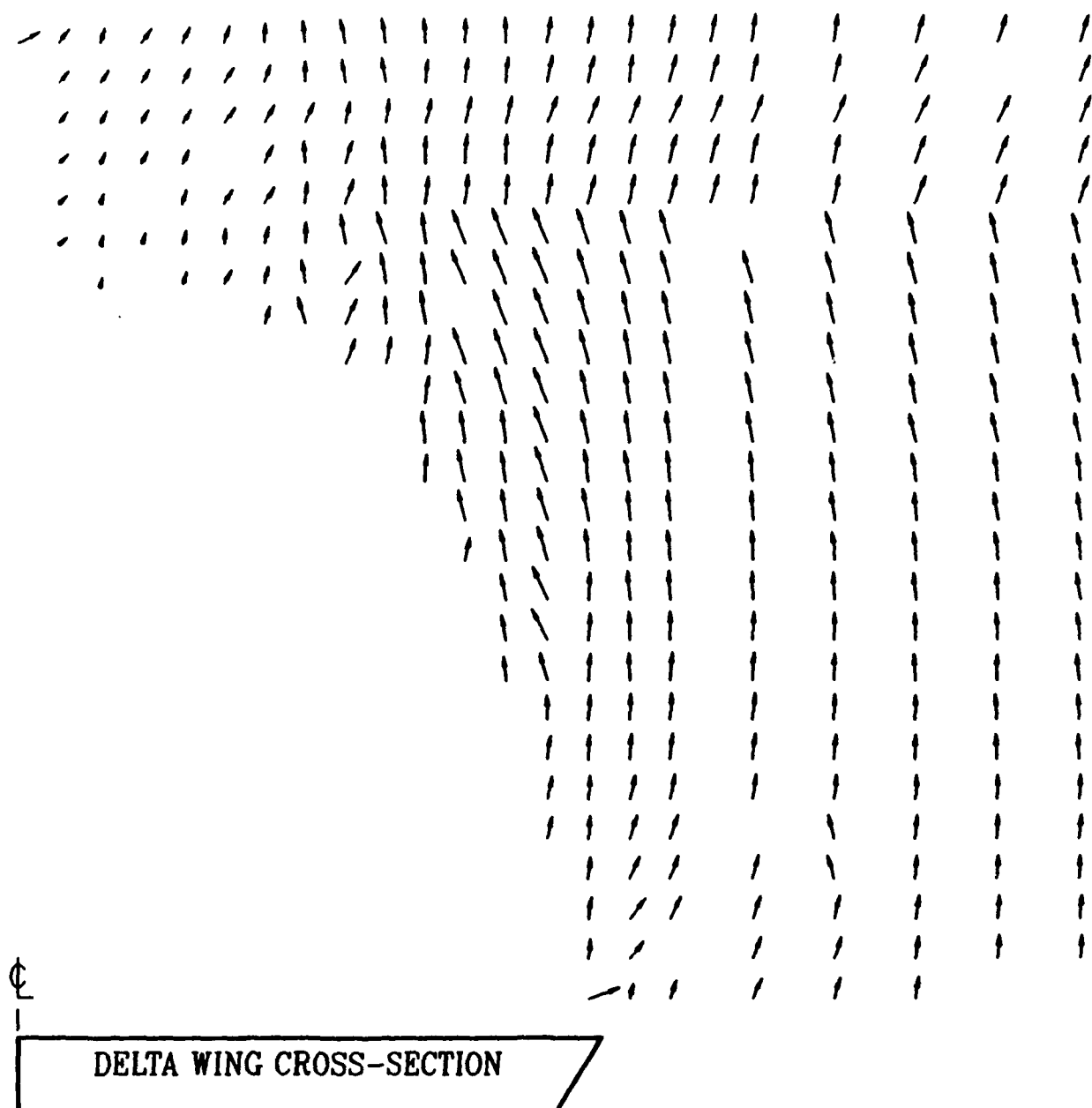


Fig. 17. Two-Dimensional Velocity Field at $x/L = 40\%$ for $\alpha = 35^\circ$.

show the symmetry of the flow. The quasi-randomness of the vectorfield at 35° AOA, 40% chord represents the vortex bursting. At 80% chord, the vortex bursting is too strong for this LV system to measure.

A representative velocity histogram of a single measurement component at a single location is shown in Fig. 18. After 1500 individual point measurements are made, the data are edited by eliminating the points which fall beyond 3 standard deviations of the mean. At this location 30 points are eliminated by this form of editing. The remaining 1470 points yield a mean velocity of 483.2 m/s with a standard deviation of 22.24 m/s. The ideal Gaussian distribution curve with the same mean and variance is superimposed over the data. At this point the skewness coefficient is -0.39, relative to a coefficient of zero for the ideal Gaussian curve. The kurtosis coefficient at this point is 2.82, compared to an ideal value of 3.00.

A 2-D velocity field for the 20° AOA, 80% chord survey where the data are rotated to a coordinate system which is axial and normal to the trajectory of the vortex core is presented in Fig. 19. Since the model is at a 20 degree angle-of-attack relative to the tunnel, and since the vortex core grows as it moves downstream along the model, the origin of the vortex is trajected at a lesser angle-of-attack than the wing. By extending "tails" from the smooth, unbiased velocity vectors as shown in the figure, a point of convergence defines the vortex origin. For a transformation angle greater than 8° (towards the 20° AOA), the lines converge to create a surface concave to the right. For an angle of less than 8°, the surface is concave towards the left. Since a small perturbation in vector orientation creates a large change in the

Axial Component w/r Tunnel
At Lower Outside Corner of Measurement Field
 $\alpha = 20^\circ \quad x/L = 0.4$

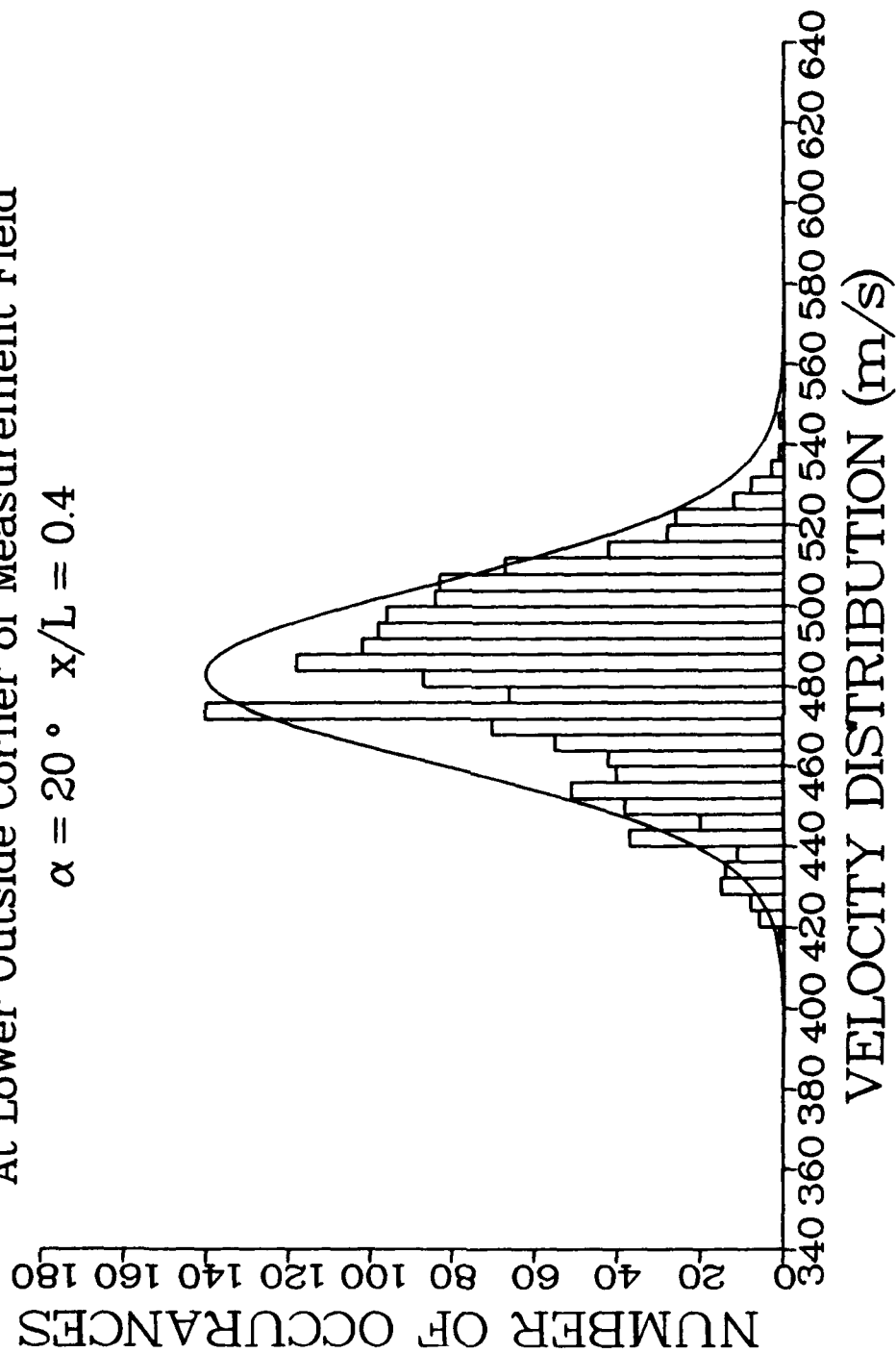


Fig. 18. Typical Velocity Histogram of Axial Component of Velocity.

$$\alpha = 20^\circ \quad x/L = 0.8$$

Transformation Angle = 8°

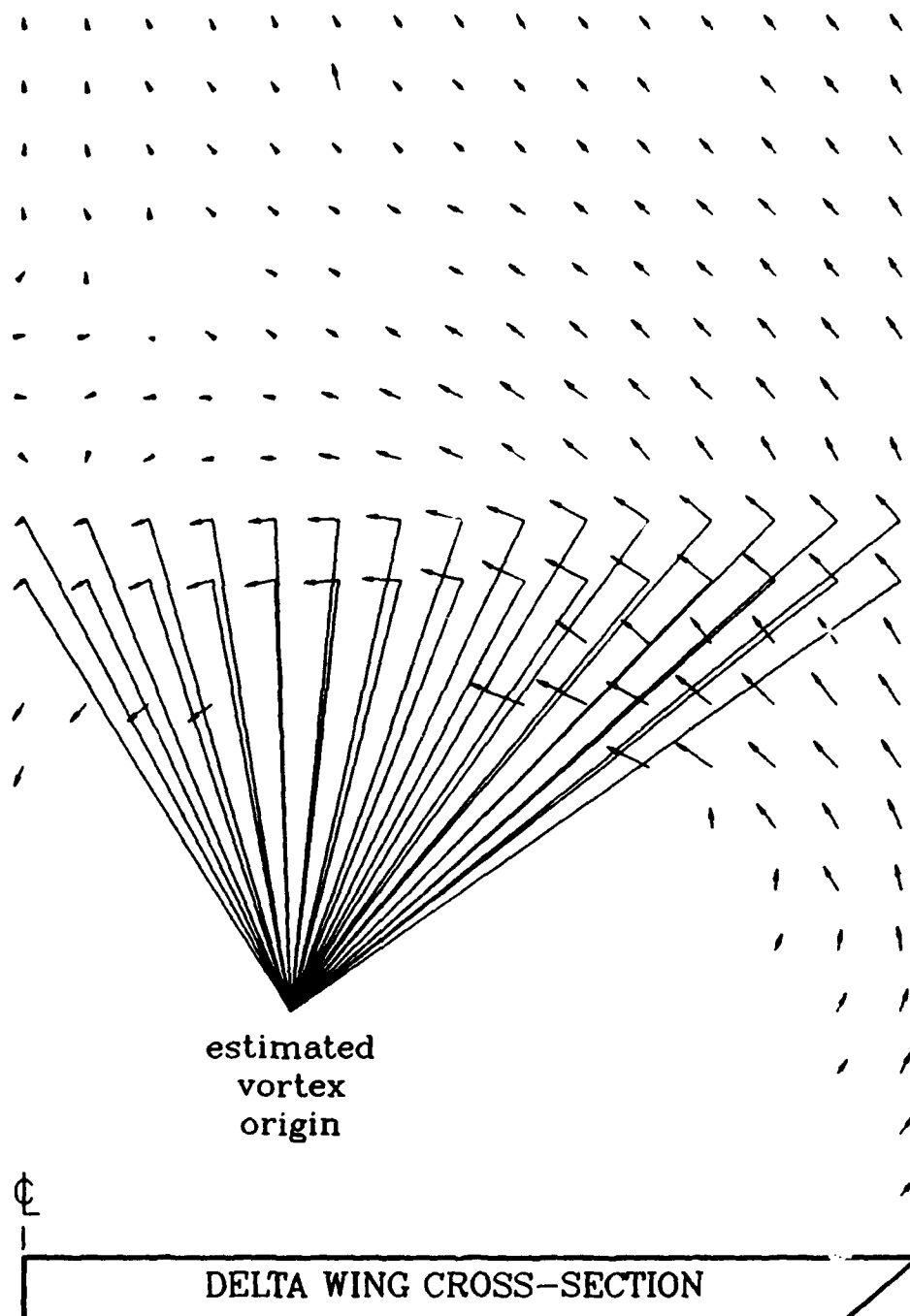


Fig. 19. Transformed Two-Dimensional Velocity Field Estimating Location of Vortex Origin at $x/L = 80\%$ for $\alpha = 20^\circ$.

position of its tail, this method requires very smooth, unbiased data to be effective. Slight changes in flowfield conditions over a long tunnel run are evidenced by different groups of vectors converging to different origins within the same velocity field. Knowing the position of the vortex origin allows each measurement location to be related to an ideal potential vortex strength. For this case, the potential vortex circulation increases from approximately 25 m²/s at the centerline to 100 m²/s at the outer edge of the measurement field.

A three-dimensional representation of the axial velocity component on the 40% chord plane at 20° AOA (Fig. 20) shows the momentum loss in the vortex region of the flowfield as evidenced by the decreasing magnitudes of the axial velocity. Figs. 21 and 22 quantitatively show the velocity trends in this flowfield.

U/U_{INF} versus Y/L for $Z/L = 0.007$ to 0.075 is shown in Fig. 21. In general, the ratio of U/U_{INF} increases as the distance normal to the model surface increases at all locations along the span. At the centerline of the model, the normalized axial velocity increases from near 0.9 to approximately 1.13 as Z/L increases from 0.007 to 0.052, and then the normalized axial velocity decreases to 1.00 as Z/L increases to 0.142 (the far field). Considering the first full set of data at $Z/L = 0.022$, it can be seen that the velocity is highest at the centerline and between 87% and 93% span and that this last location group represents a stagnation line between the primary and secondary vortices on an oil flow simulation. This compares qualitatively to the stagnation line on the simulated oil traces of Webster and Shang (Ref 13). At approximately 50% span, near the spanwise location of the vortex core, the normalized velocities increase from

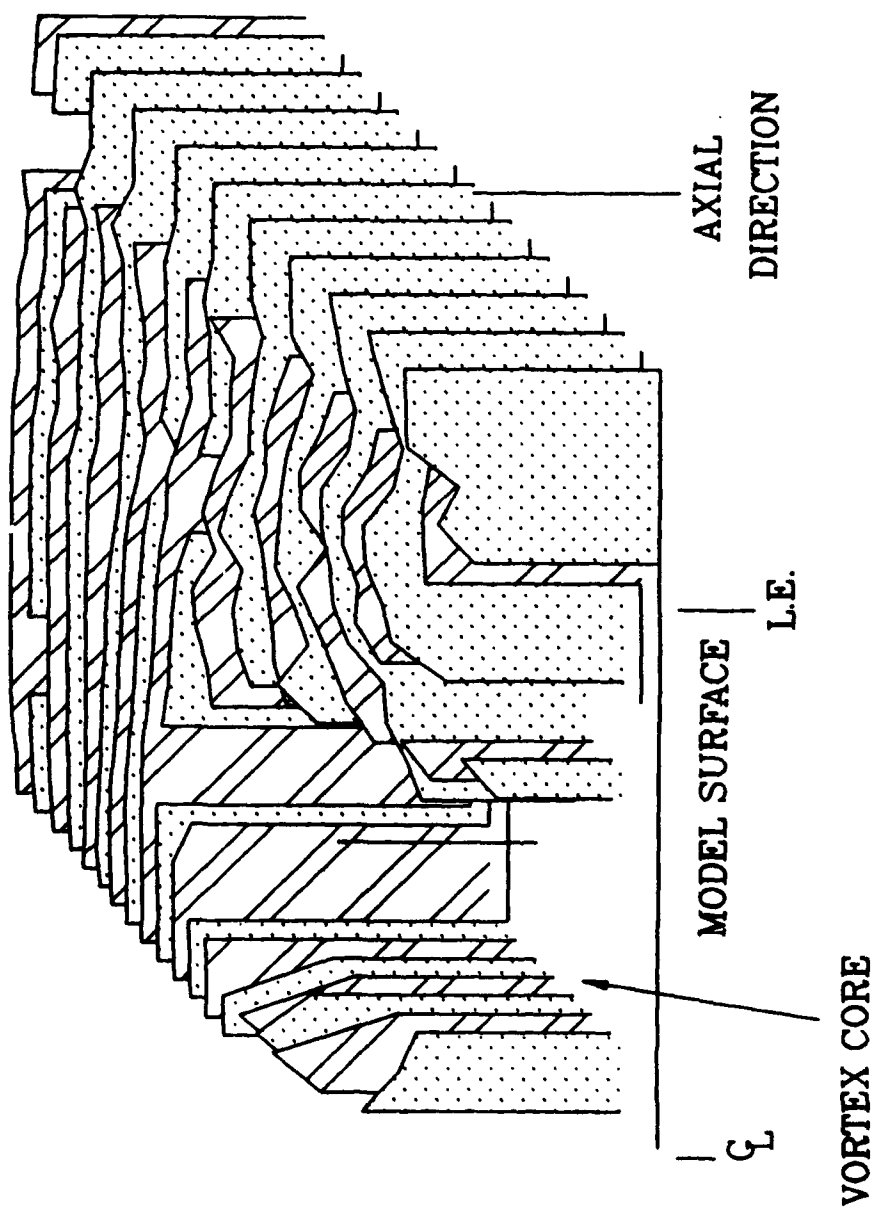


Fig. 20. Three-Dimensional Representation of Axial Velocity Component on the $x/L = 40\%$ Plane for $\alpha = 20^\circ$.

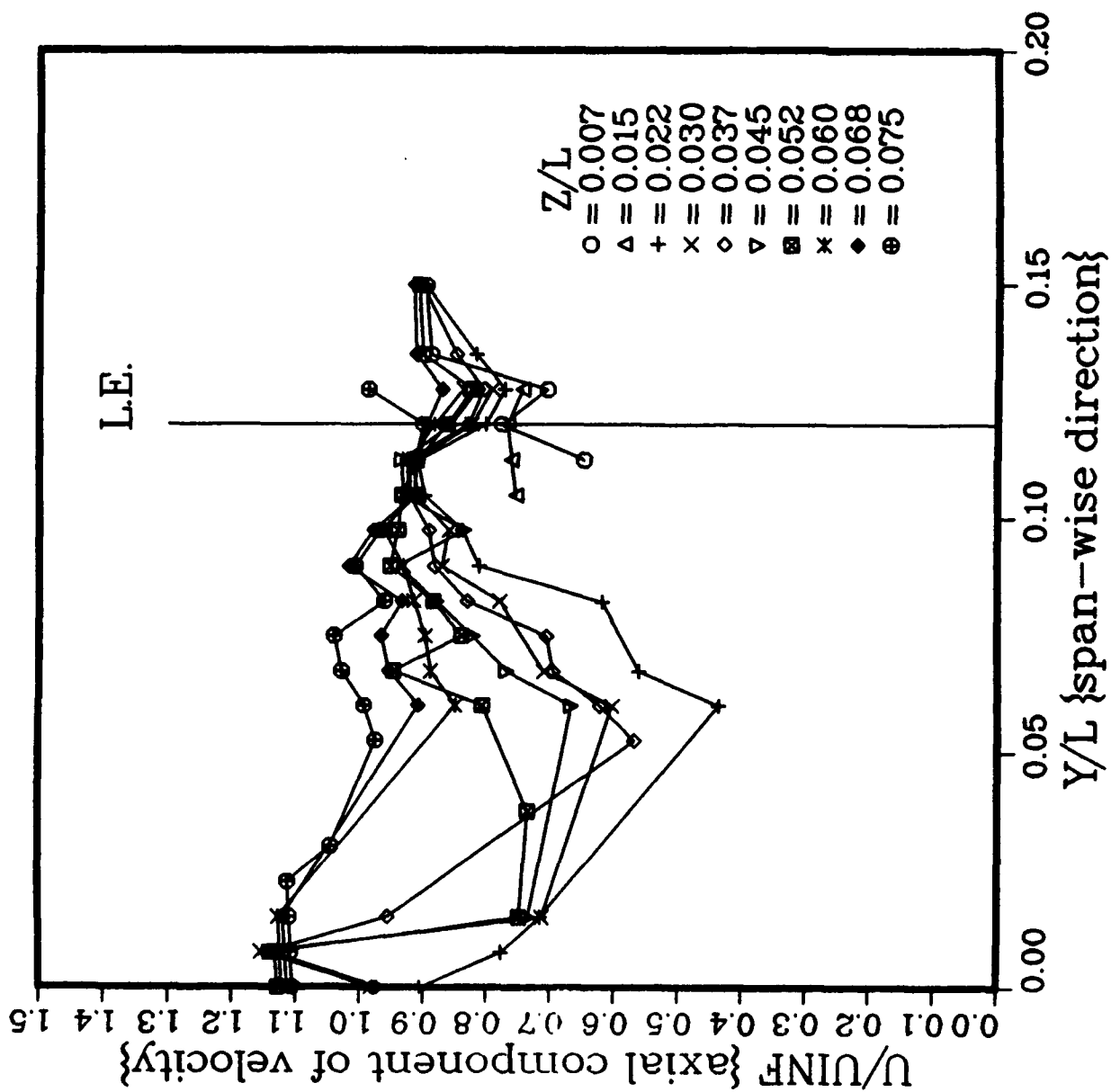


Fig. 21. Normalized Axial Velocity Component vs. Span-wise Distance on Model for $z = 0.25$ cm to $z = 2.54$ cm.

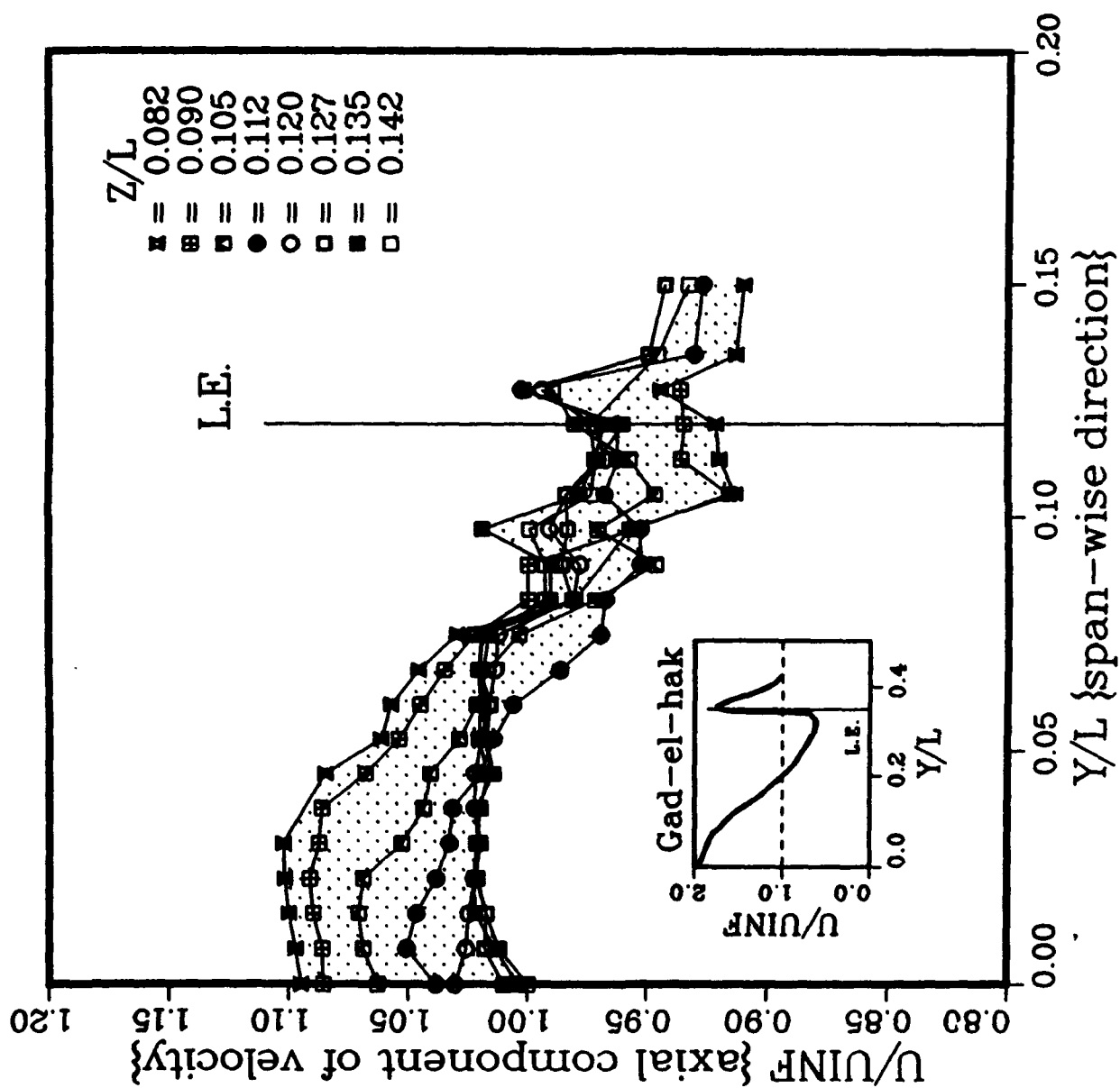


Fig. 22. Normalized Axial Velocity Component vs. Span-wise Distance on Model for $z = 2.79$ cm to $z = 4.83$ cm.

0.44 to 0.98 as Z/L increases from 0.008 to 0.075.

U/U_{INF} versus Y/L for $Z/L = 0.075$ to 0.142 is shown in Fig. 22. The band of normalized velocity ranges from 1.0 to 1.1 at the centerline of the model. The shaded band shows the velocity trends outside of the vortex core. This compares qualitatively with the results of Gad-el-Hak and Blackwelder (Ref 14, 15) for the subsonic delta wing flowfield near the model surface. The velocity decreases as the spanwise distance from the centerline increases, then rises significantly at the leading edge, and finally tapers off to approximately 95% of freestream velocity just off the edge of the model.

5.0 CONCLUSIONS

An experimental study was conducted to measure velocities in the vortices generated by a sharp leading edge 75° delta wing at Mach 1.9 for angles of attack up to 35° . Three-dimensional laser velocimeter measurements were made to define the vortex structure prior to bursting at several chord locations as part of an ongoing and developing project for computational fluid dynamics code verification and validation. Qualitative comparisons between experimental data and CFD results show good agreement on defining the region between the primary and secondary vortices. However, the CFD solutions revealed no evidence of vortex breakdown which was visualized using a laser light sheet and seen at 30° angle of attack and 80% chord. An analysis of the light sheet results is ongoing. Comparison of test characteristics and results with the vortex classification plot of Miller and Wood (Ref 5) show that the classification graph can be extended to higher normalized angle of attack in the classical vortex region. Measurements of the vortex core are shown to be limited by the lack of seed material entrained in the vortex and by the centrifugal effect of the vortex on the seed material. Additional experiments are planned with tailored flow seeding through the model and enhanced electronic equipment to further define the vortex structure, including secondary and tertiary vortices, turbulence, and stability.

6.0 RECOMMENDATIONS

Recommendations for this program include improving seeding techniques and a better mixing of electronic equipment. As a result of this experimental study, the techniques of particle dynamics was developed by Maurice (Ref 11, see Appendix B). With this additional analysis technique, experimental studies with different seeding techniques and seed particles can be conducted to optimize particle tracking and bias. Also, the current experiments showed that use of a Fast Fourier Transform processor for the weaker laser velocimetry components allowed those measurements which were unobtainable with the counterprocessors. At the time of these experiments, only one FFT processor could reasonably be used, but now the equipment exists to perform this study using three FFT processors to collect coincident data. With coincident data, additional turbulence quantities can be determined from the data. Also, much more thorough data collection could be made if unlimited wind tunnel time was available (but that's just an experimenter dreaming).

7.0 REFERENCES

1. Weissman, C.B., "Three-Component Laser Velocimeter Developments with a Unique Method of Data Presentation," AIAA Paper No. 84-1539, AIAA 17th Fluid Dynamics, Plasma Dynamics, and Lasers Conference, Snowmass CO, June 25-27, 1984.
2. Yanta, W.J. and Wardlaw, A.B., "Laser Doppler Velocimeter Measurements of Leeward Flowfields on Slender Bodies at Large Angle-of-Attack," AIAA Paper No. 77-660, AIAA 10th Fluid & Plasmadynamics Conference, Albuquerque NM, June 27-29, 1977.
3. Owen, F.K. and Johnson, D.A., "Wake Vortex Measurements of Bodies at High Angle of Attack," AIAA Paper No. 78-23, AIAA 16th Aerospace Sciences Meeting, Huntsville AL, January 16-18, 1978.
4. Schwind, R.G. and Mullen, J. Jr, "Laser Velocimeter Measurements of Slender-Body Wake Vortices," AIAA Paper No. 79-0302, 17th Aerospace Sciences Meeting, New Orleans LA, January 15-17, 1979.
5. Miller, D.S. and Wood, R.M., "Lee-Side Flow Over Delta Wings at Supersonic Speeds," NASA Technical Paper No. 2430, June 1985.

6. McMillin, S.N., Pittman, J.L., and Thomas, J.L., "A Computational Study of Incipient Leading-Edge Separation on a 65° Delta Wing at $M = 1.60$," AIAA Paper No. 90-3029-CP, AIAA 8th Applied Aerodynamics Conference, Portland OR, August 20-22, 1990.
7. Webster, W.P., and Shang, J.S., "Numerical Simulation of Reversed Flow over a Supersonic Delta Wing at High Angle of Attack," AIAA Paper No. 89-1802, AIAA 20th Fluid Dynamics, Plasma Dynamics and Lasers Conference, Buffalo NY, June 12-14, 1989.
8. Parobek, D.M., Boyer, D.L., and Clinihens, G.A., "Recent Developments in Liquid Flow Seeding Techniques for Use with LV Measurements," AIAA Paper No. 86-0769, AIAA 14th Aerodynamic Testing Conference, West Palm Beach FL, March 5-7, 1986.
9. Jones, G.S., Kamemoto, D.Y., and Gartrell, L.R., "An Investigation of the Effects of Seeding in Laser Velocimeter Systems," AIAA Paper No. 90-0502, 28th Aerospace Sciences Meeting, Reno NV, January 8-11, 1990.
10. Edwards, R.V., "Report of the Special Panel on Statistical Particle Bias Problems in Laser Anemometry," Journal of Fluids Engineering, (June 1987) Vol. 109, 89.
11. Maurice, M.S., "Laser Velocimetry Seed Particles Within Compressible, Vortical Flows," AIAA Journal, Vol. 30, No. 2, pp. 376, February 1992.

12. Guyton, R.W., private communications, Flight Dynamics Directorate, Wright Laboratory, Wright-Patterson Air Force Base OH, 1989.

13. Webster, W.P., and Shang, J.S., "Thin Layer and Full Navier-Stokes Simulations Over a Supersonic Delta Wing," AIAA Journal, Vol. 29, No. 9, pp. 1363, September 1991.

14. Gad-el-Hak, M., and Blackwelder, R.F., "The Discrete Vortices from a Delta Wing," AIAA J. (1985) Vol. 23 No. 6, 961.

15. Gad-el-Hak, M., and Blackwelder, R.F., "Control of the Discrete Vortices from a Delta Wing," AIAA J. (1987) Vol. 25 No. 8, 1042.

APPENDIX A: QUANTITATIVE RESULTS

This appendix contains the numerical results of the laser velocimetry measurements for 20° AOA, 40% chord; 20° AOA, 80% chord; 30° AOA, 40% chord; 30° AOA, 80% chord; and 35°, 40% chord. The coordinates and velocities are presented in the model coordinate system as shown in Fig.A-1. The coordinates x, y, and z are given in meters and the respective velocity components u, v, and w are given in meters per second. Any locations where no results are given were locations where the data are invalid, not acquired due to electronic errors, or not acquired due to particle dynamics.

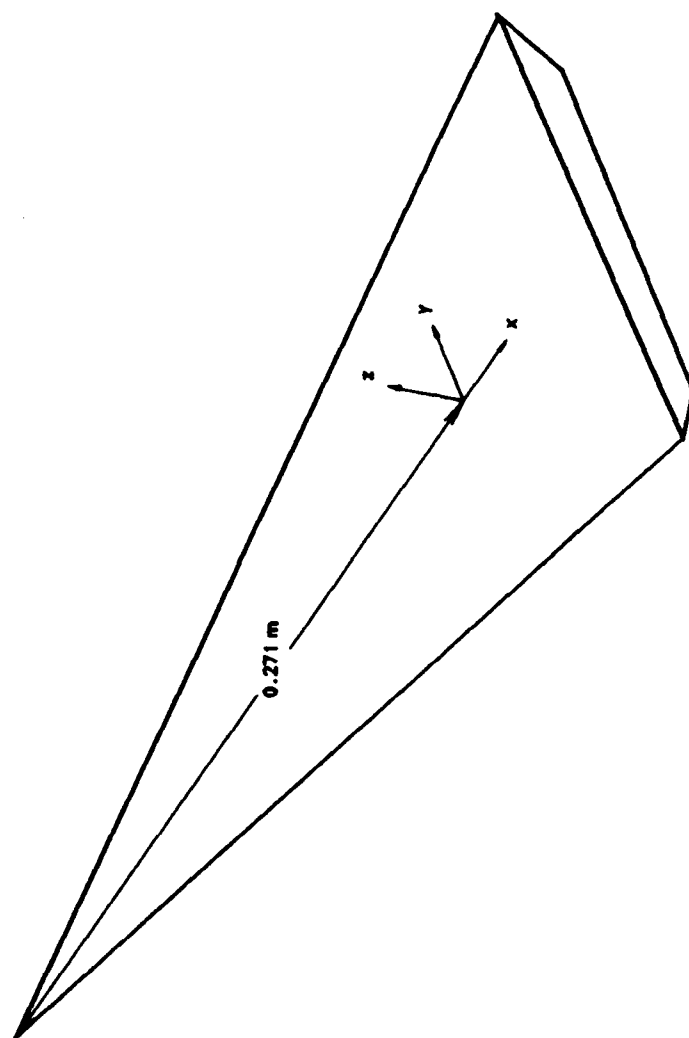


Fig. A-1. Model Coordinate System.

Table A-1: Experimental Data for 20° Angle of Attack, 40% Chord.

x (m)	y (m)	z (m)	u (m/s)	v (m/s)	w (m/s)
-0.1357	0.0508	0.0025	137.75	0.19	52.25
-0.1357	0.0508	0.0076	137.59	-0.48	52.97
-0.1357	0.0508	0.0127	138.42	-3.80	54.02
-0.1357	0.0508	0.0178	139.34	-4.75	54.98
-0.1357	0.0508	0.0229	140.44	-6.44	55.86
-0.1357	0.0508	0.0279	139.66	-9.89	55.70
-0.1357	0.0508	0.033	139.62	-4.02	55.62
-0.1357	0.0508	0.0381	142.26	-6.71	56.45
-0.1357	0.0508	0.0432	144.66	-14.09	57.40
-0.1357	0.0508	0.0483	143.18	-11.55	56.84
-0.1357	0.0508	0.0508	143.36	-13.01	56.99
-0.1357	0.0457	0.0025	136.47	-2.02	51.65
-0.1357	0.0457	0.0076	125.50	12.93	48.36
-0.1357	0.0457	0.0127	130.26	5.03	51.80
-0.1357	0.0457	0.0178	138.50	-4.40	55.93
-0.1357	0.0457	0.0229	140.11	-6.10	56.86
-0.1357	0.0457	0.0279	140.15	-7.30	56.77
-0.1357	0.0457	0.033	139.59	-5.85	56.14
-0.1357	0.0457	0.0381	142.79	-7.81	57.14
-0.1357	0.0457	0.0432	145.71	-15.66	58.17
-0.1357	0.0457	0.0483	145.14	-14.68	57.82
-0.1357	0.0457	0.0508	146.25	-19.04	58.17
-0.1357	0.0432	0.0025	108.31	45.02	33.63
-0.1357	0.0432	0.0051	114.26	44.66	41.72
-0.1357	0.0432	0.0076	118.52	39.66	48.65

x (m)	y (m)	z (m)	u (m/s)	v (m/s)	w (m/s)
-0.1357	0.0432	0.0102	121.49	32.16	53.55
-0.1357	0.0432	0.0127	123.61	24.82	57.08
-0.1357	0.0432	0.0152	125.15	17.95	57.54
-0.1357	0.0432	0.0178	126.35	12.43	57.77
-0.1357	0.0432	0.0203	128.52	7.82	58.57
-0.1357	0.0432	0.0229	133.71	1.88	58.05
-0.1357	0.0432	0.0254	151.52	-14.79	63.17
-0.1357	0.0432	0.0279	144.95	-13.55	60.78
-0.1357	0.0432	0.0305	143.67	-12.82	60.31
-0.1357	0.0432	0.033	145.45	-13.97	60.33
-0.1357	0.0432	0.0356	151.90	-16.51	62.98
-0.1357	0.0432	0.0381	153.95	-15.87	62.58
-0.1357	0.0432	0.0407	152.64	-20.42	61.85
-0.1357	0.0432	0.0432	153.80	-20.22	61.99
-0.1357	0.0407	0.0025	119.34	19.96	42.69
-0.1357	0.0407	0.0051	118.10	39.48	59.92
-0.1357	0.0407	0.0076	123.21	22.03	63.73
-0.1357	0.0407	0.0102	126.62	-4.44	65.84
-0.1357	0.0407	0.0127	127.48	-19.70	77.66
-0.1357	0.0407	0.0152	131.66	-21.06	81.82
-0.1357	0.0407	0.0178	132.63	-13.25	79.34
-0.1357	0.0407	0.0203	135.77	-15.60	74.93
-0.1357	0.0407	0.0229	137.52	-17.66	71.67
-0.1357	0.0407	0.0254	138.38	-16.29	70.13
-0.1357	0.0407	0.0279	141.44	-16.09	69.11
-0.1357	0.0407	0.0305	143.47	-14.78	66.44

x (m)	y (m)	z (m)	u (m/s)	v (m/s)	w (m/s)
-0.1357	0.0407	0.033	145.05	-15.48	65.30
-0.1357	0.0407	0.0356	150.51	-27.23	66.89
-0.1357	0.0407	0.0381	147.75	-17.96	63.71
-0.1357	0.0407	0.0407	149.24	-18.00	63.14
-0.1357	0.0407	0.0432	147.40	-18.55	62.05
-0.1357	0.0407	0.0457	148.63	-16.30	61.96
-0.1357	0.0407	0.0483	149.53	-19.37	62.19
-0.1357	0.0407	0.0508	152.05	-26.72	62.50
-0.1357	0.0381	0.0025	99.49	35.96	39.11
-0.1357	0.0381	0.0051	117.01	38.12	48.95
-0.1357	0.0381	0.0076	139.57	3.04	58.84
-0.1357	0.0381	0.0102	140.43	-2.02	61.57
-0.1357	0.0381	0.0127	142.08	-16.29	63.20
-0.1357	0.0381	0.0152	143.52	-33.48	63.20
-0.1357	0.0381	0.0178	139.91	-27.31	62.98
-0.1357	0.0381	0.0203	141.75	-32.05	71.89
-0.1357	0.0381	0.0229	139.80	-22.69	76.14
-0.1357	0.0381	0.0254	140.34	-24.55	73.22
-0.1357	0.0381	0.0279	141.19	-16.08	70.32
-0.1357	0.0381	0.0305	143.63	-16.32	69.33
-0.1357	0.0381	0.033	144.91	-18.21	66.40
-0.1357	0.0381	0.0356	146.96	-8.28	61.58
-0.1357	0.0381	0.0381	147.73	-11.47	63.44
-0.1357	0.0381	0.0407	148.49	-12.74	63.11
-0.1357	0.0381	0.0432	148.98	-13.62	62.44
-0.1357	0.0381	0.0457	149.19	-12.44	62.07

x (m)	y (m)	z (m)	u (m/s)	v (m/s)	w (m/s)
-0.1357	0.0381	0.0483	149.13	-12.01	61.53
-0.1357	0.0381	0.0508	148.52	-10.06	61.00
-0.1357	0.0356	0.0051	115.91	13.53	44.94
-0.1357	0.0356	0.0076	137.88	-13.44	55.93
-0.1357	0.0356	0.0102	140.27	-2.95	61.22
-0.1357	0.0356	0.0127	141.80	-1.25	64.47
-0.1357	0.0356	0.0152	143.17	-3.49	66.34
-0.1357	0.0356	0.0178	143.45	-31.39	67.60
-0.1357	0.0356	0.0203	141.40	-32.66	68.99
-0.1357	0.0356	0.0229	140.40	-28.31	73.16
-0.1357	0.0356	0.0254	139.89	-23.58	76.41
-0.1357	0.0356	0.0279	140.20	-22.04	72.69
-0.1357	0.0356	0.0305	140.55	-8.09	70.70
-0.1357	0.0356	0.033	142.82	-8.30	67.02
-0.1357	0.0356	0.0356	145.33	-9.14	64.86
-0.1357	0.0356	0.0381	148.56	-20.04	64.36
-0.1357	0.0356	0.0407	150.97	-25.05	65.30
-0.1357	0.0356	0.0432	151.06	-26.00	63.91
-0.1357	0.0356	0.0457	150.16	-18.59	62.27
-0.1357	0.0356	0.0483	149.41	-12.01	61.37
-0.1357	0.0356	0.0508	149.46	-12.00	61.16
-0.1357	0.033	0.0076	128.76	7.27	49.34
-0.1357	0.033	0.0102	131.97	-10.23	52.86
-0.1357	0.033	0.0127	136.80	-8.10	59.35
-0.1357	0.033	0.0152	128.32	16.30	59.85
-0.1357	0.033	0.0178	144.37	-26.94	67.09

x (m)	y (m)	z (m)	u (m/s)	v (m/s)	w (m/s)
-0.1357	0.033	0.0203	147.73	-52.75	70.49
-0.1357	0.033	0.0229	150.17	-57.29	74.37
-0.1357	0.033	0.0254	148.52	-50.43	76.09
-0.1357	0.033	0.0279	146.95	-38.08	75.97
-0.1357	0.033	0.0305	146.75	-38.08	74.17
-0.1357	0.033	0.033	146.88	-27.69	70.13
-0.1357	0.033	0.0356	149.00	-28.71	68.33
-0.1357	0.033	0.0381	146.27	-22.59	64.36
-0.1357	0.033	0.0407	152.15	-30.96	61.88
-0.1357	0.033	0.0432	150.96	-30.20	61.13
-0.1357	0.033	0.0457	156.47	-23.28	61.93
-0.1357	0.033	0.0483	153.43	-33.03	62.61
-0.1357	0.033	0.0508	153.94	-32.03	62.02
-0.1357	0.0305	0.0076	124.55	22.83	32.77
-0.1357	0.0305	0.0102	133.61	11.02	36.72
-0.1357	0.0305	0.0127	135.41	0.60	43.41
-0.1357	0.0305	0.0152	144.19	-9.25	57.13
-0.1357	0.0305	0.0178	146.08	-14.33	59.84
-0.1357	0.0305	0.0203	142.93	-6.13	64.99
-0.1357	0.0305	0.0229	156.01	-39.50	71.20
-0.1357	0.0305	0.0254	154.59	-37.78	74.01
-0.1357	0.0305	0.0305	153.49	-27.45	67.13
-0.1357	0.0305	0.033	136.11	7.13	56.61
-0.1357	0.0305	0.0356	145.27	-30.62	68.53
-0.1357	0.0305	0.0381	146.24	-21.22	65.04
-0.1357	0.0305	0.0407	150.18	-24.68	60.90

x (m)	y (m)	z (m)	u (m/s)	v (m/s)	w (m/s)
-0.1357	0.0305	0.0432	151.33	-26.21	61.21
-0.1357	0.0305	0.0457	152.03	-28.37	61.22
-0.1357	0.0305	0.0483	152.39	-27.72	61.29
-0.1357	0.0305	0.0508	153.70	-32.59	61.72
-0.1357	0.0279	0.0076	95.05	44.02	24.02
-0.1357	0.0279	0.0102	119.68	17.72	29.18
-0.1357	0.0279	0.0127	127.39	5.45	33.79
-0.1357	0.0279	0.0152	134.93	-18.15	52.66
-0.1357	0.0279	0.0178	135.78	-22.17	54.39
-0.1357	0.0279	0.0203	140.52	-16.96	61.55
-0.1357	0.0279	0.0229	143.49	-41.37	64.87
-0.1357	0.0279	0.0254	147.65	-52.98	66.12
-0.1357	0.0279	0.0279	150.47	-42.94	66.23
-0.1357	0.0279	0.0305	153.51	-49.91	66.47
-0.1357	0.0279	0.033	152.41	-47.95	65.00
-0.1357	0.0279	0.0356	149.16	-27.40	64.74
-0.1357	0.0279	0.0381	148.49	-16.79	63.33
-0.1357	0.0279	0.0407	150.57	-28.79	61.18
-0.1357	0.0279	0.0432	150.68	-28.80	61.14
-0.1357	0.0279	0.0457	152.06	-28.55	61.35
-0.1357	0.0279	0.0483	152.39	-27.07	61.23
-0.1357	0.0279	0.0508	153.23	-33.18	61.43
-0.1357	0.0254	0.0127	108.28	33.73	33.28
-0.1357	0.0254	0.0152	126.09	-2.66	41.23
-0.1357	0.0254	0.0178	128.80	-14.02	45.61
-0.1357	0.0254	0.0203	137.72	-27.29	55.03

x (m)	y (m)	z (m)	u (m/s)	v (m/s)	w (m/s)
-0.1357	0.0254	0.0229	148.34	-30.13	62.65
-0.1357	0.0254	0.0254	159.63	-56.96	75.79
-0.1357	0.0254	0.0279	158.04	-49.90	76.00
-0.1357	0.0254	0.0305	156.91	-39.88	73.92
-0.1357	0.0254	0.033	155.45	-29.78	70.89
-0.1357	0.0254	0.0356	154.05	-21.75	68.15
-0.1357	0.0254	0.0381	148.80	-7.06	64.23
-0.1357	0.0254	0.0407	155.41	-30.55	62.66
-0.1357	0.0254	0.0432	156.41	-30.18	61.98
-0.1357	0.0254	0.0457	156.43	-23.47	61.19
-0.1357	0.0254	0.0483	155.98	-24.12	60.55
-0.1357	0.0254	0.0508	156.05	-20.06	59.97
-0.1357	0.0229	0.0076	86.20	34.77	19.91
-0.1357	0.0229	0.0102	108.94	34.26	18.78
-0.1357	0.0229	0.0127	106.75	26.68	19.77
-0.1357	0.0229	0.0152	118.00	9.97	34.31
-0.1357	0.0229	0.0178	145.49	-40.11	47.77
-0.1357	0.0229	0.0203	136.51	-24.61	51.45
-0.1357	0.0229	0.0229	146.52	-43.38	61.86
-0.1357	0.0229	0.0254	157.93	-51.69	65.39
-0.1357	0.0229	0.0279	160.52	-55.41	71.75
-0.1357	0.0229	0.0305	158.81	-43.58	70.27
-0.1357	0.0229	0.033	157.33	-33.36	67.98
-0.1357	0.0229	0.0356	156.10	-26.08	66.55
-0.1357	0.0229	0.0381	151.41	-22.25	62.35
-0.1357	0.0229	0.0407	155.59	-32.72	62.16

x (m)	y (m)	z (m)	u (m/s)	v (m/s)	w (m/s)
-0.1357	0.0229	0.0432	156.57	-32.24	61.38
-0.1357	0.0229	0.0457	156.69	-28.35	60.72
-0.1357	0.0229	0.0483	156.37	-22.14	60.34
-0.1357	0.0229	0.0508	156.15	-23.48	59.76
-0.1357	0.0203	0.0076	66.92	6.80	5.40
-0.1357	0.0203	0.0102	92.62	30.39	13.92
-0.1357	0.0203	0.0127	95.51	16.00	17.39
-0.1357	0.0203	0.0152	102.27	13.05	20.75
-0.1357	0.0203	0.0178	123.79	-2.15	35.74
-0.1357	0.0203	0.0203	130.27	-25.28	44.40
-0.1357	0.0203	0.0229	139.34	-35.83	54.21
-0.1357	0.0203	0.0254	152.45	-39.85	59.89
-0.1357	0.0203	0.0279	162.30	-55.66	65.76
-0.1357	0.0203	0.0305	160.41	-43.58	64.72
-0.1357	0.0203	0.033	159.05	-35.10	63.75
-0.1357	0.0203	0.0356	156.73	-26.48	63.51
-0.1357	0.0203	0.0381	154.45	-18.89	62.90
-0.1357	0.0203	0.0407	156.01	-30.83	61.38
-0.1357	0.0203	0.0432	155.90	-29.80	60.63
-0.1357	0.0203	0.0457	156.54	-22.87	60.16
-0.1357	0.0203	0.0483	156.34	-24.64	59.76
-0.1357	0.0203	0.0508	156.34	-22.97	59.30
-0.1357	0.0178	0.0127	87.36	21.48	12.51
-0.1357	0.0178	0.0254	149.66	-32.93	58.33
-0.1357	0.0178	0.0279	162.95	-49.64	59.54
-0.1357	0.0178	0.0305	161.76	-39.50	57.22

x (m)	y (m)	z (m)	u (m/s)	v (m/s)	w (m/s)
-0.1357	0.0178	0.033	160.05	-33.67	58.33
-0.1357	0.0178	0.0356	157.87	-26.36	59.31
-0.1357	0.0178	0.0381	155.70	-20.25	60.11
-0.1357	0.0178	0.0407	156.51	-32.69	60.58
-0.1357	0.0178	0.0432	156.16	-29.55	59.86
-0.1357	0.0178	0.0457	156.63	-28.63	59.55
-0.1357	0.0178	0.0483	156.21	-25.65	59.17
-0.1357	0.0178	0.0508	156.02	-26.38	58.53
-0.1357	0.0152	0.0279	166.49	-39.64	41.94
-0.1357	0.0152	0.0305	163.94	-33.25	47.60
-0.1357	0.0152	0.033	161.33	-28.99	53.01
-0.1357	0.0152	0.0356	159.71	-25.37	55.85
-0.1357	0.0152	0.0381	156.52	-27.82	57.48
-0.1357	0.0152	0.0407	156.87	-32.92	59.38
-0.1357	0.0152	0.0432	155.69	-28.86	58.81
-0.1357	0.0152	0.0457	156.09	-27.58	58.66
-0.1357	0.0152	0.0483	155.88	-27.40	58.31
-0.1357	0.0152	0.0508	156.08	-23.44	58.06
-0.1357	0.0127	0.0178	112.85	2.22	20.67
-0.1357	0.0127	0.0305	166.72	-25.75	34.12
-0.1357	0.0127	0.033	163.16	-22.38	44.13
-0.1357	0.0127	0.0356	160.18	-20.16	50.80
-0.1357	0.0127	0.0381	158.30	-17.20	53.80
-0.1357	0.0127	0.0407	156.88	-29.22	58.09
-0.1357	0.0127	0.0432	156.77	-28.04	57.87
-0.1357	0.0127	0.0457	156.54	-26.86	57.97

x (m)	y (m)	z (m)	u (m/s)	v (m/s)	w (m/s)
-0.1357	0.0127	0.0483	156.62	-25.93	57.83
-0.1357	0.0127	0.0508	156.31	-23.21	57.47
-0.1357	0.0102	0.0254	160.46	-19.10	42.08
-0.1357	0.0102	0.0279	169.21	-18.81	21.36
-0.1357	0.0102	0.0305	166.91	-17.78	28.75
-0.1357	0.0102	0.033	164.85	-15.46	35.11
-0.1357	0.0102	0.0356	161.57	-15.18	44.79
-0.1357	0.0102	0.0381	158.51	-13.22	51.29
-0.1357	0.0102	0.0407	156.64	-29.69	57.19
-0.1357	0.0102	0.0432	156.53	-28.47	56.80
-0.1357	0.0102	0.0457	156.78	-27.49	57.24
-0.1357	0.0102	0.0508	156.46	-23.24	56.83
-0.1357	0.0076	0.0254	170.58	-10.42	10.36
-0.1357	0.0076	0.0279	169.09	-12.02	18.34
-0.1357	0.0076	0.0305	167.49	-12.64	25.19
-0.1357	0.0076	0.033	165.95	-11.52	31.30
-0.1357	0.0076	0.0356	164.08	-10.82	36.73
-0.1357	0.0076	0.0381	159.37	-8.50	48.16
-0.1357	0.0076	0.0407	156.91	-31.03	56.02
-0.1357	0.0076	0.0432	156.82	-27.03	56.18
-0.1357	0.0076	0.0457	156.89	-24.88	56.22
-0.1357	0.0076	0.0483	156.73	-21.36	56.43
-0.1357	0.0076	0.0508	156.64	-20.24	56.13
-0.1357	0.0051	0.0076	109.74	-4.06	-15.36
-0.1357	0.0051	0.0102	109.46	-9.52	-12.78
-0.1357	0.0051	0.0127	146.62	-33.11	4.18

x (m)	y (m)	z (m)	u (m/s)	v (m/s)	w (m/s)
-0.1357	0.0051	0.0152	112.68	-14.94	-1.96
-0.1357	0.0051	0.0178	114.84	-4.57	3.04
-0.1357	0.0051	0.0203	173.00	-1.43	-9.44
-0.1357	0.0051	0.0229	171.81	-4.34	0.29
-0.1357	0.0051	0.0254	170.31	-5.33	9.07
-0.1357	0.0051	0.0279	168.85	-6.83	16.41
-0.1357	0.0051	0.0305	167.28	-7.40	23.07
-0.1357	0.0051	0.033	165.74	-6.02	28.96
-0.1357	0.0051	0.0356	164.37	-5.97	33.98
-0.1357	0.0051	0.0381	160.65	-3.40	42.66
-0.1357	0.0051	0.0407	157.26	-26.34	54.89
-0.1357	0.0051	0.0432	156.11	-25.97	55.07
-0.1357	0.0051	0.0457	156.86	-24.85	55.54
-0.1357	0.0051	0.0483	156.13	-23.29	55.59
-0.1357	0.0051	0.0508	156.31	-21.36	55.60
-0.1357	0.0025	0.0076	119.05	52.27	-33.48
-0.1357	0.0025	0.0102	176.95	-33.16	-43.47
-0.1357	0.0025	0.0127	175.83	-32.26	-35.45
-0.1357	0.0025	0.0152	174.82	-7.26	-25.71
-0.1357	0.0025	0.0178	173.73	-2.53	-16.27
-0.1357	0.0025	0.0203	172.45	-0.03	-7.07
-0.1357	0.0025	0.0229	171.31	1.29	1.45
-0.1357	0.0025	0.0254	169.91	4.52	9.03
-0.1357	0.0025	0.0279	168.41	6.58	16.06
-0.1357	0.0025	0.0305	166.68	6.23	22.21
-0.1357	0.0025	0.033	165.28	7.75	28.12

x (m)	y (m)	z (m)	u (m/s)	v (m/s)	w (m/s)
-0.1357	0.0025	0.0356	164.07	7.48	32.97
-0.1357	0.0025	0.0381	161.27	9.05	40.39
-0.1357	0.0025	0.0407	157.44	-34.57	52.96
-0.1357	0.0025	0.0432	156.24	-29.97	53.89
-0.1357	0.0025	0.0457	155.53	-22.86	54.27
-0.1357	0.0025	0.0483	155.34	-19.51	54.50
-0.1357	0.0025	0.0508	153.78	-21.40	54.32
-0.1357	0	0.0076	138.88	-21.78	-20.43
-0.1357	0	0.0102	150.80	-21.48	-48.16
-0.1357	0	0.0127	150.39	-21.20	-39.13
-0.1357	0	0.0152	148.48	-21.14	-31.29
-0.1357	0	0.0178	173.03	-36.22	-12.91
-0.1357	0	0.0203	172.18	-24.65	-5.50
-0.1357	0	0.0229	170.68	0.58	2.72
-0.1357	0	0.0254	169.45	4.87	9.47
-0.1357	0	0.0279	168.04	7.30	15.92
-0.1357	0	0.0305	166.63	-1.94	22.13
-0.1357	0	0.033	165.27	-1.12	27.18
-0.1357	0	0.0356	163.13	-4.51	33.62
-0.1357	0	0.0381	159.36	-16.06	40.87
-0.1357	0	0.0407	158.14	-41.54	49.13
-0.1357	0	0.0432	155.03	-32.55	51.19
-0.1357	0	0.0457	154.11	-23.27	52.22
-0.1357	0	0.0483	153.46	-20.37	53.00
-0.1357	0	0.0508	153.36	-24.14	53.66

Table A-2: Experimental Data for 20° Angle of Attack, 80% Chord.

x (m)	y (m)	z (m)	u (m/s)	v (m/s)	w (m/s)
0	0.0711	0.0051	139.68	18.47	50.44
0	0.0711	0.0102	139.34	18.28	55.35
0	0.0711	0.0152	140.74	16.04	59.41
0	0.0711	0.0203	144.34	9.47	63.23
0	0.0711	0.0254	151.37	-3.77	67.42
0	0.0711	0.0305	151.90	-7.54	69.27
0	0.0711	0.0356	154.99	-17.43	75.01
0	0.0711	0.0407	158.40	-25.42	72.23
0	0.0711	0.0457	157.48	-29.04	77.22
0	0.0711	0.0508	154.98	-21.65	69.35
0	0.0711	0.0559	158.70	-33.14	73.72
0	0.0711	0.061	159.21	-32.35	71.23
0	0.0711	0.0661	155.45	-13.40	66.39
0	0.0711	0.0762	160.76	-19.55	64.40
0	0.0711	0.0813	160.26	-18.36	61.25
0	0.0711	0.0864	160.23	-16.33	60.08
0	0.0711	0.0915	159.92	-15.54	59.16
0	0.0711	0.0965	159.77	-14.13	58.40
0	0.0711	0.1016	160.59	-14.59	58.22
0	0.0661	0.0152	141.82	13.69	49.16
0	0.0661	0.0203	142.20	10.06	57.34
0	0.0661	0.0254	145.86	4.99	62.30

x (m)	y (m)	z (m)	u (m/s)	v (m/s)	w (m/s)
0	0.0661	0.0305	155.87	-20.17	67.82
0	0.0661	0.0356	156.95	-21.10	70.44
0	0.0661	0.0407	161.83	-33.05	72.15
0	0.0661	0.0457	158.90	-34.43	79.55
0	0.0661	0.0508	156.44	-25.83	70.99
0	0.0661	0.0559	159.79	-37.81	74.02
0	0.0661	0.061	160.08	-36.60	71.14
0	0.0661	0.0661	156.08	-16.29	66.71
0	0.0661	0.0711	159.23	-23.85	65.76
0	0.0661	0.0762	161.28	-22.11	63.53
0	0.0661	0.0813	160.86	-19.73	60.29
0	0.0661	0.0864	162.02	-21.19	59.33
0	0.0661	0.0915	160.48	-16.53	57.85
0	0.0661	0.0965	161.85	-18.51	57.71
0	0.0661	0.1016	161.03	-15.49	57.17
0	0.061	0.0254	142.18	9.23	53.53
0	0.061	0.0305	145.64	2.04	60.87
0	0.061	0.0356	158.45	-24.95	69.02
0	0.061	0.0407	162.09	-36.05	70.08
0	0.061	0.0457	162.04	-44.66	79.55
0	0.061	0.0508	157.60	-29.43	71.94
0	0.061	0.0559	160.86	-42.01	74.09
0	0.061	0.061	161.17	-39.97	70.97
0	0.061	0.0661	156.52	-18.52	66.91
0	0.061	0.0711	159.75	-25.89	65.20
0	0.061	0.0762	161.85	-23.79	62.40

x (m)	y (m)	z (m)	u (m/s)	v (m/s)	w (m/s)
0	0.061	0.0813	161.67	-21.19	58.75
0	0.061	0.0864	162.35	-23.58	57.84
0	0.061	0.0915	160.91	-17.68	56.57
0	0.061	0.0965	162.66	-19.86	56.65
0	0.061	0.1016	161.20	-15.37	55.86
0	0.0559	0.0356	146.32	-3.02	60.38
0	0.0559	0.0407	168.11	-49.89	70.08
0	0.0559	0.0457	164.30	-50.83	77.56
0	0.0559	0.0508	157.16	-28.09	68.71
0	0.0559	0.0559	163.18	-47.49	73.24
0	0.0559	0.061	162.35	-44.63	70.62
0	0.0559	0.0661	157.34	-22.30	67.12
0	0.0559	0.0711	161.03	-29.80	64.47
0	0.0559	0.0762	162.68	-25.35	60.93
0	0.0559	0.0813	162.79	-22.82	56.97
0	0.0559	0.0864	163.04	-22.12	56.09
0	0.0559	0.0915	161.45	-17.89	55.12
0	0.0559	0.1016	161.88	-15.92	54.68
0	0.0508	0.0407	171.23	-59.15	65.25
0	0.0508	0.0457	168.89	-59.93	68.61
0	0.0508	0.0508	161.30	-38.48	67.39
0	0.0508	0.0559	165.34	-53.95	70.95
0	0.0508	0.061	164.16	-49.02	68.53
0	0.0508	0.0661	158.53	-26.47	66.33
0	0.0508	0.0711	161.24	-29.92	62.99
0	0.0508	0.0762	163.12	-25.61	59.58

x (m)	y (m)	z (m)	u (m/s)	v (m/s)	w (m/s)
0	0.0508	0.0813	163.65	-23.39	55.64
0	0.0508	0.0864	163.65	-21.63	54.02
0	0.0508	0.0915	161.88	-17.10	53.32
0	0.0508	0.0965	162.79	-17.02	53.62
0	0.0508	0.1016	162.10	-14.64	53.45
0	0.0457	0.0457	168.89	-69.85	70.90
0	0.0457	0.0508	160.14	-42.69	64.41
0	0.0457	0.0559	166.56	-58.79	67.00
0	0.0457	0.061	165.39	-51.62	63.45
0	0.0457	0.0661	160.83	-33.38	64.33
0	0.0457	0.0711	163.05	-32.08	60.77
0	0.0457	0.0762	163.67	-25.05	57.14
0	0.0457	0.0813	164.61	-22.37	53.58
0	0.0457	0.0864	164.13	-18.96	51.84
0	0.0457	0.0915	162.52	-14.71	51.72
0	0.0457	0.0965	162.93	-14.88	52.05
0	0.0457	0.1016	162.69	-13.12	52.46
0	0.0407	0.0457	171.48	-77.45	66.14
0	0.0407	0.0559	166.38	-60.13	63.20
0	0.0407	0.061	165.74	-52.61	55.26
0	0.0407	0.0661	160.30	-31.01	58.18
0	0.0407	0.0711	163.55	-33.70	58.89
0	0.0407	0.0762	164.30	-25.18	54.87
0	0.0407	0.0813	165.46	-22.54	50.06
0	0.0407	0.0864	164.91	-20.53	49.97
0	0.0407	0.0915	163.28	-14.74	50.15

x (m)	y (m)	z (m)	u (m/s)	v (m/s)	w (m/s)
0	0.0407	0.0965	163.78	-14.22	50.69
0	0.0407	0.1016	162.10	-12.57	55.03
0	0.0356	0.0559	165.58	-58.64	50.92
0	0.0356	0.061	165.25	-51.25	48.56
0	0.0356	0.0661	161.97	-32.18	52.81
0	0.0356	0.0711	163.90	-32.42	54.99
0	0.0356	0.0762	164.32	-23.28	51.92
0	0.0356	0.0813	164.69	-19.32	47.58
0	0.0356	0.0864	165.33	-21.45	48.16
0	0.0356	0.0915	163.07	-13.46	48.30
0	0.0356	0.0965	163.61	-13.60	49.36
0	0.0356	0.1016	162.10	-11.45	53.15
0	0.0305	0.0559	166.61	-55.23	38.04
0	0.0305	0.061	165.61	-47.63	41.15
0	0.0305	0.0661	165.88	-34.33	46.80
0	0.0305	0.0711	164.85	-29.14	48.43
0	0.0305	0.0762	164.59	-20.43	48.88
0	0.0305	0.0864	165.77	-18.04	46.52
0	0.0305	0.0915	163.10	-11.78	47.01
0	0.0305	0.0965	163.24	-11.35	47.92
0	0.0305	0.1016	161.66	-10.42	52.76
0	0.0254	0.0559	166.85	-48.65	30.86
0	0.0254	0.061	166.25	-42.74	35.26
0	0.0254	0.0661	166.28	-27.94	41.48
0	0.0254	0.0711	165.43	-23.59	43.11
0	0.0254	0.0762	165.09	-16.80	44.97

x (m)	y (m)	z (m)	u (m/s)	v (m/s)	w (m/s)
0	0.0254	0.0813	165.07	-13.70	42.91
0	0.0254	0.0864	165.11	-13.55	44.47
0	0.0254	0.0915	163.37	-9.98	45.54
0	0.0254	0.0965	155.27	-9.44	69.35
0	0.0254	0.1016	162.30	-9.37	50.52
0	0.0203	0.0559	167.35	-42.03	26.61
0	0.0203	0.061	166.52	-36.87	31.41
0	0.0203	0.0661	166.46	-21.32	36.99
0	0.0203	0.0711	165.51	-16.68	37.87
0	0.0203	0.0762	164.51	-12.02	43.80
0	0.0203	0.0813	165.39	-13.45	41.45
0	0.0203	0.0864	164.93	-10.07	43.33
0	0.0203	0.0915	163.59	-8.78	44.43
0	0.0203	0.0965	163.55	-6.77	45.54
0	0.0203	0.1016	161.99	-6.73	50.64
0	0.0152	0.0457	168.53	-32.05	11.85
0	0.0152	0.0559	167.78	-34.98	24.20
0	0.0152	0.061	167.01	-31.00	28.67
0	0.0152	0.0661	166.81	-14.58	33.34
0	0.0152	0.0711	165.55	-17.59	35.92
0	0.0152	0.0762	164.52	-7.99	40.91
0	0.0152	0.0864	164.43	-7.65	41.92
0	0.0152	0.0915	163.87	-7.45	43.33
0	0.0152	0.0965	163.58	-7.27	44.82
0	0.0152	0.1016	163.29	-4.63	46.32
0	0.0102	0.0457	168.39	-29.46	11.30

x (m)	y (m)	z (m)	u (m/s)	v (m/s)	w (m/s)
0	0.0102	0.0559	167.75	-27.29	23.35
0	0.0102	0.061	167.05	-24.00	27.05
0	0.0102	0.0661	166.89	-7.83	31.37
0	0.0102	0.0711	165.87	-6.60	34.73
0	0.0102	0.0762	164.91	-4.76	37.99
0	0.0102	0.0864	164.46	-0.79	41.10
0	0.0102	0.0915	164.11	-4.71	42.68
0	0.0102	0.0965	163.48	-5.82	44.33
0	0.0102	0.1016	163.12	-6.17	45.86
0	0.0051	0.0457	168.80	-21.05	11.10
0	0.0051	0.0559	167.75	-20.39	22.20
0	0.0051	0.061	167.09	-18.15	26.54
0	0.0051	0.0661	167.07	-1.18	30.31
0	0.0051	0.0711	165.80	-0.98	34.74
0	0.0051	0.0762	164.62	5.44	36.50
0	0.0051	0.0813	164.52	-0.37	38.39
0	0.0051	0.0864	164.88	-2.33	40.64
0	0.0051	0.0915	164.18	-2.04	42.45
0	0.0051	0.0965	163.75	-1.33	44.22
0	0.0051	0.1016	162.86	-2.36	45.96
0	0	0.0407	168.66	-12.39	7.14
0	0	0.0457	168.45	-13.48	12.73
0	0	0.0559	167.86	-13.27	22.10
0	0	0.061	167.21	-12.23	26.15
0	0	0.0661	167.03	5.01	30.41
0	0	0.0711	165.95	4.54	34.53

x (m)	y (m)	z (m)	u (m/s)	v (m/s)	w (m/s)
0	0	0.0762	165.15	3.83	35.84
0	0	0.0813	164.56	2.22	38.27
0	0	0.0864	164.73	-0.99	40.67
0	0	0.0915	163.96	0.06	42.72
0	0	0.0965	163.51	-1.21	44.32
0	0	0.1016	163.05	-1.94	45.57

Table A-3: Experimental Data for 30° Angle of Attack, 40% Chord.

x (m)	y (m)	z (m)	u (m/s)	v (m/s)	w (m/s)
-0.1357	0.0407	0.0051	116.04	39.87	63.53
-0.1357	0.0407	0.0076	117.59	30.07	68.27
-0.1357	0.0407	0.0102	118.22	28.28	72.39
-0.1357	0.0407	0.0127	113.2	40.84	74.99
-0.1357	0.0407	0.0152	115.41	34.09	79.99
-0.1357	0.0407	0.0178	116.81	30.1	83.86
-0.1357	0.0407	0.0203	119.86	24.27	86.86
-0.1357	0.0407	0.0229	119.71	21.25	92.41
-0.1357	0.0407	0.0254	121.38	11.13	92.38
-0.1357	0.0407	0.0279	122.58	6.37	93.71
-0.1357	0.0407	0.0305	128	-4.41	96.57
-0.1357	0.0407	0.033	129.2	11.56	96.49
-0.1357	0.0407	0.0356	130.05	-14.11	98.86
-0.1357	0.0407	0.0381	131.91	-18.09	99.07
-0.1357	0.0407	0.0407	132.69	-20.61	100
-0.1357	0.0407	0.0432	133.57	-20.57	99.74
-0.1357	0.0407	0.0457	134.46	-23.58	99.89
-0.1357	0.0407	0.0483	135.55	-29.82	100.51
-0.1357	0.0407	0.0508	135.9	-27.15	100.04
-0.1357	0.0381	0.0051	115.42	20.27	62.25
-0.1357	0.0381	0.0076	106.32	48.2	62.26
-0.1357	0.0381	0.0102	108.98	40.48	72.94
-0.1357	0.0381	0.0127	113.12	27.31	81.64

x (m)	y (m)	z (m)	u (m/s)	v (m/s)	w (m/s)
-0.1357	0.0381	0.0152	117.3	24.8	85.34
-0.1357	0.0381	0.0178	117.93	20.8	89
-0.1357	0.0381	0.0203	120.56	19.54	90.19
-0.1357	0.0381	0.0229	120.32	16.81	94.06
-0.1357	0.0381	0.0254	122.05	8.74	94.73
-0.1357	0.0381	0.0279	126.7	-6.65	98.16
-0.1357	0.0381	0.0305	128.23	-4.89	99.31
-0.1357	0.0381	0.033	129.72	-11.12	99.72
-0.1357	0.0381	0.0356	131.65	-13.4	100.2
-0.1357	0.0381	0.0381	131.95	-7.44	100.07
-0.1357	0.0381	0.0407	132.46	-15.39	100.25
-0.1357	0.0381	0.0432	133.24	-17.91	100.1
-0.1357	0.0381	0.0457	134.41	-22.19	100.12
-0.1357	0.0381	0.0483	134.9	-26.98	100.38
-0.1357	0.0381	0.0508	134.73	-24.57	98.48
-0.1357	0.0356	0.0051	99.37	45.48	46.53
-0.1357	0.0356	0.0076	108.62	25.07	62.82
-0.1357	0.0356	0.0102	119.69	15.71	73.5
-0.1357	0.0356	0.0127	121.19	10.9	77.15
-0.1357	0.0356	0.0152	126.7	-11.4	82.69
-0.1357	0.0356	0.0178	124.31	-1.26	81.57
-0.1357	0.0356	0.0203	126.03	-8.3	87.48
-0.1357	0.0356	0.0229	127.28	-5.2	90.14
-0.1357	0.0356	0.0254	127.48	10.18	92.17
-0.1357	0.0356	0.0279	126.61	4.54	95.8
-0.1357	0.0356	0.0305	124.96	-0.79	98.69

x (m)	y (m)	z (m)	u (m/s)	v (m/s)	w (m/s)
-0.1357	0.0356	0.033	126.31	-5.33	100.1
-0.1357	0.0356	0.0356	130.37	-12.12	101.54
-0.1357	0.0356	0.0381	131.45	-17.48	101.5
-0.1357	0.0356	0.0407	132.64	-19.74	101.52
-0.1357	0.0356	0.0432	133.77	-22.83	100.54
-0.1357	0.0356	0.0457	135.57	-28.1	100.54
-0.1357	0.0356	0.0483	136.17	-29.06	100.39
-0.1357	0.0356	0.0508	136.36	-26.2	99.5
-0.1357	0.033	0.0076	124.63	19.5	70.66
-0.1357	0.033	0.0102	124.25	17.26	73.5
-0.1357	0.033	0.0127	124.4	20.46	76.2
-0.1357	0.033	0.0152	124.49	20.77	78.8
-0.1357	0.033	0.0178	124.81	15.35	81.75
-0.1357	0.033	0.0203	121.05	-16.49	91.19
-0.1357	0.033	0.0229	125.09	-22.74	86.07
-0.1357	0.033	0.0254	125.72	-19.8	88.11
-0.1357	0.033	0.0279	124.34	-15.22	93.8
-0.1357	0.033	0.0305	125.26	-7.2	94.8
-0.1357	0.033	0.033	126.86	-3.46	97.29
-0.1357	0.033	0.0356	130.73	-19.18	102.03
-0.1357	0.033	0.0381	130.43	-19.28	102.76
-0.1357	0.033	0.0407	131.65	-3.62	102.9
-0.1357	0.033	0.0432	132.73	-22.94	101.44
-0.1357	0.033	0.0457	133.39	-24.29	101.91
-0.1357	0.033	0.0483	134.83	-26.92	101.31
-0.1357	0.033	0.0508	135.82	-14.39	100.65

x (m)	y (m)	z (m)	u (m/s)	v (m/s)	w (m/s)
-0.1357	0.0305	0.0102	121.88	-9.07	70.42
-0.1357	0.0305	0.0127	122.86	11.89	73
-0.1357	0.0305	0.0152	123.88	6.5	75.75
-0.1357	0.0305	0.0178	125.11	6.75	78.81
-0.1357	0.0305	0.0203	125.76	2.9	81.27
-0.1357	0.0305	0.0229	126.26	-1.02	83.88
-0.1357	0.0305	0.0254	126.67	-21.72	85.79
-0.1357	0.0305	0.0279	126.99	-31.32	88.13
-0.1357	0.0305	0.0305	127.5	-25.13	89.9
-0.1357	0.0305	0.033	126.93	-17.4	94.06
-0.1357	0.0305	0.0356	128.17	-11.16	95.91
-0.1357	0.0305	0.0381	129.8	-16.16	97.94
-0.1357	0.0305	0.0407	131.15	-23.2	100.7
-0.1357	0.0305	0.0432	130.91	-23.56	100.85
-0.1357	0.0305	0.0457	131.88	-22.36	100.77
-0.1357	0.0305	0.0483	132.83	-24.66	99.69
-0.1357	0.0305	0.0508	133.52	-24.77	98.7
-0.1357	0.0279	0.0229	125.32	5.13	80.25
-0.1357	0.0279	0.0254	126.26	0.8	82.7
-0.1357	0.0279	0.0279	127.41	-14.44	85.4
-0.1357	0.0279	0.0305	127.6	-32.25	87.6
-0.1357	0.0279	0.033	128.01	-26.25	90.14
-0.1357	0.0279	0.0356	132.8	-29.11	94.46
-0.1357	0.0279	0.0381	129.3	-19.65	94.91
-0.1357	0.0279	0.0407	134.99	-28.25	99.58
-0.1357	0.0279	0.0432	135.41	-34.31	102.41

x (m)	y (m)	z (m)	u (m/s)	v (m/s)	w (m/s)
-0.1357	0.0279	0.0457	135.06	-33.83	103.65
-0.1357	0.0279	0.0483	135.8	-33.73	103.45
-0.1357	0.0279	0.0508	136.67	-18.87	101.66
-0.1357	0.0254	0.0279	117.9	3.36	73.62
-0.1357	0.0254	0.0305	114.38	-0.65	76.97
-0.1357	0.0254	0.033	123.88	-31.24	84.41
-0.1357	0.0254	0.0356	126.93	-30.24	88.38
-0.1357	0.0254	0.0381	129.78	-21.11	92.22
-0.1357	0.0254	0.0407	139.09	-40.87	99.73
-0.1357	0.0254	0.0432	137.33	-34.22	99.8
-0.1357	0.0254	0.0457	137.47	-36.37	102.16
-0.1357	0.0254	0.0483	137.83	-38.49	102.72
-0.1357	0.0254	0.0508	137.58	-38.73	101.98
-0.1357	0.0229	0.0381	146.85	-67.73	109.62
-0.1357	0.0229	0.0407	150.96	-58.47	100.16
-0.1357	0.0229	0.0432	136.13	-41.37	96.49
-0.1357	0.0229	0.0457	136.23	-37.55	98.04
-0.1357	0.0229	0.0483	137.15	-43.28	99.88
-0.1357	0.0229	0.0508	138.43	-46.08	99.61
-0.1357	0.0203	0.0356	125.08	-33.24	91.83
-0.1357	0.0203	0.0381	146.39	-77.52	111.96
-0.1357	0.0203	0.0407	148.4	-73.98	107.04
-0.1357	0.0203	0.0432	149.99	-59.3	100.26
-0.1357	0.0203	0.0457	146.1	-51.65	104.15
-0.1357	0.0203	0.0483	144.32	-44.29	100.44
-0.1357	0.0203	0.0508	137.76	-24.68	101.3

x (m)	y (m)	z (m)	u (m/s)	v (m/s)	w (m/s)
-0.1357	0.0178	0.0381	128.66	-46.27	95.66
-0.1357	0.0178	0.0407	148.73	-80.15	106.63
-0.1357	0.0178	0.0432	149.66	-73.27	101.46
-0.1357	0.0178	0.0457	147.2	-53.9	95.04
-0.1357	0.0178	0.0483	146.27	-41.22	92.2
-0.1357	0.0178	0.0508	147	-39.14	87.26
-0.1357	0.0152	0.0407	145.45	-64.45	87.07
-0.1357	0.0152	0.0432	154.21	-65.02	81.02
-0.1357	0.0152	0.0457	155.01	-56.19	73.87
-0.1357	0.0152	0.0483	156.47	-45.4	67.39
-0.1357	0.0152	0.0508	153.5	-37.85	72.45
-0.1357	0.0127	0.0407	140.72	-32.91	52.09
-0.1357	0.0127	0.0432	158.32	-55.65	61.34
-0.1357	0.0127	0.0457	157.23	-49.3	62.95
-0.1357	0.0127	0.0483	157.43	-45.54	60.31
-0.1357	0.0127	0.0508	155.87	-35.82	63.83
-0.1357	0.0102	0.0407	140.24	-26.26	37.77
-0.1357	0.0102	0.0432	158.64	-50.68	52.3
-0.1357	0.0102	0.0457	158.37	-43.31	54.41
-0.1357	0.0102	0.0483	158.3	-49.83	55.88
-0.1357	0.0102	0.0508	156.89	-37.41	58.41
-0.1357	0.0076	0.0432	160.7	-57.15	43.02
-0.1357	0.0076	0.0457	160.06	-44.33	47.43
-0.1357	0.0076	0.0483	159.12	-44.15	50.92
-0.1357	0.0076	0.0508	157.65	-36.04	54.4
-0.1357	0.0051	0.0432	163.04	-49.54	36.03

x (m)	y (m)	z (m)	u (m/s)	v (m/s)	w (m/s)
-0.1357	0.0051	0.0457	161.87	-44.5	41.46
-0.1357	0.0051	0.0483	159.93	-45.04	46.84
-0.1357	0.0051	0.0508	158.39	-39.03	51.18
-0.1357	0.0025	0.0432	164.69	-48.63	30.68
-0.1357	0.0025	0.0457	162.55	-41.92	38.21
-0.1357	0.0025	0.0483	160.65	-40.22	44.37
-0.1357	0.0025	0.0508	159.07	-33.67	49.16
-0.1357	0	0.0407	166.98	-48.23	21.28
-0.1357	0	0.0432	164.67	-41.81	29.72
-0.1357	0	0.0457	162.91	-38.05	37.27
-0.1357	0	0.0483	161.12	-37.29	43.24
-0.1357	0	0.0508	159.7	-26.76	47.87

Table A-4: Experimental Data for 30° Angle of Attack, 80% Chord.

x (m)	y (m)	z (m)	u (m/s)	v (m/s)	w (m/s)
0	0.0711	0.0051	80.79	92.56	36.09
0	0.0711	0.0102	67.07	132.87	36.15
0	0.0711	0.0152	87.22	92.14	53.44
0	0.0711	0.0203	113.63	29.9	72.35
0	0.0711	0.0254	110.57	24.03	85.26
0	0.0711	0.0305	143.24	-27.83	114.45
0	0.0711	0.0356	128.33	-3.24	116.05
0	0.0711	0.0407	122.43	32.34	90.19
0	0.0711	0.0457	124.04	16.76	93.64
0	0.0711	0.0508	129.1	2.66	98.33
0	0.0711	0.0559	130.4	-4.17	100.11
0	0.0711	0.061	130.55	-3.89	102.02
0	0.0711	0.0661	132.6	-10.48	103.57
0	0.0711	0.0711	133.57	-13.2	102.77
0	0.0711	0.0762	133.94	-19.26	102.45
0	0.0711	0.0813	134.14	-13.73	101.02
0	0.0711	0.0864	136.27	-20.62	100.14
0	0.0711	0.0915	137.24	-19.27	100.03
0	0.0711	0.0965	138.51	-25.87	99.55
0	0.0711	0.1016	139.51	-27.54	98.78
0	0.0661	0.0305	121.09	5.29	66.99
0	0.0661	0.0356	120.45	3.45	74.67
0	0.0661	0.0407	121.48	-3.57	82.8

x (m)	y (m)	z (m)	u (m/s)	v (m/s)	w (m/s)
0	0.0661	0.0457	124.55	-6.72	87.9
0	0.0661	0.0508	126.31	-2.35	91.59
0	0.0661	0.0559	137.52	-38.68	98.9
0	0.0661	0.0661	135.41	-37.76	100.18
0	0.0661	0.0711	136.34	-35.34	100.56
0	0.0661	0.0762	137.09	-37.07	100.76
0	0.0661	0.0813	141.96	-43.5	93.91
0	0.0661	0.0864	139.09	-48.14	101.7
0	0.0661	0.0915	139.65	-47.05	102.22
0	0.0661	0.0965	142.42	-53.02	101.94
0	0.0661	0.1016	130.11	-24.69	92.84
0	0.061	0.0457	123.45	16.63	78.97
0	0.061	0.0508	125.08	13.95	85.59
0	0.061	0.0559	127.56	7.67	89.69
0	0.061	0.061	128.96	2.84	92.58
0	0.061	0.0661	129.3	-1.45	94.71
0	0.061	0.0711	130.05	-4.23	96.2
0	0.061	0.0762	130.96	-7.13	96.96
0	0.061	0.0813	137.13	-39.71	100.33
0	0.061	0.0864	137.14	-45.09	100.27
0	0.061	0.0915	137.66	-43.53	100.48
0	0.061	0.0965	138.86	-45.76	99.61
0	0.061	0.1016	141.1	-46.17	99.17
0	0.0559	0.0559	132.19	-11.44	84.8
0	0.0559	0.061	134.2	-14.08	90.45
0	0.0559	0.0661	137.37	-19.49	95.41

x (m)	y (m)	z (m)	u (m/s)	v (m/s)	w (m/s)
0	0.0559	0.0711	142.64	-36.71	100.9
0	0.0559	0.0762	141.85	-33.89	101.66
0	0.0559	0.0813	136.41	-22.43	99.37
0	0.0559	0.0864	138.64	-26.97	100.89
0	0.0559	0.0915	138.51	-29.23	100.78
0	0.0559	0.0965	139.63	-30.4	100.12
0	0.0559	0.1016	140.64	-31.4	98.58
0	0.0508	0.061	157.12	-74.34	94.46
0	0.0508	0.0661	126.95	-0.33	83.38
0	0.0508	0.0711	128.97	-4.15	88.4
0	0.0508	0.0762	131.45	-14.88	92.57
0	0.0508	0.0813	132.37	-18.19	95.24
0	0.0508	0.0864	133.96	-17.55	95.13
0	0.0508	0.0915	134.4	-22.07	97.28
0	0.0508	0.0965	133.66	-18.1	95.72
0	0.0508	0.1016	135.43	-21.33	93.71
0	0.0457	0.0661	145.14	-73.89	114.39
0	0.0457	0.0711	155.66	-62.16	96.03
0	0.0457	0.0762	129.82	-8.53	86.54
0	0.0457	0.0813	131.47	-14.83	91.63
0	0.0457	0.0864	136.92	-26.57	94.63
0	0.0457	0.0915	136.48	-27.56	97.25
0	0.0457	0.1016	141.13	-34.12	95.21
0	0.0407	0.0661	146.3	-93.39	113.16
0	0.0407	0.0711	145.63	-84.42	112.69
0	0.0407	0.0762	145.29	-71.1	112.48

x (m)	y (m)	z (m)	u (m/s)	v (m/s)	w (m/s)
0	0.0407	0.0813	145.47	-63.82	111.55
0	0.0407	0.0864	138.69	-34.45	93.53
0	0.0407	0.0915	136.99	-31.77	94.69
0	0.0407	0.0965	139.76	-34.67	95.07
0	0.0407	0.1016	142.61	-47.02	94.75
0	0.0356	0.0711	146.49	-92.58	111.32
0	0.0356	0.0762	145.96	-86.61	110.92
0	0.0356	0.0813	140.22	-57.04	107.27
0	0.0356	0.0864	145.46	-47.92	92.35
0	0.0356	0.0915	139.63	-33.32	90.49
0	0.0356	0.0965	136.89	-27.19	90.55
0	0.0356	0.1016	139.41	-29.65	90.95
0	0.0305	0.0762	141.66	-66.29	92.16
0	0.0305	0.0813	147.62	-40.54	76.77
0	0.0305	0.0864	146.91	-38.17	78.47
0	0.0305	0.0915	147.17	-36.91	78.87
0	0.0305	0.0965	146.13	-37.64	82.23
0	0.0305	0.1016	143.67	-32.58	84.54
0	0.0254	0.0762	149.83	-53.54	63.46
0	0.0254	0.0813	150.9	-41.9	62.93
0	0.0254	0.0864	147.5	-28.75	66.11
0	0.0254	0.0915	150.1	-32.41	67.45
0	0.0254	0.0965	149.86	-34.68	70.8
0	0.0254	0.1016	149.78	-30.78	71.27
0	0.0203	0.0813	148.66	-33.18	55.3
0	0.0203	0.0864	152.33	-35.68	55.84

x (m)	y (m)	z (m)	u (m/s)	v (m/s)	w (m/s)
0	0.0203	0.0915	154.95	-32.75	55.54
0	0.0203	0.0965	156.98	-33.57	54.33
0	0.0203	0.1016	158.75	-30.16	52.72
0	0.0152	0.0762	139.45	-51.99	68.54
0	0.0152	0.0813	143.71	-43.52	64.64
0	0.0152	0.0864	148.28	-39.4	60.82
0	0.0152	0.0915	151.48	-30.19	59.39
0	0.0152	0.0965	153.67	-31.34	57.55
0	0.0152	0.1016	155.39	-28.66	56.34
0	0.0102	0.0711	123.48	-56.38	87.3
0	0.0102	0.0762	131.84	-45.4	79.67
0	0.0102	0.0813	137.16	-42.56	74.35
0	0.0102	0.0864	142.59	-38.85	69.42
0	0.0102	0.0915	147.44	-27.88	65.01
0	0.0102	0.0965	151.3	-30.66	60.54
0	0.0102	0.1016	153.67	-31.98	58.43
0	0.0051	0.0661	111.22	-49.41	102
0	0.0051	0.0711	119.59	-40.62	93.85
0	0.0051	0.0762	127.27	-41.48	86.37
0	0.0051	0.0813	133.1	-43.14	80.95
0	0.0051	0.0864	139.56	-37.9	74.42
0	0.0051	0.0915	144.47	-29.95	68.7
0	0.0051	0.0965	149.02	-21.52	63.36
0	0.0051	0.1016	152.34	-25.76	60.27
0	0	0.0457	81.98	-35.16	130.4
0	0	0.0508	88.3	-36.76	124.87

x (m)	y (m)	z (m)	u (m/s)	v (m/s)	w (m/s)
0	0	0.0559	95.11	-35.87	118.73
0	0	0.061	102.13	-34.74	111.45
0	0	0.0661	109.88	-33.25	104.38
0	0	0.0711	117.59	-36.07	97.21
0	0	0.0762	124.94	-40.09	90.31
0	0	0.0813	132.08	-31.22	82.49
0	0	0.0864	138.49	-23.71	76.48
0	0	0.0915	143.62	-19.28	71.26
0	0	0.0965	148.52	-16.18	66.04
0	0	0.1016	152.08	-14.71	62.3

Table A-5: Experimental Data for 35° Angle of Attack, 40% Chord.

x (m)	y (m)	z (m)	u (m/s)	v (m/s)	w (m/s)
-0.1357	0.0661	0.0051	112.15	5.15	77.06
-0.1357	0.0661	0.0076	112.6	4.22	78.2
-0.1357	0.0661	0.0102	112.74	3.16	79.18
-0.1357	0.0661	0.0127	113.38	4.54	80.41
-0.1357	0.0661	0.0152	114.38	3.08	81.99
-0.1357	0.0661	0.0178	115.49	-3.91	83.64
-0.1357	0.0661	0.0203	115.99	-3.97	84.79
-0.1357	0.0661	0.0229	116.75	-8.87	86.2
-0.1357	0.0661	0.0254	117.38	-10.09	87.5
-0.1357	0.0661	0.0279	118.19	-13.93	88.57
-0.1357	0.0661	0.0305	118.19	-9.92	89.55
-0.1357	0.0661	0.033	119.22	-12.8	90.58
-0.1357	0.0661	0.0356	119.83	-9.8	91.87
-0.1357	0.0661	0.0381	120.1	-16.29	92.56
-0.1357	0.0661	0.0407	120.36	-19.93	93.36
-0.1357	0.0661	0.0432	120.75	-19.39	94.53
-0.1357	0.0661	0.0457	121.14	-20.24	95.51
-0.1357	0.0661	0.0483	121.6	-20.44	96.42
-0.1357	0.0661	0.0508	122.05	-21.38	97.42
-0.1357	0.0661	0.0534	94.51	30.71	85.24
-0.1357	0.0661	0.0559	95.2	27.94	84.5
-0.1357	0.0661	0.0584	93.44	32.91	84.23
-0.1357	0.0661	0.061	93.17	30.93	84.29

x (m)	y (m)	z (m)	u (m/s)	v (m/s)	w (m/s)
-0.1357	0.0661	0.0635	96.62	26.68	86.51
-0.1357	0.061	0.0051	111.23	5.03	76.22
-0.1357	0.061	0.0076	112.35	5.1	77.64
-0.1357	0.061	0.0102	112.51	4.67	78.75
-0.1357	0.061	0.0127	113.8	0.88	80.71
-0.1357	0.061	0.0152	113.96	1.03	81.89
-0.1357	0.061	0.0178	115	-4.39	83.39
-0.1357	0.061	0.0203	116.1	-5.52	85.12
-0.1357	0.061	0.0229	116.37	-1.91	86.44
-0.1357	0.061	0.0254	117.09	-6.15	88.21
-0.1357	0.061	0.0279	117.65	-6.69	89.16
-0.1357	0.061	0.0305	118.38	-11.8	90.52
-0.1357	0.061	0.033	118.95	-15.59	91.61
-0.1357	0.061	0.0356	119.69	-13.56	92.75
-0.1357	0.061	0.0381	120.5	-19.29	93.55
-0.1357	0.061	0.0407	120.76	-20.69	94.93
-0.1357	0.061	0.0432	120.91	-17.32	96.26
-0.1357	0.061	0.0457	121.45	-20.19	96.92
-0.1357	0.061	0.0483	121.64	-20.55	98.1
-0.1357	0.061	0.0508	122.33	-23	98.83
-0.1357	0.061	0.0534	94.87	29.31	88.7
-0.1357	0.061	0.0559	94.25	31.98	86.52
-0.1357	0.061	0.0584	91.4	38.11	84.79
-0.1357	0.061	0.0635	96.57	26.6	87.72
-0.1357	0.0559	0.0025	110.22	8.05	72.93
-0.1357	0.0559	0.0051	111.35	7.72	75.45

x (m)	y (m)	z (m)	u (m/s)	v (m/s)	w (m/s)
-0.1357	0.0559	0.0076	110.97	10.7	76.23
-0.1357	0.0559	0.0102	112.16	6.69	78.26
-0.1357	0.0559	0.0127	113.03	5.14	80.18
-0.1357	0.0559	0.0152	113.97	4.11	82.15
-0.1357	0.0559	0.0178	114.64	0.45	83.52
-0.1357	0.0559	0.0203	115.45	1.06	85.42
-0.1357	0.0559	0.0229	116.51	-5.35	87.4
-0.1357	0.0559	0.0254	117.43	-4.52	89.05
-0.1357	0.0559	0.0279	117.9	-10.49	90.37
-0.1357	0.0559	0.0305	118.27	-9.77	91.8
-0.1357	0.0559	0.033	119.41	-8.45	93.33
-0.1357	0.0559	0.0356	119.96	-13.5	94.3
-0.1357	0.0559	0.0381	120.61	-20.74	95.28
-0.1357	0.0559	0.0407	120.9	-17.29	95.81
-0.1357	0.0559	0.0432	121.37	-19.51	97.62
-0.1357	0.0559	0.0457	121.72	-18.89	98.49
-0.1357	0.0559	0.0483	122.14	-23.18	99.55
-0.1357	0.0559	0.0508	122.69	-23.28	100.42
-0.1357	0.0559	0.0534	92.09	34.08	87.88
-0.1357	0.0559	0.0559	93.28	29.8	87.03
-0.1357	0.0559	0.0584	89	40.54	84.11
-0.1357	0.0559	0.061	91.34	35.94	85.65
-0.1357	0.0559	0.0635	95.43	24.63	87.65
-0.1357	0.0508	0.0025	107.61	17.43	69.32
-0.1357	0.0508	0.0051	108.08	21.2	71.6
-0.1357	0.0508	0.0076	110.54	16.06	75.07

x (m)	y (m)	z (m)	u (m/s)	v (m/s)	w (m/s)
-0.1357	0.0508	0.0102	111.42	-19.68	77.18
-0.1357	0.0508	0.0127	112.6	-18.95	79.95
-0.1357	0.0508	0.0152	113.68	7.71	82.85
-0.1357	0.0508	0.0178	114.47	7.72	85.05
-0.1357	0.0508	0.0203	115.39	3.07	87.2
-0.1357	0.0508	0.0229	116.37	0.62	89.27
-0.1357	0.0508	0.0254	116.85	-0.15	90.86
-0.1357	0.0508	0.0279	117.9	-6.19	91.85
-0.1357	0.0508	0.0305	118.5	-8.14	93.44
-0.1357	0.0508	0.033	119.74	-12.07	94.73
-0.1357	0.0508	0.0356	119.89	-11.11	95.64
-0.1357	0.0508	0.0381	120.59	-16.21	96.76
-0.1357	0.0508	0.0407	121.35	-20.12	97.97
-0.1357	0.0508	0.0432	121.53	-20.55	99.49
-0.1357	0.0508	0.0457	122.16	-21.44	100.63
-0.1357	0.0508	0.0483	122.31	-25.45	101.43
-0.1357	0.0508	0.0508	122.95	-26.03	102.07
-0.1357	0.0508	0.0534	96.19	19	92.2
-0.1357	0.0508	0.0559	98.84	18.08	92.39
-0.1357	0.0508	0.0584	90.36	36.27	85.93
-0.1357	0.0508	0.061	97.97	19.71	90.55
-0.1357	0.0508	0.0635	100.51	13.41	91.28
-0.1357	0.0457	0.0025	104.76	27.67	65.14
-0.1357	0.0457	0.0051	107.68	26.3	70.4
-0.1357	0.0457	0.0076	108.85	24.51	73.87
-0.1357	0.0457	0.0102	110.12	20.43	77.61

x (m)	y (m)	z (m)	u (m/s)	v (m/s)	w (m/s)
-0.1357	0.0457	0.0152	112.46	11.57	83.75
-0.1357	0.0457	0.0178	113.58	10.02	87.56
-0.1357	0.0457	0.0203	114.52	9.71	89.73
-0.1357	0.0457	0.0229	115.21	4.58	92.27
-0.1357	0.0457	0.0254	116.01	3.62	93.46
-0.1357	0.0457	0.0279	117.48	-2.41	94.71
-0.1357	0.0457	0.0305	118.16	-3.53	96.6
-0.1357	0.0457	0.033	118.8	-4.38	97.63
-0.1357	0.0457	0.0356	119.11	-6.93	99.05
-0.1357	0.0457	0.0381	120.65	-14.96	99.26
-0.1357	0.0457	0.0407	121.74	-19.49	100.13
-0.1357	0.0457	0.0432	121.84	-20.76	102.2
-0.1357	0.0457	0.0457	122.66	-21.61	102.63
-0.1357	0.0457	0.0483	123.33	-28.45	103.7
-0.1357	0.0457	0.0534	97.08	16.78	93.53
-0.1357	0.0457	0.0559	97.58	18.73	92.97
-0.1357	0.0457	0.0584	91.46	33.82	86.93
-0.1357	0.0457	0.061	97.92	18.74	90.9
-0.1357	0.0457	0.0635	100.4	13.26	91.12
-0.1357	0.0432	0.0534	93.41	26.9	91.71
-0.1357	0.0432	0.0559	95.61	24.71	91.9
-0.1357	0.0432	0.0584	89.28	36.6	85.64
-0.1357	0.0432	0.061	95.24	25.83	89.25
-0.1357	0.0432	0.0635	98.09	16.71	88.97
-0.1357	0.0407	0.0025	104.52	18.29	60.93
-0.1357	0.0407	0.0076	101.63	33.1	71.38

x (m)	y (m)	z (m)	u (m/s)	v (m/s)	w (m/s)
-0.1357	0.0407	0.0102	104.02	26.23	75
-0.1357	0.0407	0.0127	106.27	23.04	79.64
-0.1357	0.0407	0.0152	110.55	13.64	85.05
-0.1357	0.0407	0.0178	112.84	8.39	87.81
-0.1357	0.0407	0.0203	113.95	5.57	91.34
-0.1357	0.0407	0.0229	114.84	6.22	93.27
-0.1357	0.0407	0.0254	115.64	0.29	95.14
-0.1357	0.0407	0.0279	117.03	-6.99	96.38
-0.1357	0.0407	0.0305	117.99	-9.97	98.19
-0.1357	0.0407	0.033	118.4	-10.16	100.08
-0.1357	0.0407	0.0356	119.37	-9.55	101.02
-0.1357	0.0407	0.0381	119.95	-12.54	101.75
-0.1357	0.0407	0.0407	120.84	-18.18	102
-0.1357	0.0407	0.0432	121.59	-19.92	103.63
-0.1357	0.0407	0.0457	121.88	-23.51	104.22
-0.1357	0.0407	0.0483	123.39	-28.28	104.91
-0.1357	0.0407	0.0508	124.4	-31.88	106.67
-0.1357	0.0407	0.0534	95.47	22.93	93.33
-0.1357	0.0407	0.0559	95.86	20.51	92.33
-0.1357	0.0407	0.0584	89.29	36.54	85.87
-0.1357	0.0407	0.061	96.79	22.41	89.59
-0.1357	0.0407	0.0635	99.25	16.5	89.32
-0.1357	0.0381	0.0025	99.5	11.6	52.09
-0.1357	0.0381	0.0051	93.76	44.11	58.4
-0.1357	0.0381	0.0076	100.42	51.43	67.93
-0.1357	0.0381	0.0102	106.35	34.81	75.67

x (m)	y (m)	z (m)	u (m/s)	v (m/s)	w (m/s)
-0.1357	0.0381	0.0127	110.14	23.99	80.93
-0.1357	0.0381	0.0152	112.92	18.24	85.34
-0.1357	0.0381	0.0178	114.65	7.02	88.38
-0.1357	0.0381	0.0203	114.03	4.47	90.1
-0.1357	0.0381	0.0229	115.3	-1.53	92.4
-0.1357	0.0381	0.0254	116.37	-1.62	94.89
-0.1357	0.0381	0.0279	118.02	-7.15	96.84
-0.1357	0.0381	0.0305	117.38	-3.23	97.9
-0.1357	0.0381	0.033	118.26	-6.23	100.06
-0.1357	0.0381	0.0356	119.91	-14.18	101.97
-0.1357	0.0381	0.0381	120.64	-11.5	103.27
-0.1357	0.0381	0.0407	121.95	-15.01	103.53
-0.1357	0.0381	0.0432	117.47	-17.18	112.02
-0.1357	0.0381	0.0457	122.65	-20.82	105.95
-0.1357	0.0381	0.0483	123.73	-26.54	106.75
-0.1357	0.0381	0.0508	124.22	-27.52	107.59
-0.1357	0.0381	0.0534	95.96	19.47	93.84
-0.1357	0.0381	0.0559	96.3	19.94	92.84
-0.1357	0.0381	0.0584	91.04	33.02	87.3
-0.1357	0.0381	0.061	99.91	12.4	91.42
-0.1357	0.0381	0.0635	102.27	10.09	90.43
-0.1357	0.0356	0.0025	70.25	100.66	36.05
-0.1357	0.0356	0.0051	108.01	5.42	67.2
-0.1357	0.0356	0.0076	110.1	8.31	71.29
-0.1357	0.0356	0.0102	111.2	7.39	74.95
-0.1357	0.0356	0.0127	112.03	3.87	79.54

x (m)	y (m)	z (m)	u (m/s)	v (m/s)	w (m/s)
-0.1357	0.0356	0.0152	112.82	3.37	82.31
-0.1357	0.0356	0.0178	113.72	2.72	84.91
-0.1357	0.0356	0.0203	114.74	5.14	87.35
-0.1357	0.0356	0.0229	115.34	5.18	89.85
-0.1357	0.0356	0.0254	115.64	5.32	91.95
-0.1357	0.0356	0.0279	116.14	4.35	94.2
-0.1357	0.0356	0.0305	118.35	-10.75	102.58
-0.1357	0.0356	0.033	116.16	-19.96	108.42
-0.1357	0.0356	0.0356	112.93	-12.25	107.55
-0.1357	0.0356	0.0381	116.84	-22.09	107.09
-0.1357	0.0356	0.0407	116.99	-23.39	109.12
-0.1357	0.0356	0.0432	118.64	-29.4	110.93
-0.1357	0.0356	0.0457	118.64	-33.26	112.77
-0.1357	0.0356	0.0483	120.27	-33.94	113.43
-0.1357	0.0356	0.0508	122.33	-37.53	113.04
-0.1357	0.0356	0.0534	94.15	23.24	93.2
-0.1357	0.0356	0.0559	96.95	18.56	93.8
-0.1357	0.0356	0.0584	89.88	32.93	86.86
-0.1357	0.0356	0.061	98.11	18.61	89.99
-0.1357	0.0356	0.0635	101.3	12.9	87.79
-0.1357	0.033	0.0127	112.55	14.68	74.14
-0.1357	0.033	0.0152	113.17	14.07	76.71
-0.1357	0.033	0.0178	113.18	9.99	79.78
-0.1357	0.033	0.0203	113.88	-1.69	82.73
-0.1357	0.033	0.0229	123.35	-24.5	92.28
-0.1357	0.033	0.0254	134.89	-49.38	102.17

x (m)	y (m)	z (m)	u (m/s)	v (m/s)	w (m/s)
-0.1357	0.033	0.0279	132.27	-46.79	110.76
-0.1357	0.033	0.0305	124.15	-30.3	111.3
-0.1357	0.033	0.033	128.29	-31.06	109.13
-0.1357	0.033	0.0356	125.77	-36.97	117.1
-0.1357	0.033	0.0381	122.48	-42.01	118.77
-0.1357	0.033	0.0407	123.5	-43.02	116.63
-0.1357	0.033	0.0432	124.03	-42.84	115.51
-0.1357	0.033	0.0457	123.71	-42.07	115.62
-0.1357	0.033	0.0483	125.02	-46.52	116.95
-0.1357	0.033	0.0508	125.31	-46.53	116.5
-0.1357	0.033	0.0534	96.23	14.97	94.79
-0.1357	0.033	0.0559	97.48	14.52	94
-0.1357	0.033	0.0584	90.84	31.25	87.34
-0.1357	0.033	0.061	97.95	17.41	88.43
-0.1357	0.033	0.0635	103.48	13.7	84.56
-0.1357	0.0305	0.0229	114.77	-6.97	82.38
-0.1357	0.0305	0.0254	115.44	-14.74	85.42
-0.1357	0.0305	0.0279	116.35	-15.99	88.48
-0.1357	0.0305	0.0305	110.1	-17.19	101.84
-0.1357	0.0305	0.033	108.85	-13.29	106.96
-0.1357	0.0305	0.0356	115.57	-14.68	101.05
-0.1357	0.0305	0.0381	112.77	-12.21	107.8
-0.1357	0.0305	0.0407	120.73	-37.08	119.59
-0.1357	0.0305	0.0432	120.37	-40.24	114.95
-0.1357	0.0305	0.0457	121.37	-42.28	113.23
-0.1357	0.0305	0.0483	122.84	-42.52	113.69

x (m)	y (m)	z (m)	u (m/s)	v (m/s)	w (m/s)
-0.1357	0.0305	0.0508	123.76	-44.77	115.86
-0.1357	0.0305	0.0534	100.51	7.56	97.34
-0.1357	0.0305	0.0559	102.3	2.24	97.21
-0.1357	0.0305	0.0584	95.91	18.41	90.33
-0.1357	0.0305	0.061	105.2	7.06	87.46
-0.1357	0.0305	0.0635	112	-1.63	85.06
-0.1357	0.0279	0.0305	100.45	13.13	76.5
-0.1357	0.0279	0.033	107.01	-24.56	104.94
-0.1357	0.0279	0.0356	107.95	-24.31	108.77
-0.1357	0.0279	0.0381	109.77	-14.97	103.78
-0.1357	0.0279	0.0407	121.7	-32.78	107.57
-0.1357	0.0279	0.0432	121.66	-43.13	119.66
-0.1357	0.0279	0.0483	124.97	-46.37	111.41
-0.1357	0.0279	0.0508	121.54	-42.86	110.47
-0.1357	0.0279	0.0534	98.46	9.19	95.51
-0.1357	0.0279	0.0559	102.04	3.35	95.88
-0.1357	0.0279	0.0584	97.82	17.19	86.38
-0.1357	0.0279	0.061	107.73	7.8	83.73
-0.1357	0.0279	0.0635	112.89	0.52	81.94
-0.1357	0.0254	0.0356	94.37	5.14	92.11
-0.1357	0.0254	0.0381	97.91	-10.13	103.96
-0.1357	0.0254	0.0407	97.43	10.88	92.69
-0.1357	0.0254	0.0432	100.76	10.77	95.28
-0.1357	0.0254	0.0457	111.28	-16.73	107.84
-0.1357	0.0254	0.0483	108.66	-11.47	103.75
-0.1357	0.0254	0.0508	106.54	-12.04	100.46

x (m)	y (m)	z (m)	u (m/s)	v (m/s)	w (m/s)
-0.1357	0.0254	0.0534	96.07	12.57	91.69
-0.1357	0.0254	0.0559	106.91	1.65	90.09
-0.1357	0.0254	0.0584	100.92	18.46	79.99
-0.1357	0.0254	0.061	109.85	8.32	79.67
-0.1357	0.0254	0.0635	116.88	-3.65	80.16
-0.1357	0.0229	0.0432	94.58	14.8	88.4
-0.1357	0.0229	0.0457	110.13	-4.17	89.08
-0.1357	0.0229	0.0483	114.86	-17.38	101.41
-0.1357	0.0229	0.0508	116.29	-32.28	106.74
-0.1357	0.0229	0.0534	111.98	-6.19	91.81
-0.1357	0.0229	0.0559	114.82	-9.65	85.61
-0.1357	0.0229	0.0584	108.12	9.28	78.39
-0.1357	0.0229	0.061	120.81	-17.23	82.51
-0.1357	0.0229	0.0635	124.54	-13.13	80.69
-0.1357	0.0203	0.0432	79.31	29.09	83.98
-0.1357	0.0203	0.0457	77.63	34.65	82.08
-0.1357	0.0203	0.0483	81.16	47.47	73.72
-0.1357	0.0203	0.0508	114.69	-15.83	96.19
-0.1357	0.0203	0.0534	95.43	25.92	80.76
-0.1357	0.0203	0.0559	96.48	23.46	75.4
-0.1357	0.0203	0.0584	109.38	12.47	71.99
-0.1357	0.0203	0.061	122.32	-11.39	77.69
-0.1357	0.0203	0.0635	123.07	-15.42	78.16
-0.1357	0.0178	0.0457	112.54	-24.66	85.63
-0.1357	0.0178	0.0483	113.53	-12.8	76.54
-0.1357	0.0178	0.0508	115.92	1.27	70.17

x (m)	y (m)	z (m)	u (m/s)	v (m/s)	w (m/s)
-0.1357	0.0178	0.0534	115.2	8.22	69.06
-0.1357	0.0178	0.0559	118.11	-2.61	73.13
-0.1357	0.0178	0.0584	104.83	27.58	63.21
-0.1357	0.0178	0.061	118.48	0.81	69.78
-0.1357	0.0178	0.0635	123.71	-7.69	73.09
-0.1357	0.0152	0.0457	104.09	16.77	56.82
-0.1357	0.0152	0.0483	108.46	12.14	57.28
-0.1357	0.0152	0.0508	111.07	12.55	56.61
-0.1357	0.0152	0.0534	102.81	33.27	51.32
-0.1357	0.0152	0.0559	105.98	28.8	56.92
-0.1357	0.0152	0.0584	104.23	31.11	57.08
-0.1357	0.0152	0.061	109.28	20.3	59.88
-0.1357	0.0152	0.0635	117.97	2.83	65.38
-0.1357	0.0127	0.0483	109.6	22.4	45.49
-0.1357	0.0127	0.0508	117.9	4.16	52.29
-0.1357	0.0127	0.0534	105.71	28.32	46.23
-0.1357	0.0127	0.0584	106.32	35.41	50.89
-0.1357	0.0127	0.061	105.31	33.96	51.71
-0.1357	0.0127	0.0635	112.49	19.4	57.05
-0.1357	0.0102	0.0483	117.99	10.02	41.16
-0.1357	0.0102	0.0508	120.37	9.96	45.49
-0.1357	0.0102	0.0534	117.29	11.18	46.91
-0.1357	0.0102	0.0559	113.45	20.43	46.13
-0.1357	0.0102	0.0584	112.64	26.02	47.87
-0.1357	0.0102	0.061	113	25.97	50.61
-0.1357	0.0102	0.0635	113.6	22.37	53.55

x (m)	y (m)	z (m)	u (m/s)	v (m/s)	w (m/s)
-0.1357	0.0076	0.0508	122.15	12.13	35.99
-0.1357	0.0076	0.0559	114.87	21.27	40.17
-0.1357	0.0076	0.0584	115.76	20.92	43.81
-0.1357	0.0076	0.061	112.66	26.22	45.26
-0.1357	0.0076	0.0635	111.04	33.54	47.35
-0.1357	0.0051	0.0483	129.59	4.96	24.07
-0.1357	0.0051	0.0508	130.61	7.1	31.07
-0.1357	0.0051	0.0534	127.9	11.11	35.63
-0.1357	0.0051	0.0559	124.41	15.44	38.85
-0.1357	0.0051	0.0584	120.03	18.36	41.01
-0.1357	0.0051	0.061	116.95	26.35	43.04
-0.1357	0.0051	0.0635	123.14	13.82	51.36
-0.1357	0.0025	0.0508	125.93	24.42	20.43
-0.1357	0.0025	0.0534	124.55	28	26.24
-0.1357	0.0025	0.0559	120.32	31.07	30.61
-0.1357	0.0025	0.0584	119.73	26.34	36.77
-0.1357	0.0025	0.061	115.02	33.55	39.04
-0.1357	0.0025	0.0635	115.38	31.06	44.07
-0.1357	0	0.0635	104.5	71.6	36.93

Laser Velocimetry Seed Particles Within Compressible, Vortical Flows

Mark S. Maurice*

Wright Laboratory, Wright-Patterson Air Force Base, Ohio 45433

The ability of seed particles to penetrate and accurately track vortices is of critical importance to the analysis of laser velocimetry (LV) measurements within these flow structures. In applying a particle equation of motion to vortical flowfields which extend into the supersonic, compressible regime, two approaches are considered. First, an ideal, potential vortex is developed for a compressible flowfield. As an aid to the design and analysis of vortical flowfield surveys over a wide range of independent parameters, this model is used to plot the time and position at which any particle starting at rest within a vortex will begin to track the flow velocity within 3% error. As a specific application, the potential vortex is then used to estimate the dynamic bias of LV measurements taken within a vortex shed from a 75-deg delta wing at 20 deg angle of attack in a Mach 1.9 supersonic flow. The second approach uses a computationally derived Navier-Stokes flowfield solution in place of the potential vortex model. The computational flowfield method predicts that accurate LV measurements within the delta wing flowfield require seed particles no larger than 0.1–0.2 μm in diameter, and defines the unseeded inner vortex core region. Both approaches show an increase in velocity bias which is nearly proportional to particle diameter, stressing the need for a monodisperse seed of known size to resolve particle bias in complex flows.

Nomenclature

C_d	= drag coefficient, Eq. (15)
C_{d_i}	= function defined by Eq. (16)
C_p	= specific heat
d	= particle diameter
G	= function defined by Eq. (17)
h	= function defined by Eq. (18)
L	= root chord length
M	= Mach number
m	= mass
P	= pressure
R	= gas constant
Re_0	= Reynolds number, Eq. (2)
r	= radial spacial coordinate
r^*	= transformed, dimensionless radial coordinate, Eq. (12)
S	= Sutherland viscosity constant
St	= Stokes number, Eq. (4)
s	= distance, used in Eq. (6)
T	= temperature
t	= time
u	= fluid velocity
v	= particle velocity
w	= modified particle relative velocity, Eq. (14)
x, y, z	= Cartesian spacial coordinates
%ERR	= measure of particle velocity bias, Eqs. (24) and (25)
α	= angle of attack
β	= density ratio, Eq. (3)
Γ	= circulation
γ	= ratio of specific heats
θ	= angular spacial coordinate in a cylindrical system
μ	= molecular viscosity
π	= dimensionless variable groups, Eqs. (26–28)

ρ	= density
τ	= dimensionless time, Eq. (23)
ω	= vorticity

Subscripts

f	= fluid property
i, j	= Cartesian coordinate indicial notation
o	= property in the outer field of a two-dimensional vortex
p	= particle property
R	= the relative difference between the particle and the fluid
0	= initial condition

Introduction

THE dynamics of small particles within aerodynamic flowfields are of interest for a variety of applications. In propulsive engines, for example, combustion particles can have an erosive effect on turbine blades, as well as contributing to performance losses through the exit nozzle. External aerodynamic and control surface degradation can be strong functions of atmospheric dispersion, and sediment transport can be modeled by the dynamics of individual particles. In the application of flow visualization or laser velocimetry, however, it is required that the particle dynamics of the seed material describe the fluid dynamics of the flowfield. The seed particles are assumed to follow the fluid streamlines, and not to alter the corresponding unseeded flow.

In flow regions with large gradients such as near shock waves, or regions with high turbulence frequencies, particle dynamic bias can dominate laser velocimetry (LV) measurements. For the case of a seed particle passing through a shock wave, it has been shown by Nichols¹ that the particle lag can be substantial. If the mean velocity and turbulence intensity are determined from ensembled averages from a variety of particle sizes passing through the shock wave and measured at a single downstream location, these quantities may be grossly overestimated. On the other hand, it has been shown by Hjelmfelt and Mockros² that a particle subjected to a high-frequency, oscillating flowfield may greatly underestimate the turbulence intensity of the fluid.

Received Sept. 14, 1990; presented as Paper 91-0292 at the AIAA 29th Aerospace Sciences Meeting, Reno, NV, Jan. 7–10, 1991; revision received April 2, 1991; accepted for publication April 24, 1991. This paper is declared a work of the U.S. Government and is not subject to copyright protection in the United States.

*Mechanical Engineer, WL/FIMN. Member AIAA.

APPENDIX B: PARTICLE DYNAMICS IN VORTICAL FLOWS

This appendix contains details of the particle dynamics in vortical flows. It is a reproduction of an AIAA Journal article (Ref 11) written as a work of the Aeromechanics Division, Flight Dynamics Directorate, Wright Laboratory, Wright-Patterson Air Force Base.

Although fluid streamlines are circular within a two-dimensional potential vortex, centrifugal forces can cause seed particles to move radially away from the vortex origin. Consequently, LV velocity measurements within vortical flowfields¹⁻³ may be biased. For an incompressible, potential vortex flow, velocity bias can be computationally investigated using a simplified equation of motion derived by Dring and Suo,⁴ who prescribe particle position in terms of three dimensionless parameters that are constant throughout the flow. For this case,

$$\frac{r}{r_0} = f(Re_0, \beta, St) \quad (1)$$

where

$$Re_0 = \frac{\rho_f v_0 r_0}{\mu} \quad (2)$$

$$\beta = \rho_f / \rho_p \quad (3)$$

and

$$St = \frac{\rho_p v_0 d^2}{18 r_0 \mu} \quad (4)$$

For compressible flow, all three independent parameters vary radially through the vortex. If these variables are held constant by defining them in terms of the total density and temperature of the flowfield, and trajectories are computed by an equation of motion which includes compressibility effects, it can be seen in Fig. 1 that as the initial Mach number of the particle increases into the compressible flow regime, the particle trajectory shows a substantial increase in bias. Consequently, in a compressible, vortical flow, an incompressible analysis can underestimate the particle velocity bias.

Approach

Potential Vortex

Although classical text book derivations assume the potential vortex to be an incompressible flow when deriving the velocity field,^{7,8} the approach is extendible to compressible flowfields. In a compressible or incompressible flow, the potential vortex field is irrotational. Therefore, it is required that

$$\omega_r = \frac{\partial u_\theta}{\partial r} + \frac{1}{r} \left(u_r - \frac{\partial u_r}{\partial \theta} \right) = 0 \quad (5)$$

Since a potential vortex has no radial velocity component, and since the angular velocity component is only a function of ra-

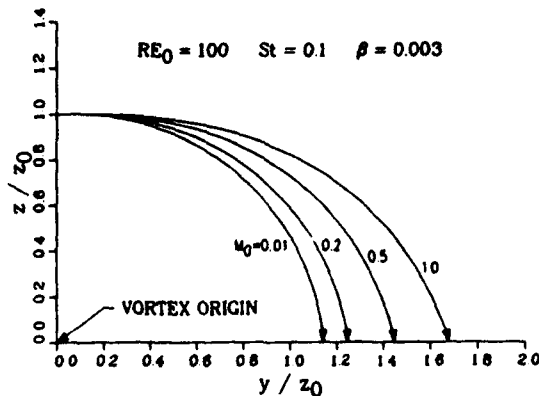


Fig. 1 Particle trajectories within a potential vortex in a compressible flow.

dial distance, Eq. (5) reduces to a first-order ordinary differential equation with an integration constant related to the vortex strength by the application of Stokes' theorem:

$$\Gamma = -\oint \mathbf{u} \cdot d\mathbf{s} \quad (6)$$

The resulting vortex velocities are

$$u_\theta = \frac{-\Gamma}{2\pi r} \quad (7)$$

and

$$u_r = 0 \quad (8)$$

Since this velocity field satisfies the compressible form of the continuity equation, the flowfield is physically possible. If the radial direction of the vortex lies on the y - z plane of a Cartesian coordinate system, the two-dimensional vortical field can be superimposed with a constant normal velocity in the x direction. The resulting three-dimensional flowfield will then have helical streamlines that rotate about the x axis. This flowfield can be used as a simple model of vortices that are shed from aerodynamic surfaces, recognizing that it does not account for axial variations of vortex strength or the development of a viscous core.

Another consideration for a potential vortex in a compressible flow is the limit of the mathematical model. For the incompressible case, the temperature is considered constant throughout the field, leaving only the infinite velocity at the center of the vortex as a limit. In a compressible flow, however, the temperature decreases toward zero as the velocity becomes infinite. To examine the inner limit with respect to commonly used constitutive equations for thermodynamic closure, it is best to temporarily decouple the constant axial velocity from the vortical flow plane. Since the flow can be considered isentropic and adiabatic, the axial velocity can be used to relate the total temperature, pressure, and density of the flowfield to the static values in the outer vortex region which approaches zero velocity in the vortical flow plane. These "outer" values can then be considered as stagnation values for the decoupled two-dimensional vortex flowfield. Within the region of the flowfield where the perfect gas law and calorically perfect gas assumption hold,

$$\frac{T}{T_s} = (P) \quad (9)$$

$$\frac{P}{P_s} = (P)^{\gamma/(\gamma-1)} \quad (10)$$

and

$$\frac{\rho}{\rho_s} = (P)^{1/(\gamma-1)} \quad (11)$$

where

$$P = 1 - \frac{\Gamma^2}{8\pi^2 r^2 C_p T_s} \quad (12)$$

The thermodynamic profiles in terms of the transformed radial coordinate are shown in Fig. 2. For air, the stagnation temperature within the vortical plane can be as high as 470 K, based on an arbitrary maximum of 2% error in the calorically perfect gas assumption. The inner limit of the model, based on a maximum 3% error in Sutherland's viscosity law, is at radial distance from the vortex origin where the stagnation temperature has decreased to 167 K.

The corresponding range of P_s extends from near vacuum to an upper limit defined by the validity of the perfect gas law. For a maximum 2% error, any P_s up to 11.2 atm is valid over the entire range of T_s .

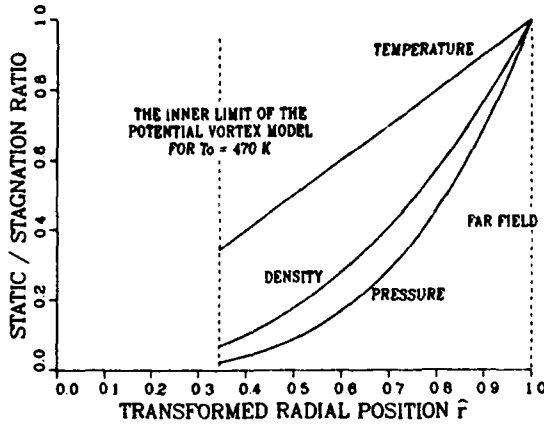


Fig. 2 Thermodynamic profiles through a potential vortex in a compressible flow.

Particle Equation of Motion

The equation set used to describe the particle motion is developed by Nichols,⁹ and includes the influences of Stokes' drag, resultant pressure, apparent mass, gravitational forces, and the Basset history integral. For application to the vortical flow, the gravitational term and the Basset history integral have been excluded. The Basset term can be significant when the particle density is of the same order of magnitude as the fluid density, or when the particle relative acceleration is large compared with the particle relative velocity. In this case, as in most numerical solutions, the Basset term is neglected because the numerically evaluated integral is found to be either negligible, highly unstable, or potentially biased by the accumulation of roundoff and truncation errors. The resulting differential equation for a general steady-state flow can be written as

$$\frac{dv_i}{dt} = \frac{-3C_d}{4d} \frac{m_f}{(m_p + m_f/2)} w_i |w| + \frac{m_f}{(m_p + m_f/2)} u_j \frac{\partial u_i}{\partial x_j} + \frac{m_f}{(m_p + m_f/2)} \frac{d}{dt} \left\{ u_i + \frac{d^2}{40} \nabla^2 u_i \right\} \quad (13)$$

where

$$w_i = v_i - u_i - \frac{d^2}{24} \nabla^2 u_i \quad (14)$$

and each of the fluid properties and derivatives are evaluated with respect to the particle location.

The drag coefficient is evaluated by the drag law of Crowe^{9,10}:

$$Cd = (Cd_1 - 2) \exp\{-3.07 \gamma^{1/2} (M_R/Re_R) G(Re_R)\} + \{h(M_R)/(\gamma^{1/2} M_R)\} \exp\{-Re_R/(2M_R)\} + 2 \quad (15)$$

where

$$Cd_1 = \frac{24}{Re_R} (1 + 0.158 Re_R^{2/3}) \quad (16)$$

$$\log_{10} G(Re_R) = 1.25 \{1 + \tanh(0.77 \log_{10} Re_R - 1.92)\} \quad (17)$$

and

$$h(M_R) = \{2.3 + 1.7(T_p/T_f)^{1/2}\} - 2.3 \tanh(1.17 \log_{10} M_R) \quad (18)$$

Crowe's drag law is valid over a wide range of relative Reynolds and Mach numbers, and includes the effects of inertia, compressibility, rarefaction, and heat transfer.

Nichols⁹ shows that the particle equation of motion becomes stiff for small particle diameters. Consequently, his solutions for particle behavior through shock waves are piecewise, using Adams' technique where possible, and restarting the solution with slower Runge-Kutta integration when local stiffness causes Adams' method to diverge. To avoid the necessity of piecewise solutions while maintaining computational efficiency, solutions presented here are obtained by 4th order Runge-Kutta-Fehlberg (RKF) numerical integration. The RKF method is ideally suited for this situation since it estimates the local stiffness of the equation at each time step, and adjusts the step size accordingly. Results include a general consideration of trajectories and velocity bias within the potential vortex model, specific application of the model to an experimental LV survey, and the use of a computational fluid dynamics (CFD)-generated vortical flowfield in place of the model.

Results

Dimensional Analysis

The particle equation of motion described by Eq. (13) requires the coupled solution of three first-order differential equations initialized by particle position and velocity within a specified vortical field. To reduce the equation set for analysis, consider the slightly more specific case of an LV seed particle traveling downstream in airflow (in the x direction), and at time zero, it becomes surrounded by a potential vortex. If the particle is traveling with the same initial constant downstream velocity as the flow, the equation of motion for the x direction decouples from the vortical flow in the y - z plane. Since there are no initial forces on the particle in the x direction, the equations show that the downstream particle velocity will remain constant. Additionally, since the vortex is axisymmetric, one initial condition parameter can be eliminated by choosing y_0 as the initial particle position, and setting z_0 to zero. Also, since the particle is assumed to have no initial velocity other than in the x direction, both of the initial velocity parameters in the vortical plane can be set to zero.

Analysis of the reduced equation set in the vortical plane coupled with the various equations of closure require the following dimensional inputs:

$$u_0, \rho_0, T_0, \mu_0, S, d, \rho_p, y_0 \quad (19)$$

where S is Sutherland's constant for air, and the outer viscosity can be evaluated by Sutherland's law for the input value of T_0 . These dimensional inputs describe the dependent variables:

$$y, z, v_y, v_z, t \quad (20)$$

Application of the Buckingham Π Theorem^{7,8} reduces the dimensional equation set to a function in terms of five dimensionless, independent parameters:

$$\frac{T_0}{S}, \frac{u_0^2}{RT_0}, \frac{\rho_0 u_0 d}{\mu_0}, \frac{\rho_p}{\rho_0}, \frac{y_0}{d} \quad (21)$$

Additional trial-and-error analysis shows that the effect of the parameter involving Sutherland's constant is negligible, and that the density ratio and initial distance parameters can be combined. The resulting dimensionless equation set is

$$\frac{y}{y_0}, \frac{z}{y_0}, \frac{v_y}{u_0}, \frac{v_z}{u_0}, \tau = f\left\{\frac{u_0^2}{RT_0}, \frac{\rho_p u_0 d}{\mu_0}, \frac{y_0 \rho_p}{d \rho_0}\right\} \quad (22)$$

where

$$\tau = t u_0 / y_0 \quad (23)$$

Two of the dependent dimensionless parameters in Eq. (22) describe the particle velocities in the vortical plane. However,

describe the particle velocities in the vortical plane. However, for application to LV, it is the bias in these quantities that is important. Therefore, define

$$\%ERR_v = \frac{v_t - u_t}{(u_t^2 + u_r^2)^{1/2}} \times 100 \quad (24)$$

$$\%ERR_r = \frac{v_r - u_r}{(u_t^2 + u_r^2)^{1/2}} \times 100 \quad (25)$$

Since these two error parameters can be written as functions of the dimensionless groups, they can be used as dependent dimensionless parameters themselves.

The three independent dimensionless groups can be fully defined by inputs of outer temperature and density, initial flow-field velocity and particle position, and the particle density and diameter. In terms of dimensionless variables, these groups can be defined as

$$\pi_1 = u_0/(RT_o)^{1/2} \quad (26)$$

$$\pi_2 = \rho_o u_0 d / \mu_o \quad (27)$$

$$\pi_3 = (y_o \rho_o) / (d \rho_p) \quad (28)$$

The six independent dimensional parameters and the viscosity from Sutherland's law are bounded for LV purposes in Table 1. The corresponding ranges of the three π parameters are also shown.

Particle trajectories in the y - z plane for a single combination of π groups are shown in Fig. 3. For this case, the particle has moved to more than twice its initial radial position after three helical revolutions. Although the trajectory alone does not quantify the velocity bias, it does show the difficulty in maintaining seeded flow near the vortex origin.

For the same combination of π groups, the measurement error that will occur in the y and z velocity components as a function of dimensionless time is shown in Fig. 4. In general, the magnitude of velocity bias decreases from 100% at the initial condition toward 0% as the particle moves outward from the vortex origin to a radius where it accurately follows the fluid streamlines. Since the velocity normal to the vortical plane is constant, values of τ correspond linearly to particle translation along the x axis.

For the ranges of parameters selected in Table 1, the radial particle position and corresponding time at which the total magnitude of velocity bias decreases to 3% is shown in Figs. 5a-5c. On the log-log scale, the curves of radial position are shown to decrease nearly linearly towards conditions where any radial displacement of the particle is negligible. In terms of the dimensional parameters, this decrease corresponds to smaller particle diameters, an initial position further from the vortex origin, or lighter particles relative to the fluid density.

The corresponding curves for τ also decrease as π_3 increases, and include a sharp drop at the point where radial

translation becomes negligible. In general, damping the velocity bias from the initial conditions is much faster than any required radial translation of the particle. Consequently, the portion of the curve above the dip is for particles that must be translated further away from the vortex origin, while the portion of the curve below the dip corresponds to particles that are brought from rest to the fluid velocity at the initial radial particle position.

Application of the Potential Vortex

As a specific application, the potential vortex is used to model an LV measured supersonic vortex shed from a 75-deg delta wing at 20-deg angle of attack. The two-dimensional velocity vector field at 80% chord is shown in Fig. 6, and a comprehensive description of the experimental test and results can be found in Ref. 5. From the known stagnation conditions and freestream Mach number, the outer vortex temperature, density, and axial velocity are determined, and the density of the seed corresponds to the 10 cS silicon oil that was used for the test.

Three-dimensional LV measurements were made in the plane perpendicular to the model surface. However, it was found that by applying a rotational transformation to the data, lines emanating normal from the individual two-dimensional velocity vectors tend to converge towards a point. This point is estimated to be the vortex origin. The transformed velocity field shown in Fig. 6 corresponds to a "vortex angle of attack" of 8 deg from the freestream flow.

The corresponding values of vortex strength decrease from the outer edge of the wing towards the delta wing centerline. For this example, a nominal weighted average value of $-50 \text{ m}^2/\text{s}$ is used.

Using the inner limit of the potential vortex model as an initial position, the corresponding particle trajectories for various sizes of seed are shown in Fig. 7. Because of the high speed of the axial flow, the particles only travel about one-third of a helical revolution from the nose of the wing to the 80% chord location. However, the difference in individual trajectories is significant, showing a nearly circular path for the 0.1- μm particle while the 5.0- μm particle increases its radial distance from the vortex origin by more than 40%.

The radial position of particles at the 80% chord location as a continuous function of seed diameter is given in Fig. 8. Over the included range of 0.1-5.0 μm particles, the curve shows that the increase in radial translation is fairly linear.

The corresponding curve of the velocity bias at this chord location is given in Fig. 9. This curve is also fairly linear, showing a steady increase in bias from less than 0.5% for 0.1- μm particles to nearly 28% for 5.0- μm seed. This curve shows that seed diameters of the polydispersed silicon oil must be less than 0.833 μm in order to maintain a velocity bias of less than 3.0%.

Finally, the measurement error for three candidate particle sizes as a function of chord position is shown in Fig. 10. In each case, the particle bias at zero percent chord is 100%,

Table 1 Chosen ranges of dimensional and corresponding dimensionless parameters

Parameter	Range	Reasoning
T_o , K	176-470	The lower value is arbitrarily chosen so that $M \geq 0.5$ at the inner limit of the vortex model. The upper value is based on a maximum 2% error for the calorically perfect gas assumption.
ρ_o , kg/m ³	0.0375-4.011	Dependent on T_o , this range corresponds to the minimal range of 0.05 atm < P_o < 2 atm, which is an arbitrary range of interest.
μ_o , kg/ms	1.19E-5-2.56E-5	From Sutherland's viscosity law for the range of T_o .
U_o , m/s	10-780	The lower value is arbitrary, the high value, dependent on T_o , is the velocity at the inner limit of the vortex model.
ρ_p , kg/m ³	260-3960	This range covers a wide variety of LV seed, from hollow glass spheres to Al_2O_3 .
d , μm	0.2-100	This is a typical range for LV seed diameters.
y_o , m	0.001-2.0	This is a probable range of interest for wind-tunnel applications.
π_1	0.0273-2.144	π_1 , π_2 , and π_3 are based on appropriate combinations of dimensional parameters.
π_2	0.00293-12221	
π_3	9.47×10^{-3} -154269	

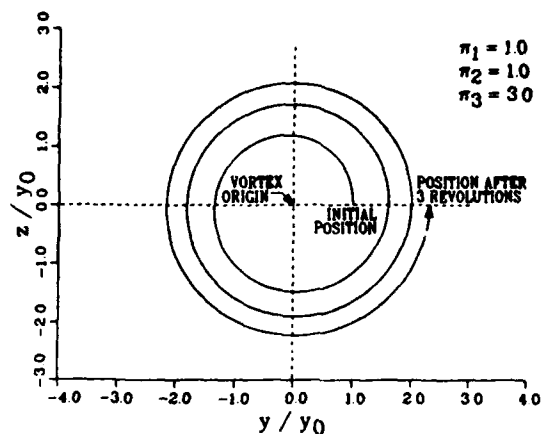


Fig. 3 Representative particle trajectory for one possible π group.

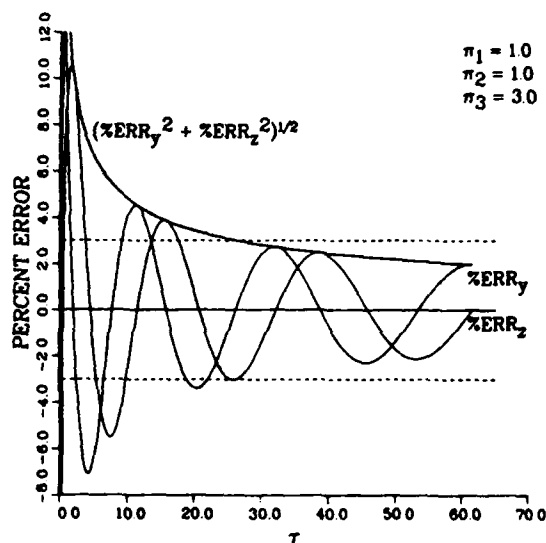


Fig. 4 Representative time history of velocity bias for one possible π group.

since the particles have no initial velocity in the vortical plane. By the time the particles move downstream only 2-5% chord, however, the initial bias is completely damped. The remaining bias is due to the tangential momentum of the particle in the vortical field, and slowly decays as the radial distance of the seed from the vortex origin increases.

Consequently, this example predicts that for seed particles of less than $0.833 \mu\text{m}$ in diameter, reasonably unbiased LV measurements can be made within the radial limits of the potential vortex model at any axial station downstream of about 10% chord. Since the inner bound of the model happens to be the approximate bound at which LV measurements were actually taken, the unmodeled viscous inner core of the vortex is inconsequential to this analysis. Furthermore, it was found that any possible initial velocities applied to the seed particles were quickly damped, making the results nearly independent of the simplified set of initial conditions used.

Application of a Computational Fluid Dynamics-Generated Vortical Field

As a second application of the particle equations of motion, the potential vortex model is replaced with a three-dimensional Navier-Stokes solution of a delta wing flowfield. For the same

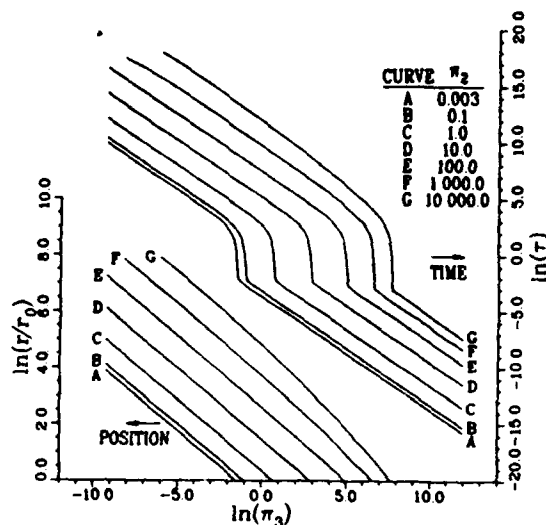


Fig. 5a Particle time and position at 3% velocity bias ($\pi_1 = 0.03$).

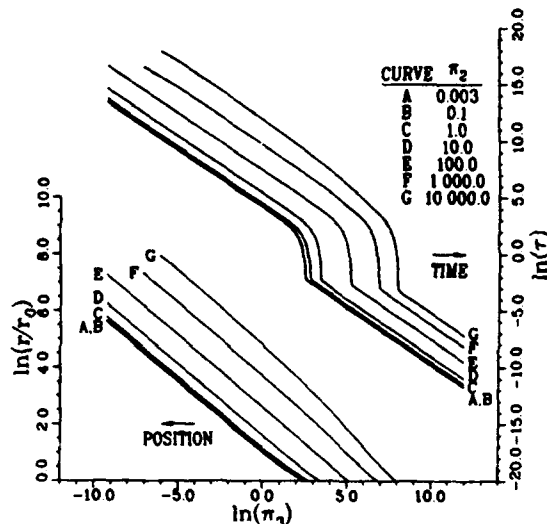


Fig. 5b Particle time and position at 3% velocity bias ($\pi_1 = 1.0$).

model geometry at slightly different flight conditions than the experimental case, two-dimensional cross sections of a portion of the delta wing flowfield calculated by Webster and Shang¹¹ are shown in Fig. 11. As represented by the 15 and 40% chord locations, the general form of the primary and secondary vortices appear to vary only slightly with chord, although the size of the structures varies proportionally with the wing span.

As an attempt to seed the inner core of the vortex, seed particles were initially positioned in the vicinity of the leading edge of the model. It was found, however, that the vertical momentum of the particles from the freestream angle of attack is too great. The particles enter the lower portion of the forming vortex, and continue to move vertically upward through the core and into the outer portion of the vortex before the initial vertical momentum is dissipated. By trial-and-error, it was found that the seed which penetrates deepest into the vortex core are particles that are swept around the edge of the wing from the underside.

Trajectories of seed particles that are initially positioned along the edge of the wing at 15% chord are shown in Fig. 12. As

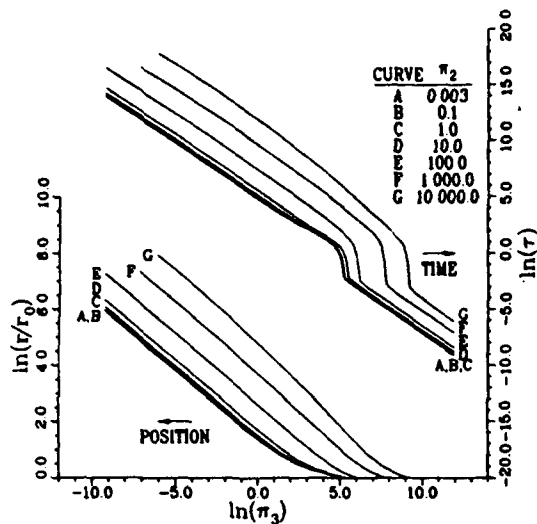


Fig. 5c Particle time and position at 3% velocity bias ($\pi_1 = 2.0$).

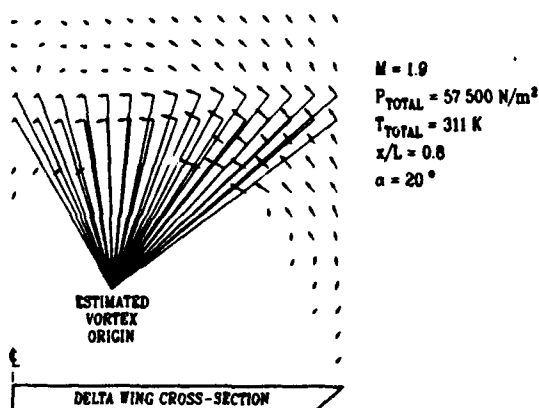


Fig. 6 LV measured velocity field produced by a delta wing (Ref. 5).

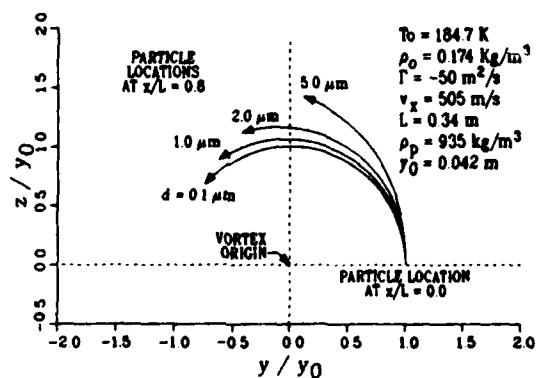


Fig. 7 Two-dimensional projection of silicon oil seed particle trajectories within a modeled delta wing vortex.

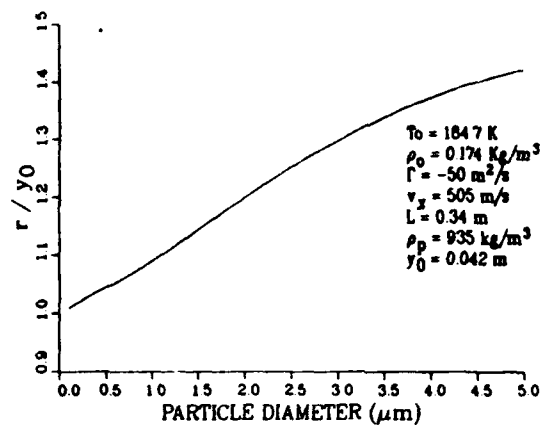


Fig. 8 Radial particle position at 80% chord within a modeled delta wing vortex.

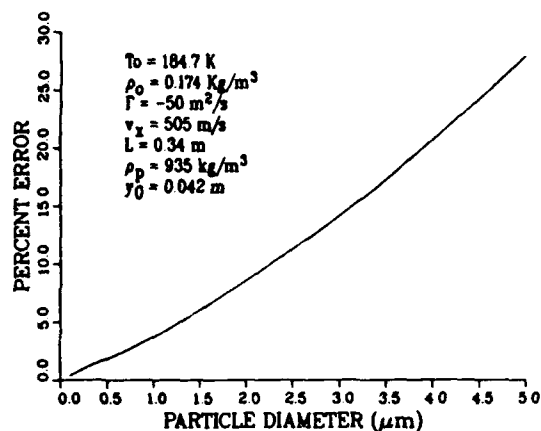


Fig. 9 Magnitude of velocity bias at 80% chord within a modeled delta wing vortex.

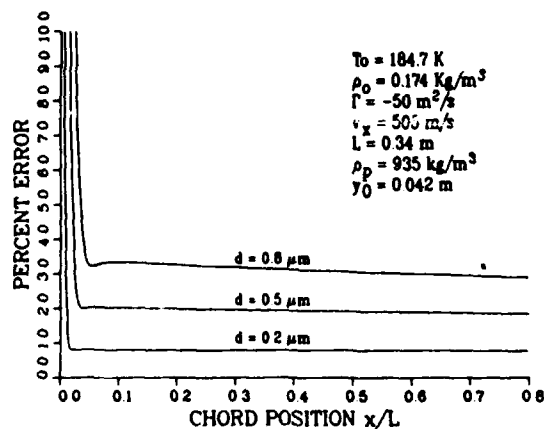


Fig. 10 Magnitude of velocity bias as a function of chord position within a modeled delta wing vortex.

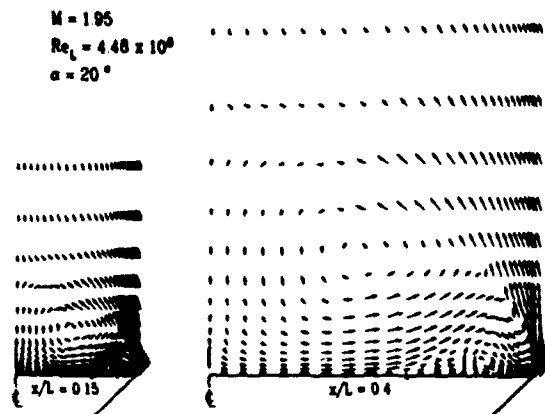


Fig. 11 Cross sections of a computationally derived vortical flowfield produced by a delta wing (Ref. 11).

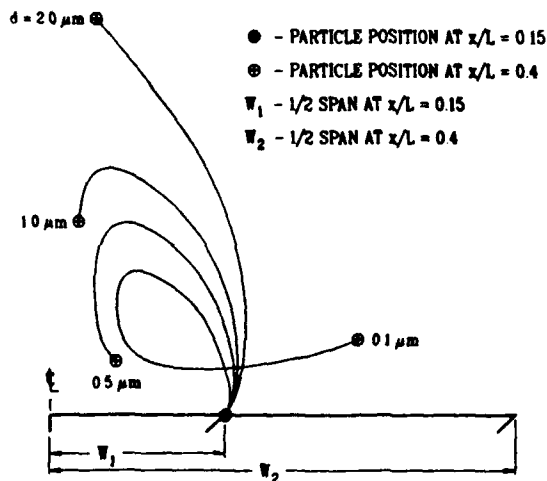


Fig. 12 Two-dimensional projection of silicon oil seed particle trajectories within a computationally derived delta wing flowfield.

the particles travel downstream, they are swept around the primary vortex. The smallest particle shown, $0.1 \mu\text{m}$, completes an entire helical revolution prior to reaching the 40% chord station, and maintains a velocity bias of less than 3%. The $2.0\text{-}\mu\text{m}$ particle, on the other hand, is centrifuged out of the vortex, and has a final velocity bias of over 50%.

Trajectories for $0.2\text{-}\mu\text{m}$ particles at different initial chord locations along the edge of the wing are shown in Fig. 13. In each case, the particles are traveling helically around the primary vortex, which is growing chordwise. The particle that starts at the 5% chord location is shown to travel once around the primary vortex, and then it breaks off to circle the secondary vortex. As that particle moves beyond the 40% chord location, it passes back from the secondary to the primary vortex.

If the 40% chord positions of each of the particles shown in Fig. 13 are connected, the resulting curve will be the inner core bound for the seed found at that profile location. This curve is shown in Fig. 14 for three particle diameters. As would be expected, the size of the unseeded inner core grows with the size of the seed. The $0.5\text{-}\mu\text{m}$ particles travel slightly less than one helical revolution, and have an average velocity bias at 40% chord of about 10%. The $0.2\text{-}\mu\text{m}$ particles have an average velocity bias of around 5%, and the seed that starts near the leading edge is shown to be circling the secondary

PARTICLE STARTING POSITION:

- - $x/L = 0.05$
 - - $x/L = 0.10$
 - - $x/L = 0.15$
 - ◇ - $x/L = 0.20$
 - × - $x/L = 0.25$
 - △ - $x/L = 0.30$
 - - $x/L = 0.35$
- $d = 0.2 \mu\text{m}$
 ● - PARTICLE POSITION AT $x/L = 0.4$

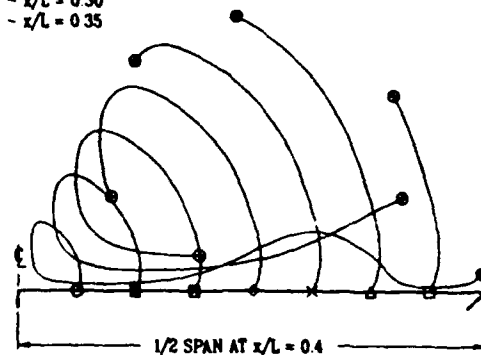


Fig. 13 Three-dimensional projection of silicon oil seed particle trajectories within a computationally derived delta wing flowfield. Each particle is initially at the outer edge of the wing.

- - FINAL PARTICLE POSITION FOR A PARTICLE WHICH STARTS AT $x/L = 0.38$
- - FINAL PARTICLE POSITION FOR A PARTICLE WHICH STARTS AT $x/L = 0.05$

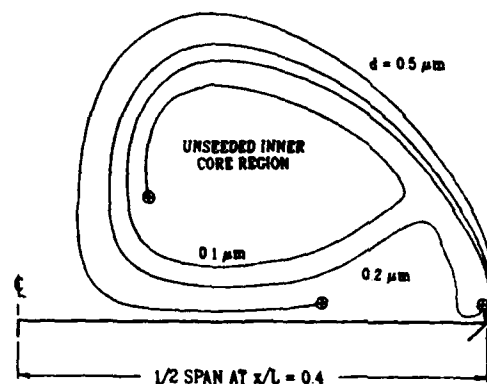


Fig. 14 Inner bounds of a silicon oil seeded flowfield at 40% chord within a computationally derived delta wing vortex.

vortex at the 40% chord location. The $0.1\text{-}\mu\text{m}$ seed, with an average velocity bias of about 3%, is entirely within the primary vortex at the 40% chord measurement station. Although the specific submicron particle size distribution of the experimental study is not known, the size and shape of the unseeded core, as determined by the LV surveys and laser light sheet visualization, correspond qualitatively with the analytical prediction.

Conclusions

Three contributions were made by this study. First, a three-dimensional potential vortex flowfield was developed and bounded for use as a mathematical model. Second, curves were presented that can be used to aid in the design and analysis of LV measurements in vortical flows over a large practical range of interest. Third, the particle equations of motion were coupled with a CFD-derived flowfield, showing the capability to numerically track the position and velocity bias of LV seed through highly complex flows.

Although the potential vortex is a very simple model of the delta wing vortex structure, it gave valuable insight into the behavior of the silicic acid seed in the wind-tunnel environment. It estimated the required particle diameter to within the same order of magnitude as using the CFD solution, and offers results for the entire class of solutions in terms of three dimensionless variables.

Tracking the particles through the CFD-generated flowfield offers the greatest potential to investigate seed density distributions and particle bias in any LV study which is coupled with a CFD effort. Using the RKF method of numerical integration to automatically adjust the time step based on equation stiffness makes the method numerically stable and efficient.

Both methods predict that the velocity bias within the delta wing vortex increases rapidly with particle diameter. Consequently, particle size must be carefully controlled in order to minimize particle dynamic bias. Future efforts will use the potential vortex model to design experiments and analyze data for vortical flows that do not have a companion CFD solution. When a CFD solution exists, it will be used with the particle equation of motion as a more precise method of quantifying the dynamic measurement bias.

Acknowledgments

The author thanks Dean Miller, George Seibert, Linda Smith, and Charles Tyler, who each contributed towards the collection and presentation of the LV measured flowfield, and also to Phillip Webster, who provided a complete numerical flowfield solution for this analysis.

References

- ¹Nichols, R. H., "Calculation of Particle Dynamics Effects on Laser Velocimetry Data," *Wind Tunnel Seeding Systems for Laser Velocimeters*, NASA CP2393, March 1985, pp. 1-11.
- ²Hjelmfelt, A. T., Jr., and Mockros, L. F., "Motion of Discrete Particles in a Turbulent Fluid," *Applied Scientific Research*, Vol. 16, 1966, pp. 149-161.
- ³Schwind, R. G., and Mullen, J. J., "Laser Velocimeter Measurements of Slender-Body Vortices," AIAA Paper 79-0302, New Orleans, LA, Jan. 1979.
- ⁴Abid, R., and Schmitt, R., "Experimental Study of a Turbulent Horseshoe Vortex Using a Three Component Laser Velocimeter," AIAA Paper 86-1069, Atlanta, GA, May 1986.
- ⁵Smith, L. G., Maurice, M. S., Seibert, G. L., and Tyler, C., "Laser Velocimetry Measurements of Supersonic Vortex Flows on a Simple Razor-Edged Delta Wing," AIAA Paper 91-1684, Honolulu, HI, June 1991.
- ⁶Dring, R. P., and Suo, M., "Particle Trajectories in Swirling Flows," *Journal of Energy*, Vol. 2, No. 4, 1978, pp. 233-237.
- ⁷Chow, C.-Y., and Kuethe, A. M., *Foundations of Aerodynamics: Basis of Aerodynamic Design*, 3rd ed., Wiley, New York, 1976, pp. 20-58, 422-426.
- ⁸Anderson, J. D., Jr., *Fundamentals of Aerodynamics*, McGraw-Hill, New York, 1984, pp. 21-26, 152-155.
- ⁹Nichols, R. H., "The Effect of Particle Dynamics on Turbulence Measurements with a Laser Doppler Velocimeter," Ph.D. Dissertation, Dept. of Aerospace Engineering, Univ. of Tennessee, Knoxville, TN, June 1986.
- ¹⁰Crowe, C. T., "Drag Coefficient of Particles in a Rocket Nozzle," *AIAA Journal*, Vol. 5, No. 5, 1967, pp. 1021-1022.
- ¹¹Webster, W. P., and Shang, J. S., "Comparison Between Thin Layer and Full Navier-Stokes Simulations Over a Supersonic Delta Wing," AIAA Paper 90-0589, Reno, NV, Jan. 1990.

APPENDIX C: COMPUTATIONAL FLUID DYNAMICS RESULTS

This appendix contains details of the computational fluid dynamics study of the supersonic vortex flowfield. It is a reproduction of an AIAA Journal article (Ref 13) written as a work of the Aeromechanics Division, Flight Dynamics Directorate, Wright Laboratory, Wright-Patterson Air Force Base.

Thin-Layer Full Navier-Stokes Simulations over a Supersonic Delta Wing

W. Phillip Webster* and Joseph S. Shang†

U.S. Air Force Wright Research and Development Center, Wright-Patterson Air Force Base, Ohio 45433

Steady flowfields describing the flow over a 75-deg swept delta wing at $M_\infty = 1.95$ and 4.48×10^6 were simulated at $\alpha = 20$ and 30 deg using two computer codes. Comparisons were made between calculations using 1) the laminar and turbulent thin-layer Navier-Stokes equations, and 2) laminar thin-layer and Navier-Stokes equations. At $\alpha = 20$ deg, each equation set captures the essential structure of the flow and the differences between their results are minor. Numerical results generated by a grid refinement study exhibited only a minor improvement. The Navier-Stokes equations were used to calculate the flow at $\alpha = 30$ deg. A region of reversed flow along the surface near the trailing edge was observed. The vertical extent of this region was much smaller, but the upstream propagation extended much farther than the thin-layer simulation.

Nomenclature

C_p	= coefficient of pressure
L	= root chord length
M	= Mach number
Re	= Reynolds number
U, V, W	= velocity components in coordinate directions
x, y, z	= coordinate directions
Y	= maximum span at a given x location
y^+	= nondimensional distance from surface, $z\sqrt{\tau_0/\rho\nu}$
α	= angle of attack
β	= leading-edge bevel
Γ	= sweep angle
ρ	= density
τ	= surface shear stress
∞	= freestream value
0	= surface value

Introduction

THE flow about modern high-speed aircraft with a delta planform at angle of attack is characterized by the presence of large spiraling vortices on the lee side of the wing. In many cases, these vortices are the primary structure in the flow affecting the performance of the aircraft. These vortices readily form at low angles of attack. With increasing angle of attack, secondary and tertiary vortices form due to boundary-layer separation. Flows over slender delta wings have been studied experimentally by Monnerie and Werle,¹ Hummel,² Miller and Wood,³ Stallings and Lamb,⁴ and Guyton,⁵ among others; they have been studied numerically by Rizzetta and Shang,⁶ Buter and Rizzetta,⁷ Thomas and Newsome,⁸ to name but a few. There have been numerous investigations of other delta-based planforms. These include, but are not limited to, delta wings with canard,⁹ crank delta wings,¹⁰ pitching delta wings,¹¹ and rocking delta wings.¹²

In a previous paper,¹³ the authors presented numerical simulations of vortical flow over a delta wing ($\Gamma = 75$ deg) at four angles of attack (10, 20, 30, and 35 deg) at a freestream Mach number of 1.95 and a Reynolds number of 4.48×10^6 . The

governing equations used were the unsteady, compressible, three-dimensional, thin-layer Navier-Stokes equations written in Reynolds averaged form. The computer code used to solve this set of equations was ARC3D, which is fully described by Pulliam.¹⁴ This code uses the approximately factorized implicit Beam-Warming algorithm and is diagonalized to accelerate convergence.

The previous results captured the essential structure of the vortical flow on the lee side of the delta wing. At $\alpha = 10$ and 20 deg, the results compared very favorably with experimental results. At $\alpha = 30$ and 35 deg, a large region of reversed flow was observed near the trailing edge. This reversed flow was contained in the low-pressure region associated with the secondary vortex. It extended from the trailing edge forward to 67% of the root chord for $\alpha = 30$ deg and forward to 56% of the root chord at $\alpha = 35$ deg.

This work left three areas in which the results were not satisfactory. The first problem area was the assumption of laminar flow. The high Reynolds number (4.48×10^6 based on root chord length) would indicate the flow to be turbulent. However, to focus the range of issues in the previous work, turbulence was not modeled. The second issue was the use of the thin-layer assumption. The thin-layer assumption is considered appropriate for vortical flows; however, its utility is unknown in the reversed flow region where stress components in the spanwise direction may not be negligible. The final problem area was the need for a grid resolution study that was not performed in the previous work.

Addressing each of these issues is the objective of this paper. In order to do this, a second computer code was used to solve the Navier-Stokes equations. This code (FDL3D-I), written by Visbal,¹⁵ is based, like ARC3D, on the approximately factorized implicit Beam-Warming algorithm; however, it has several differences from ARC3D. First, the code can solve either the full or thin-layer Navier-Stokes equations. Second, the code is not diagonalized but retains the block tridiagonal form; thus, it is first-order accurate in time. In addition to these major differences, there are several smaller differences between the two codes. Since FDL3D-I retains the block tridiagonal structure, the implicit damping terms are second order. Because of its scalar pentadiagonal form, ARC3D has both second- and fourth-order terms. In addition, the metric terms at boundaries in ARC3D are first-order accurate, whereas in FDL3D-I, they are second order.

In order to compare the codes as carefully as possible, the damping terms were maintained as nearly identical as possible. The coefficients for the second- and fourth-order explicit and second-order implicit were the same. To match the fourth-

Presented as Paper 90-0589 at the AIAA 28th Aerospace Sciences Meeting, Reno, NV, Jan. 8-11, 1990; received Feb. 8, 1990; revision received Sept. 27, 1990; accepted for publication Oct. 21, 1990. This paper is declared a work of the U.S. Government and is not subject to copyright protection in the United States.

*Aerospace Engineer, WL/FIMM. Member AIAA.

†Technical Manager, WL/FIMM. Associate Fellow AIAA.

order implicit term from ARD3D, additional second-order implicit damping was added to FDL3D. This results in the codes solving slightly different sets of equations, and small differences in the results were to be expected. One method to avoid this difference would have been not to use fourth-order damping; however, the solution became unstable.

The resolution of the issues just outlined was accomplished in the following manner. First, the effects of turbulence were evaluated using ARC3D. This was done since ARC3D has an implementation of the Baldwin-Lomax turbulence model, which is currently unavailable in FDL3D-I. Second, FDL3D-I was used to calculate the flowfield about a delta wing using the thin-layer approximation to validate FDL3D-I. This calculation used the same conditions and grid as the previous work at $\alpha = 20$ deg. These results were compared to the previous results as well as to experimental data. Third, the full Navier-Stokes equations were solved using FDL3D-I and compared to the thin-layer results, such that observed variations in the results could be attributed to the use of thin-layer or full Navier-Stokes equations and not to differences between the two codes. Fourth, the effects of grid resolution were investigated using the Navier-Stokes equations. The spanwise resolution over the delta wing and the normal resolution near the upper surface were increased by a factor of 2.

All of this work was done at $\alpha = 20$ deg, a condition that did not display significant reversed flow in the previous work. In order to determine the effects of using the full Navier-Stokes equations on the reversed flow region, the $\alpha = 30$ -deg case was solved using FDL3D-I. This angle of attack produced a significant region of reversed flow in the previous results.

Analysis

The vortical flow about a delta wing ($\Gamma = 75$ deg) was simulated numerically at $\alpha = 20$ deg and 30 deg, $M_\infty = 1.95$ and 4.48×10^6 . The delta wing configuration had a length of 33.9 cm, a thickness of 1.9 cm, and a leading-edge bevel $\beta = 35$ deg. Figure 1 is a sketch of the delta wing with relevant parameters labeled. This configuration was chosen to duplicate a parallel experimental study that is underway at the present time.

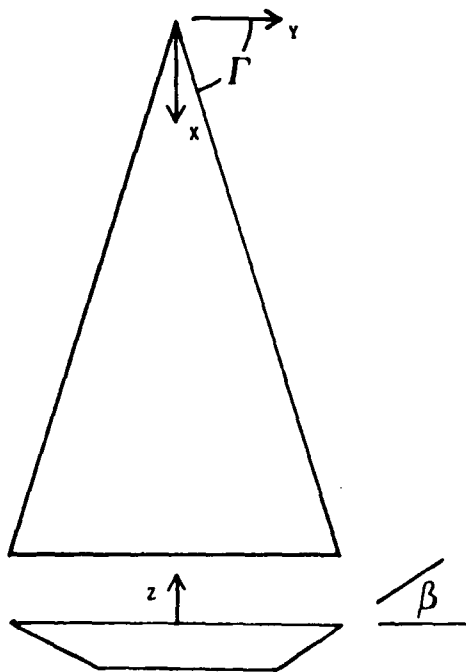


Fig. 1 Sketch of delta wing.

The governing equations were taken to be the unsteady, compressible, three-dimensional Navier-Stokes equations. The perfect gas law was used to relate the pressure, temperature and density, whereas Sutherland's equation was used to calculate the molecular viscosity. Two computer codes were used to solve this set of equations. The first, ARC3D, uses the thin-layer approximation. The second, FDL3D-I, has the option of solving either the full or thin-layer Navier-Stokes equations.

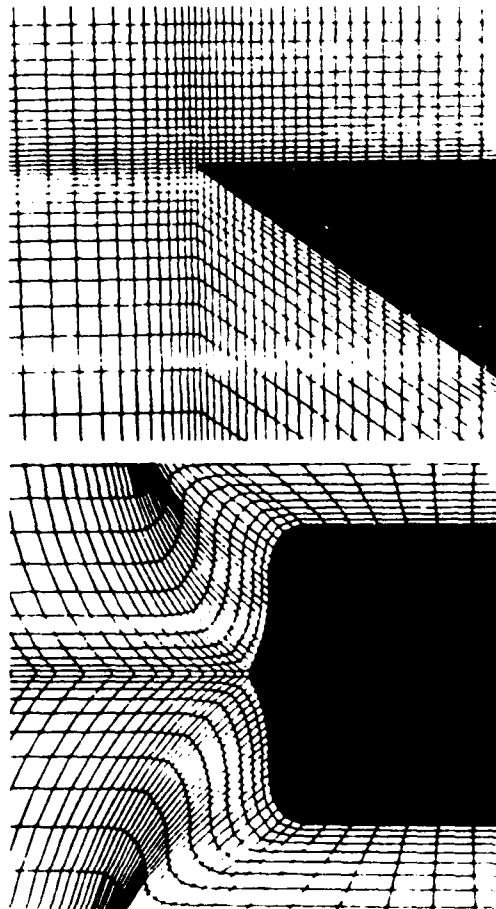
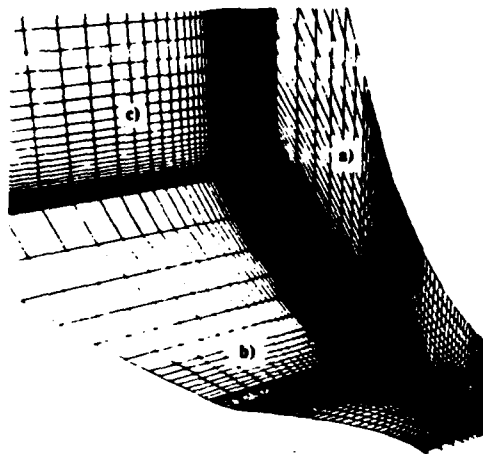


Fig. 2 Outline of the grid structure: a) global structure; b) outboard tip; c) trailing edge.

tions. The local time step for each code was scaled by $(1.0 + \sqrt{J})^{-1}$, where J is the Jacobian of the coordinate transformation.

The grids for these calculations were generated algebraically. The grid may be described as having an H-H structure. This type of grid was chosen to eliminate singular metrics at the leading edge and to facilitate modeling of the blunt trailing edge. Figures 2 show several planes that outline the global grid structure (Fig. 2a). The planes are the following: the symmetry plane (labeled A in the figure), the plane that contains the upper surface of the delta wing (labeled B), and the plane that is located at the downstream edge of the domain (labeled C). In addition, Figs. 2 show close-ups of the outboard tip (Fig. 2b) and the trailing edge (Fig. 2c), detailing the H-H structure. The trailing edge was rounded in order to smooth the grid. The normal grid spacing at the surface increased proportionally with the distance from the apex to a maximum of $10^{-3} \times L$ at the trailing edge. The grid was clustered in the streamwise direction at the leading and trailing edge with the spacing on the surface varying by almost three orders of magnitude. A more detailed discussion of the grid structure was reported previously.¹³

The coordinate system had its origin at the apex with the x axis chordwise along the upper surface in the plane of symmetry. The y axis was normal to the plane of symmetry and in the spanwise direction. The z axis was normal to the upper surface and in the plane of symmetry.

The primary grid had 80 grid points in the x direction with 5 ahead of the apex and 15 in the wake. In the y direction, there were 49 grid points inboard of the leading edge and 31 outboard for a total of 80 grid points. In the z direction, there were 80 grid points with 32 below and 48 above the delta wing. This resulted in a grid with a total of 512,000 grid points. This grid was used for the comparisons between ARC3D and FDL3D-I, the comparisons between the full and thin-layer Navier-Stokes equations using FDL3D-I, and for the turbulent calculation with ARC3D.

For the grid refinement study, a second system had an additional 49 grid points in the spanwise direction. A new grid point was inserted between each grid point on the surface. In the z direction, a new point was inserted between each of the first 21 points above the upper surface. This resulted in a grid with 1,032,000 grid points.

The final grid was based on the primary mesh system with an additional 30 points in the x direction. This increased the resolution at the trailing edge and matches the grid used in the previous work in which reversed flow was observed. This grid was used for the full Navier-Stokes calculation at $\alpha = 30$ deg by FDL3D-I.

Each of the simulations used the converged solution from the previous work¹³ as an initial condition. The L2 norm of the change in the dependent variables displayed a spike, which then quickly decreased to its starting value. The solution was then allowed to evolve until the L2 norm reached and maintained a constant value. It should be noted that the dependent variables in ARC3D are divided by the Jacobian whereas in FDL3D-I, they are not. This results in the L2 norm differing by several orders of magnitude between the two codes. All solutions were obtained using one processor on a Cray 2 supercomputer. The data processing rate is expressed in $\mu s/\text{point/iteration}$. The data processing rates were 39.46, 45.82, and 60.11, for ARC3D laminar, FDL3D-I thin layer, and FDL3D-I Navier-Stokes, respectively.

Results and Discussion

The first issue dealt with was that of turbulence. ARC3D, with the turbulence model of Baldwin and Lomax, was run 1800 iterations until convergence. The L2 norm peaked at 1.2×10^{-9} and dropped to 3.9×10^{-12} . The average value of y^+ on the upper surface was 4.01 with a maximum of 9.39 at the trailing edge. Figure 3 shows the pressure coefficient distribution at 81.19% root chord for the laminar and turbulent solu-

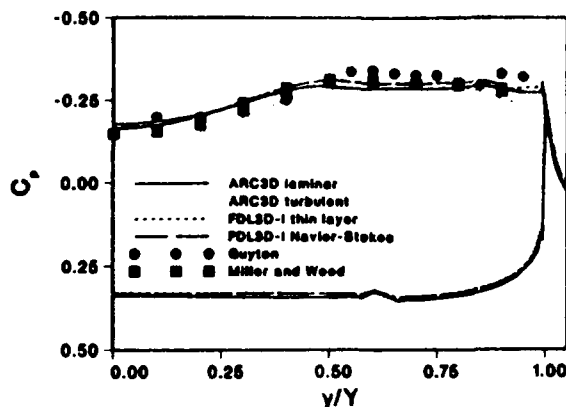


Fig. 3 Coefficient of pressure vs y/Y at 81.18% foot chord for a delta wing: $\Gamma = 75$ deg; $M_\infty = 1.95$; $\alpha = 20$ deg; $Re = 4.48 \times 10^6$.

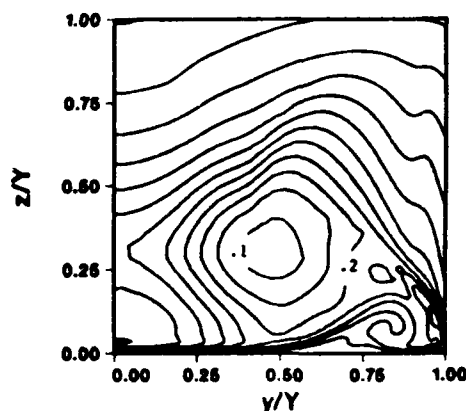


Fig. 4 Contours of normalized pitot pressure at 81.18% root chord for a delta wing using ARC3D with no turbulence model. $\Gamma = 75$ deg; $M_\infty = 1.95$; $\alpha = 20$ deg; $Re = 4.48 \times 10^6$.

tions (as well as data, which will be discussed later). The Reynolds number based on running length at this streamwise location was 3.63×10^6 . Also shown are the data of Guyton⁵ and that of Miller and Wood.³ At this streamwise location, the average value of y^+ was 5.04, the minimum value was 1.76, and the maximum was 8.70. The laminar solution fell between the experimental results from the symmetry plane to the secondary separation point; the turbulent solution predicted pressure coefficients that were lower than the data. The largest difference between the two numerical simulations was 32.8% at the centerline. From the secondary separation point to the leading edge, both solutions predicted lower pressure coefficients than the data. Near the leading edge, the turbulent solution was 12.1% higher than the laminar solution, but the difference was less than the scatter in the experimental data. It appeared that the laminar solution compared more favorably with the data.

Contours of the pitot pressure ratio at 81.19% root chord are given in Fig. 4 for the laminar solution and in Fig. 5 for the turbulent solution. The modeled turbulence has no effect on the predicted location of either the primary or secondary vortex. The effect of turbulence was only apparent near the wall below the primary vortex where the boundary layer was thinner in the turbulent case.

The simulated oil flow patterns for the laminar and turbulent solutions are presented in Fig. 6. The primary, secondary, and tertiary separation and reattachment lines are all evident. They are, from the leading edge inward, the primary separa-

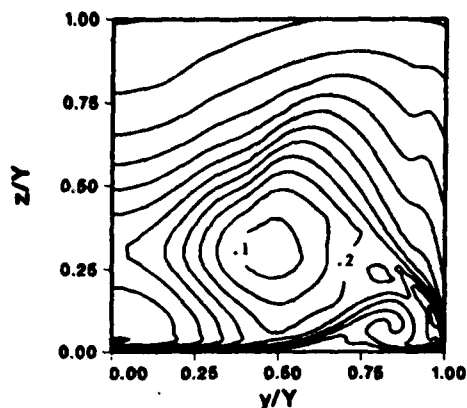


Fig. 5 Contours of normalized pitot pressure at 81.18% root chord for a delta wing using ARC3D with the Baldwin-Lomax turbulence model: $\Gamma = 75$ deg; $M_\infty = 1.95$; $\alpha = 20$ deg; $Re = 4.48 \times 10^6$.

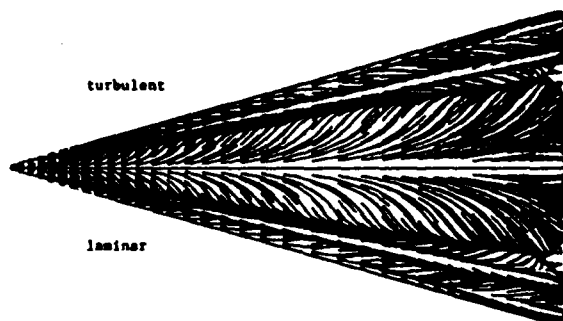


Fig. 6 Simulated oil traces for a delta wing using ARC3D turbulent (upper) and laminar (lower): $\Gamma = 75$ deg; $M_\infty = 1.95$; $\alpha = 20$ deg; $Re = 4.48 \times 10^6$.

tion, secondary reattachment, tertiary separation, tertiary reattachment, secondary separation, and the primary reattachment at the centerline. The difference between the laminar and turbulent shear stress patterns was very minor for the entire surface. This indicated no major structural differences between the two simulations. The small changes in the separation and reattachment lines were apparent in the spanwise variation of the shear stress. Figure 7 depicts one component of the normalized surface shear stress τ_{xz} as a function of the normalized span, at 81.19% root chord. The shear stresses were normalized to their maximum at that streamwise location. The location of the reattachment and separation lines corresponds to the change of sign in τ_{xz} . The secondary separation was slightly farther outboard (60.27 vs 58.82% span) for the turbulent case, whereas the secondary reattachment was inboard (89.83 vs 88.84% span).

Slight differences in pressure coefficient, pitot pressure, and shear stress distribution between the laminar and turbulent solutions were observed. The Baldwin-Lomax turbulence model is well known to be inaccurate in regions of separated flow. For $\alpha = 20$ deg, where no separations were seen, the effects of turbulence were small. At $\alpha = 30$ deg, large regions of separated flow have been previously observed, making use of the Baldwin-Lomax inappropriate. Since we are primarily interested in the assessment of the numerical procedure, accuracy, and flowfield structure, only laminar solutions were used in the remainder of this paper.

The second calculation used FDL3D-I with the thin-layer approximation. The solution required 2400 iterations using

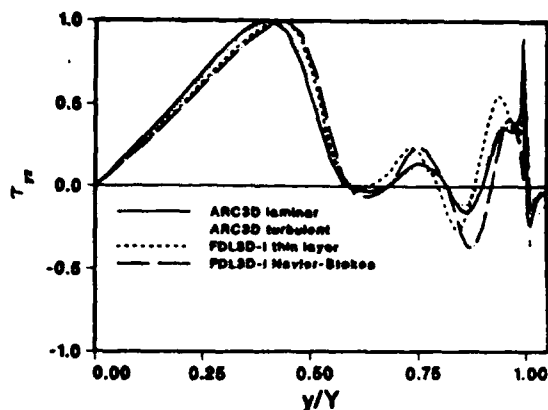


Fig. 7 Shear stress τ_{xz} vs y/Y at 81.19% root chord for a delta wing: $\Gamma = 75$ deg; $M_\infty = 1.95$; $\alpha = 20$ deg; $Re = 4.48 \times 10^6$.

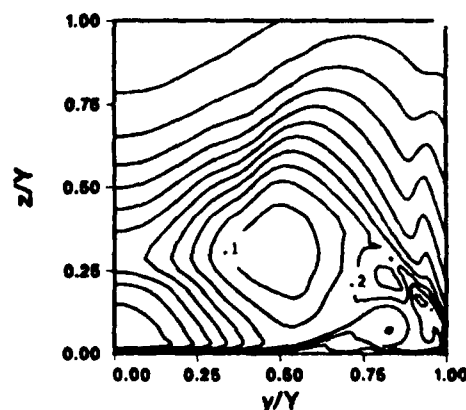


Fig. 8 Contours of normalized pitot pressure at 81.19% root chord for a delta wing using FDL3D-I thin layer: $\Gamma = 75$ deg; $M_\infty = 1.95$; $\alpha = 20$ deg; $Re = 4.48 \times 10^6$.

the same time step and damping coefficients that were used in the ARC3D calculation. The L2 norm peaked at 1.3×10^{-3} and dropped to 7.6×10^{-5} . The pressure coefficient distribution at 81.19% root chord is compared to the ARC3D thin-layer result in Fig. 3. The greatest difference between them was 6.84% (at the centerline) and, in general, both were in excellent agreement with the experimental data.

Figure 8 shows contours of the pitot pressure ratio from FDL3D-I thin layer at 81.19% root chord. When compared to the ARC3D result in Fig. 4, it was seen that both codes capture the primary and secondary vortices. The predicted location of the primary vortex was almost exactly the same for the two codes. However, the secondary was farther outboard for ARC3D (81.97 vs 84.70% span). FDL3D-I was in better agreement with the experimental results from Monnerie and Werle¹ which placed the secondary at 82.5% span.

The simulated oil flow patterns compared very well over the surface and are not presented here. Both display the primary, secondary, and tertiary separation and reattachment lines. In addition, both capture a very small region of reversed flow at the trailing edge, which was observed in the previous work. The differences between the two thin-layer solutions were more apparent in the spanwise variation of the shear stress, as seen in Fig. 7. The location of the secondary separation was nearly the same for both solutions; however, the secondary reattachment, the tertiary separation, and reattachment for FDL3D-I were inboard of their locations, as predicted by ARC3D (88.02 vs 89.84% span, 79.62 vs 81.81% span, and

63.38 vs 67.69% span, respectively). The preceding results indicate that FDL3D-I (using the thin-layer equations) and ARC3D produce very similar solutions.

The third calculation used the full Navier-Stokes equations and evolved 3000 iterations with the same time step and damping terms that were used in the FDL3D-I thin-layer calculation. The L2 norm peaked at 1.15×10^{-3} and dropped to 9.7×10^{-5} . The pressure coefficient distribution at 81.19% root chord from the full and thin layer Navier-Stokes equations are compared in Fig. 3. The two results were nearly identical for the first 80% of the span and display a 8.86% difference in the pressure coefficient near the outboard edge. There was excellent agreement with the data of Miller and Wood.³

Figure 9 shows contours of the pitot pressure ratio at 81.19% root chord for the FDL3D-I Navier-Stokes simulation. Comparison to the thin-layer result in Fig. 8 shows that the location of the primary vortex was nearly identical. However, the secondary vortex was farther outboard for the Navier-Stokes result (81.97 vs 85.25% span).

The simulated oil flows along the upper surface again showed only slight differences between the two solutions and are not presented here. The shear stress from the thin-layer and Navier-Stokes solutions are compared in Fig. 7. The secondary separation point for both results were nearly the same, 59.22% and 58.92% span for the thin-layer and Navier-Stokes solutions, respectively. The secondary reattachment

and tertiary separation and reattachment all were further inboard for the thin-layer result (92.04 vs 88.02% span, 81.72 vs 79.62% span, and 67.87 vs 63.38% span, respectively).

From these above figures, it was concluded that differences between the thin-layer and the Navier-Stokes results were quite small for a delta wing at $\alpha = 20$ deg and the thin-layer calculation (which was less expensive) captures the essential flow features.

An interpolation using the full Navier-Stokes solution was then performed to provide an initial condition for the grid resolution study. The fine grid had approximately twice as many points as the primary grid. In addition to the doubling of the computational domain, the local time step was reduced by the local scaling with the Jacobian. These two factors combined to make this an extremely expensive calculation; thus, only 600 iterations were run. This was sufficient for the L2 norm to return to its starting value. The L2 norm peaked at 7.03×10^{-4} and dropped to 5.8×10^{-5} . Figure 10 presents the pressure coefficient distribution at 81.19% root chord. There were very slight differences between the two solutions, particularly in the region between the primary and secondary vortex. Contours of the pitot pressure ratio for the fine grid solution are presented in Fig. 11. For the region of the primary, secondary, and tertiary vortices, the fine grid solution reveals additional minute structures. These structures were also indicated in the lateral shear stress in Fig. 12. In the fine grid solution, the sep-

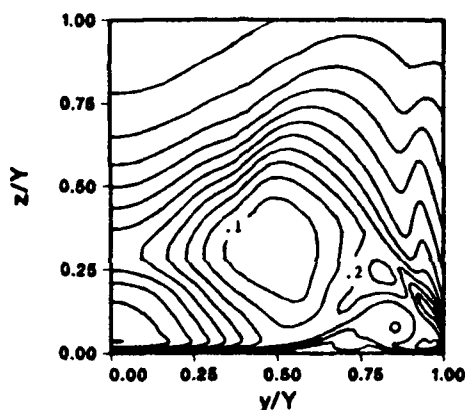


Fig. 9 Contours of normalized pitot pressure at 81.19% root chord for a delta wing using FDL3D-I Navier-Stokes: $\Gamma = 75$ deg, $M_\infty = 1.95$, $\alpha = 20$ deg, $Re = 4.48 \times 10^6$.

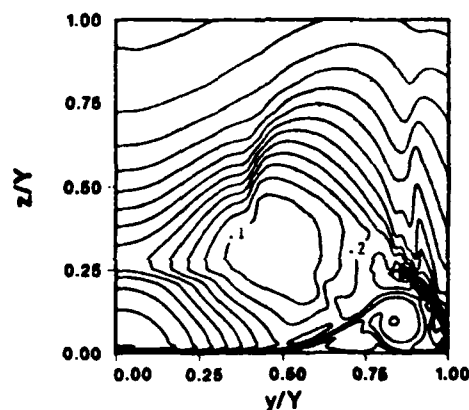


Fig. 11 Contours of normalized pitot pressure at 81.19% root chord for a delta wing using FDL3D-I with grid refinement: $\Gamma = 75$ deg, $M_\infty = 1.95$, $\alpha = 20$ deg, $Re = 4.48 \times 10^6$.

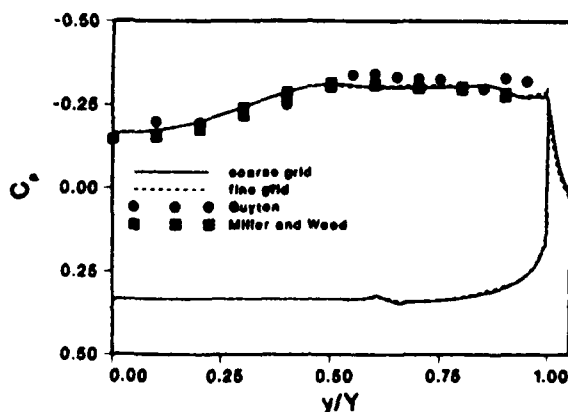


Fig. 10 Coefficient of pressure vs y/Y at 81.19% root chord for a delta wing using FDL3D-I with grid refinement: $\Gamma = 75$ deg, $M_\infty = 1.95$, $\alpha = 20$ deg, $Re = 4.48 \times 10^6$.

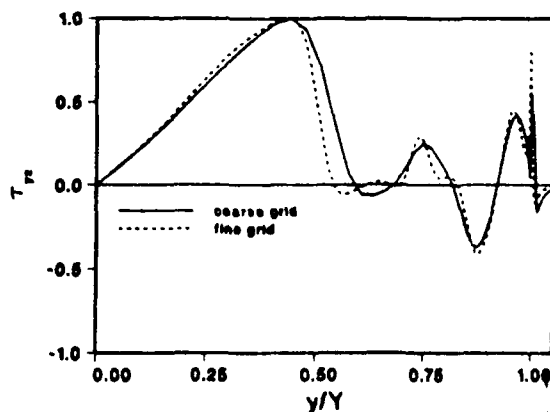


Fig. 12 Shear stress τ_{xy} vs y/Y at 81.19% root chord for a delta wing using FDL3D-I with grid refinement: $\Gamma = 75$ deg, $M_\infty = 1.95$, $\alpha = 20$ deg, $Re = 4.48 \times 10^6$.

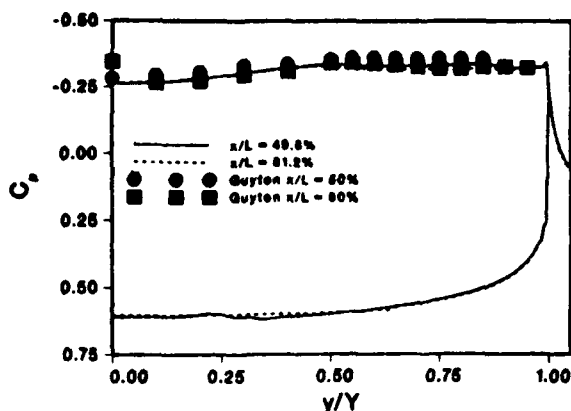


Fig. 13 Coefficient of pressure vs y/Y at 49.80 and 81.19% root chord for a delta wing using FDL3D-I: $\Gamma = 75^\circ$, $M_\infty = 1.95$; $\alpha = 35^\circ$; $Re = 4.48 \times 10^6$.

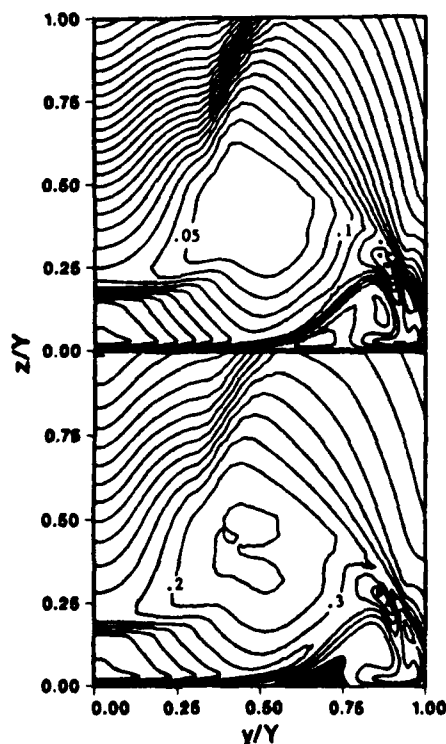


Fig. 14 Contours of a) normalized pitot pressure and b) ρU at 90.0% root chord for a delta wing, full Navier-Stokes simulation: $\Gamma = 75^\circ$, $M_\infty = 1.95$; $\alpha = 35^\circ$; $Re = 4.48 \times 10^6$.

aration between the secondary and tertiary separation points have spread laterally to accommodate the additional vortical structures.

The Navier-Stokes equations were used to calculate the flow over a delta wing at $\alpha = 30^\circ$, which required 2000 iterations. The L2 norm peaked at 1.2×10^{-3} and dropped to 8.6×10^{-5} . The pressure coefficient distribution at 49.80% and 81.19% root chord is presented in Fig. 13. Included are experimental data from Guyton² at 50 and 80% of the root chord. From the centerline to 45% span, the pressures were equal, but outboard they diverge with the downstream pressures being up to 5.0% higher. The agreement with the experimental data was

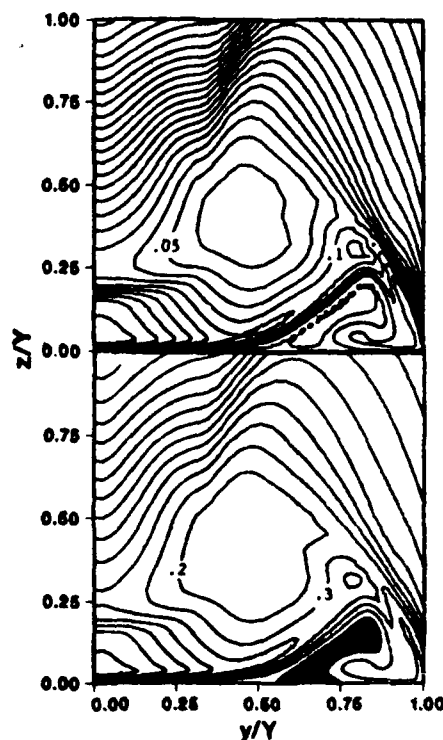


Fig. 15 Contours of a) normalized pitot pressure and b) ρU at 90.0% root chord for a delta wing, thin layer simulation from Ref. 13: $\Gamma = 75^\circ$; $M_\infty = 1.95$; $\alpha = 35^\circ$; $Re = 4.48 \times 10^6$.

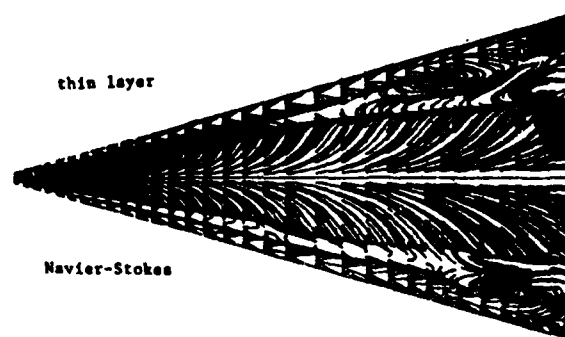


Fig. 16 Simulated oil traces for a delta wing using thin layer (upper) and Navier-Stokes (lower): $\Gamma = 75^\circ$; $M_\infty = 1.95$; $\alpha = 35^\circ$; $Re = 4.48 \times 10^6$.

very good. Figures 14 show contours of normalized pitot pressure (Fig. 14a) and the product of the density and the streamwise Mach number (Fig. 14b) at 89.74% root chord. This product was negative in the darkened region, indicating reversed flow. The reversed flow was contained in a region along the surface beneath the secondary vortex. Results from the previous work are presented in Figs. 15. The location of the primary vortex is the same for the two simulations. However, the height of the reversed flow region (normalized by the span) was much smaller (0.0884 compared to 0.195). This difference is due to the additional diffusion calculated in the Navier-Stokes solution.

Figure 16 depicts the surface shear map for the present Navier-Stokes solution and the previous thin-layer solution. The reversed flow region extends forward to 46% root chord

compared to 67% for the thin-layer solution. Also visible are two large counter-rotating vortical structures. In the nomenclature of Tobak and Peake¹⁶ these are referred to as nodes. These vortices are formed by the viscous interaction between the reversed flow and the streamwise flow. The inboard vortex was swept up and inward by the primary vortex. The outboard vortex was swept up and inward by the secondary vortex. These two structures merge above the reversed flow region and are swept downstream. In the Navier-Stokes solution, the inboard and outboard nodes are located at 84.13 and 85.1% of the root chord, respectively. In the thin-layer solution, they are located at 94.23 and 76.92% of the root chord, respectively. In addition to the large nodes, a smaller node was located in each of the solutions. These nodes are too small to be discerned in Fig. 16. For the Navier-Stokes solution, the third node is located at 53.1% root chord along the secondary separation line. In the thin-layer solution, the third node is located at the trailing edge along the tertiary separation line.

These are significant differences between the thin-layer and Navier-Stokes simulations for a delta wing at $\alpha = 30$ deg. These differences manifested themselves in the secondary vortex where a shear layer is present. The variation in the streamwise and normal (to the upper surface) extent of the reversed flow region is most evident.

Conclusions

The supersonic flowfield about a delta wing ($\Gamma = 75$ deg) was numerically simulated at $M_\infty = 1.95$ and 4.48×10^6 . Two different codes based on the approximately factorized implicit Beam-Warming algorithm were used in the study. To assess the effects of turbulence, ARC3D was used with and without the Baldwin-Lomax turbulence model. The laminar and turbulent solution exhibited very little difference in the predicted vortical structure. This indicates that turbulence was not overly critical for a delta wing at $\alpha = 20$ deg with the present grid resolution.

The comparison between ARC3D and FDL3D-I (thin layer) showed minor differences in the predicted pressure coefficient distribution, location of the primary and secondary vortices, and surface shear stress. A comparison was made between the thin-layer and Navier-Stokes solutions generated by FDL3D-I. The two solutions were nearly identical, indicating that there was no advantage in using the Navier-Stokes equations over the thin layer equations of delta wing simulations at moderate angles of attack.

A calculation carried out on a refined grid for $\alpha = 20$ deg reveals that the numerical result is essentially independent from grid refinement. A calculation with FDL3D-I using the full Navier-Stokes equations was then made. For the $\alpha = 20$ deg calculation, there was no improvement with grid resolution.

Navier-Stokes solution for a delta wing at $\alpha = 30$ deg showed an embedded reverse flow region that was observed in an earlier thin-layer calculation. The dimensions of this sepa-

rated flow region was significantly different from the thin-layer calculation. The reversed flow region exhibited strong velocity gradients in directions other than normal to the body surface. The thin-layer approximation does not account for the viscous term associated with these gradients.

Acknowledgments

Computer time for the work presented here was provided under the auspices of the Air Force Weapons Laboratory at Kirtland Air Force Base. The authors wish to thank N. Rapagnani for his assistance in procuring these resources.

References

- ¹Monnerie, H., and Werle, H., "Study of Supersonic and Hypersonic Flow About a Slender Wing at an Angle of Attack," *Hypersonic Boundary Layers and Flow Fields*, AGARD CP-30, May 1968, pp. 23-1-23-19 (in French).
- ²Hummel, D., "On the Vortex Formation over a Slender Wing at Large Angles of Incidence," *High Angle of Attack Aerodynamics*, AGARD CP-247, 1987, pp. 13-1-13-17.
- ³Miller, D. S., and Wood, R. M., "Lee-Side Flow over Delta Wings at Supersonic Speeds," NASA TP-2430, June 1985.
- ⁴Stallings, R. L., and Lamb, M., "Wing-Alone Aerodynamic Characteristics for High Angles of Attack at Supersonic Speeds," NASA TP-1889, 1981.
- ⁵Guyton, R. W., private communication, 1989.
- ⁶Rizzetta, D. P., and Shang, J. S., "Numerical Simulation of Leading-Edge Vortex Flows," *AIAA Journal*, Vol. 24, No. 2, 1986, pp. 237-245.
- ⁷Buter, T. A., and Rizzetta, D. P., "Steady Supersonic Navier-Stokes Solutions of a 75° Delta Wing," NASA CP-2416, Oct., 1985.
- ⁸Thomas, J. L., and Newsome, R. W., "Navier-Stokes Computations of Leeward Flows Over Delta Wings," AIAA Paper 86-1949, May 1986.
- ⁹Scherr, S., and Das, A., "Basic Analysis of the Flow Fields of Slender Delta Wings Using the Euler Equations," International Council of the Aeronautical Sciences, Paper ICAS-88-5.2, Aug. 1988.
- ¹⁰Fujii, K., and Schiff, L. B., "Numerical Simulation of Vortical Flows Over a Strake-Delta Wing," AIAA Paper 87-1229, June 1987.
- ¹¹Kandil, O. A., and Chung, H. A., "Unsteady Vortex Computations Past Oscillating Delta Wing at High Incidence," AIAA Paper 89-0081, June 1987.
- ¹²Kandil, O. A., and Chung, H. A., "Unsteady Vortex-Dominated Flows Around Maneuvering Wings Over a Wide Range of Mach Numbers," AIAA Paper 88-0317, Jan. 1988.
- ¹³Webster, W. P., and Shang, J. S., "Numerical Simulation of Reversed Flow Over a Supersonic Delta Wing at High Angles of Attack," AIAA Paper 89-1802, June 1989.
- ¹⁴Pulliam T. H., "Efficient Solution Methods of the Navier-Stokes Equations," *Lecture Notes for the Von Karman Institute for Fluid Dynamics Lecture Series: Numerical Techniques for Viscous Flow Computation in Turbomachinery Bladings*, Jan. 1986.
- ¹⁵Visbal M. R., "Numerical Investigation of Laminar Junction Flows," AIAA Paper 89-1873, June 1989.
- ¹⁶Tobak, M., and Peake, D. J., "Topology of Three-Dimensional Separated Flows," *Annual Review of Fluid Mechanics*, Vol. 14, 1982, pp. 61-85.